A Study of Micromachined Displacement Pumps for Vacuum Generation

by

Hui Zhou

B.E., Materials Science and Engineering
Tsinghua University, 2002
M.E., Materials Science and Engineering
Tsinghua University, 2004
S.M., Materials Science and Engineering
Massachusetts Institute of Technology, 2008

Submitted to the Department of Electrical Engineering and Computer Science
in partial fulfillment of the requirements for the degree of

Doctor of Philosophy in Electrical Engineering and Computer Science
at the

MASSACHUSETTS INSTITUTE OF TECHNOLOGY
September 2011

Author _____
Hui Zhou
Department of Electrical Engineering and Computer Science
July 22, 2011

Certified by _____
Martin A. Schmidt
Professor of Electrical Engineering and Computer Science
Thesis Supervisor

Accepted by _____
Leslie A. Kolodziejski
Professor of Electrical Engineering and Computer Science
Chairman, Department Committee on Graduate Students

A Study of Micromachined Displacement Pumps for Vacuum Generation

by

Hui Zhou

Submitted to the Department of Electrical Engineering and Computer Science
on July 22, 2011 in partial fulfillment of the requirements for the degree of
Doctor of Philosophy in Electrical Engineering and Computer Science

Abstract

Micromachined vacuum pumps are one of the key components in miniature systems for chemical and biological analysis. Miniature sensors and analyzers are normally operated at the pressure range lower than a few millitorr.

We are developing a micromachined vacuum pump that is comprised of a mechanical rough pump integrated with micromachined ion-pumps. The rough pump generates a low vacuum of tens of torr from atmospheric pressure for the ion-pumps to initialize. Field ionization and electron impact ionization pumps that connect to the rough pumps continue to pump from the low vacuum of tens of torr to high vacuum of millitorr or even microtorr. The focus of this thesis work is on the development of the micromachined rough pump.

A micromachined displacement pump concept is adopted for the development of the chip scale vacuum rough pump. The micro displacement pump is designed with the aid of analytical and numerical modeling. The rough pump is fabricated by deep-reactive ion etching and other standard micromachining techniques. Systematic study into operation of this class of pumps allows us to now report on a pump that achieves 164 torr absolute pressure, which is to our knowledge the lowest measured pressure in a micromachined vacuum pump operated from atmospheric pressure. This performance improvement is significant in that it enables a base pressure of less than 35 torr for a two-stage design, which allows integration with the ion pump, thus leading to realization of miniature chemical and biological analyzers. More importantly, the understanding of the micromachined displacement pumps for vacuum generation has been greatly improved and a universal model has been developed, which is very powerful to describe and predict the micromachined displacement pump behavior for vacuum generation.

Thesis Advisor: Martin A. Schmidt
Title: Professor of Electrical Engineering and Computer Science

Acknowledgements

One of the greetings I received after I passed my doctoral thesis defense was “it has been a long journey but a well worth one”. It is very true.

It has been seven years since the first time I landed on this land and joined the institute, and the research work presented in this thesis is my third project ever since then. The journey started with excitement for a new environment and joy with new friends, and is ending with a sense of accomplishment and enthusiasm for the future life. It has not been a straight journey though. These past seven years have been filled with challenges and struggles, but I was fortunate to meet my advisor, Martin A. Schmidt, who have guided me into the world of MEMS and helped me through the tough times. As my research advisor, Marty is very knowledgeable and responsible; as my life saver, he is extraordinary considerate and supportive. His professionality and personality are the example I would follow in my life.

Next I would like to thank Hanqing Li, my other research supervisor. Hanqing is experienced in almost every piece of equipments in Microsystems Technology Laboratories (MTL) for MEMS fabrication. Without his supervision and direct help on the fabrication, this thesis work would take much longer to finish.

I am also very grateful for the help from my other two committee members, Carol Livermore and Akintunde I. (Tayo) Akinwande. Carol is the PI of the Chip Scale Vacuum Micro Pump (CSVMP) project. She has been organizing the project meetings weekly or biweekly, and providing many great advice and feedback on my work. I have been working with Tayo through two projects, and his critical questions always make me think and I have learned many lessons from him.

The other team members on the CSVMP project are also very helpful. I want to thank the whole team for all the great discussions, in particular Luis Velásquez-García, who is enthusiastic on my project and is another good resource of microfabrication techniques.

The fabrication was conducted in MTL at MIT, and I want to thank Vicky Diadiuk and all other MTL staff. I want to acknowledge the MTL community leader Debb Hodges-Pabon; all my trainers Donal Jamieson, David Terry, Bernard Alamariu, Robert Bicchieri, Kurt Broderick, Dennis Ward, Eric Lim, Krisofor Payer, Paul Tierney, Daniel A. Adams, Paudely Zamora; EHS coordinator Patricia Burkhart; and facility coordinator Paul McGrath.

Also I want to thank our past and present group members Vikas Sharma, Kerry Cheung, Valérie Leblanc, Eric Lam and group administrator Anthee Travers, Anne Wasserman, and Juanita Rivera, along with all my friends who have brought light into my life, in particular Charles Hsu and Jifeng Liu.

I would like to thank my family for their unlimited love, especially my parents, my grandparents, my sister and brother-in-law.

Finally, I would like to thank my wife Haiying Li for her infinite love, support and encouragement. Her happiness is the very motivation for me to work hard.

Table of Contents

Symbols

α: damping constant
η: fluidic viscosity
ρ: density
τ: fluidic time constant
ω_0: undamped resonant frequency
ω_d: damped resonant frequency
b: damping coefficient
c: initial squeeze-film thickness
C: fluidic capacitance
k: spring constant
m: mass
P_0: atmospheric pressure (~760 torr)
$P_1 \sim P_6$: test volume pressure after Step 1~6
P_a: pneumatic actuation pressure differential (in torr)
P_i: test volume pressure before Step 1
P_t: test volume pressure
P_{vacuum}, P_v: ultimate base pressure (vacuum pressure)
ΔP: pressure differential
$(dP/dt)_{Pt}$: pressure derivative
Q: flow rate
Q_{leak}: leak rate
r: radius
R: fluidic resistance
$t_1 \sim t_6$: duration of Step 1~6
T: operational cycle time
T_c: gas charging time
T_{disc}: gas discharging time
$v_{pumping}$: pumping speed
V: volume
V_{dead}, V_d: dead volume
V_{d0}: dead volume by design
$V_{pumping}$, V_p: pumping volume
V_t: test volume
w: deflection

List of Figures

List of Tables

Chapter 1

Introduction and Background

1.1 Project Introduction

Micromachined vacuum pumps are one of the key components in miniature systems for chemical and biological analysis. For example, in mass spectrometers, it is important that the ions produced in the ionization chamber have a free run through the machine without any collision with air molecules, therefore a high vacuum is required. In general, the applications of the miniature vacuum pumps are almost unlimited – wherever a vacuum is needed at micro scale, they are suitable. Micro vacuum pumps have many other applications than creating the vacuum environment for sensors and analyzers. They may also provide pneumatic actuation of liquids for lab-on-a-chip devices, and due to their high compression capability, vacuum pumps can be easily converted to high pressure pumps for gas chromatography.

However, vacuum pumps are difficult to scale down. The pumping volume would be reduced proportionally to the pump size and thus the leakage would have a much larger effect on the ultimate base pressure for micro vacuum pumps. Though micromachined pumps have been well studied [1], only a few have been developed for vacuum generation. Examples of vacuum pumps that operate at atmospheric pressure include Knudsen pumps [2], vapor-jet pumps [3][4], sputter-ion pumps [5], and displacement pumps [6][7]. The lowest absolute pressure these pumps have achieved is about 350 torr [2].

Miniature sensors and analyzers, e.g. a miniature mass analyzer, are typically operated at the pressure range of millitorr [8]. We are developing a micromachined vacuum pump that is comprised of a mechanical rough pump integrated with micromachined ion pumps. A rough pump generates a low vacuum of tens of torr from atmospheric pressure. A field ionization pump and an electron impact ionization pump that connect to the rough pump continue to pump from the low vacuum of tens of torr to a high vacuum. A field ionization pump reduces the pressure from tens of torr to 10^{-3}~10^{-4} torr, and an electron impact ionization pump continues to pump down from 10^{-3} torr to lower than 10^{-6} torr. The schematic of the chip scale vacuum micro pump is shown in Figure 1-1. Additional components, the separation valve between the rough pump and high vacuum pump and an in-situ pressure sensor, are also shown in the figure.

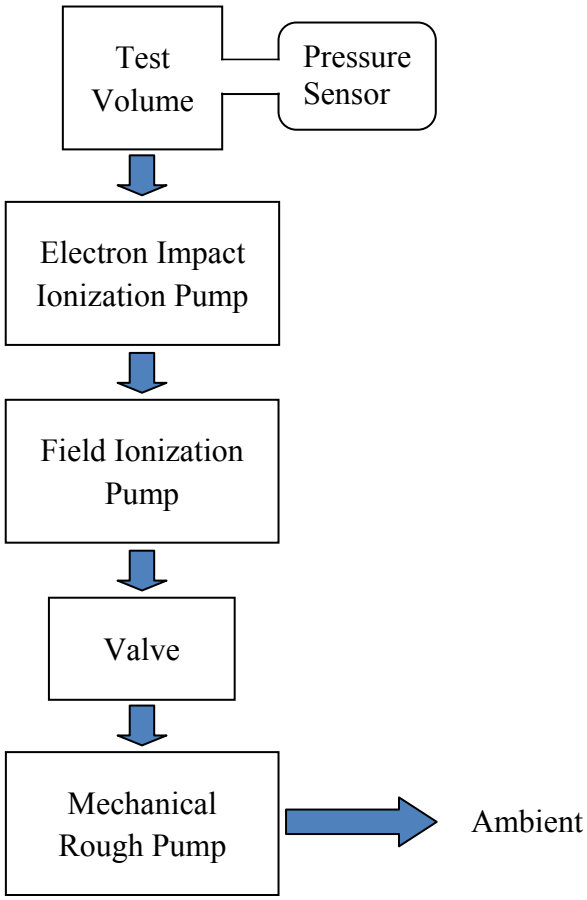

Figure 1-1: Schematic of the chip scale vacuum micro pump.

The focus of this thesis work is on the development of the micromachined rough pump. We have chosen a micromachined displacement pump design because it has a relatively simple structure and is capable of achieving a vacuum level of tens of torr to initialize the ion pumps. The power consumption of the displacement pumps may also be lower than 1W. The goal of the thesis is to study the limit of this type of pumps for vacuum generation. Displacement pumps will be designed, modeled, fabricated, and characterized.

For portability purposes, the chip scale rough vacuum micro pumps need to be small in size and low in power consumption to achieve a low pressure, as required by the sponsor (Defense Advanced Research Projects Agency). The major specifications of the micromachined rough vacuum pumps are listed as below:

(1) Target base pressure for two-stage rough pumps: ~30 torr

The ion pumps are expected to start working from tens of torr, e.g. ~30 torr. The pressure drop of the rough pumps is (760 torr / 30 torr) = 25X, which is difficult to achieve with a single-stage micromachined pump in practice from atmospheric pressure [1~7]. A two-stage pump design is more practical, which we propose in this thesis work. If the two stages are identical in geometry and thus in pumping capability, each stage must be able to achieve a pressure drop of ~5X, i.e. the ultimate base pressure of the first stage of the pump – the one connecting to the ambient – is then ~152 torr.

With this pressure for the first stage, the maximum pressure differential during the pump operation is then over 500 torr. The actuation force against the pressure differential is as large as 1.8N for the pump chamber design as described in Chapter 2. A relatively large actuation force is then required for pump operation and characterization. Furthermore, the large pressure drop of ~5X needs a high compression ratio of the pump chamber (the pumping volume divided by the dead volume). The details are discussed in Chapter 2. With the large force generated from the micro actuators, the magnitude of the actuation stroke needs to be on the order of tens of microns.

(2) Total volume limit for two-stage pumps (without energy source): 1cm^3

The micromachined vacuum pumps are for portable applications, and the size of the whole vacuum pump without the energy source, batteries or fuel cells, is limited to 2cm^3. Half of the vacuum pump is for our two-stage rough pump, which is 1cm^3. This gives the volume budget of the rough pump integrated with the appropriate actuators.

(3) Power consumption: < 1W

One of the major applications of the micromachined vacuum pumps is for field use, and sustainability is very important. The power consumed by the pumps is expected to be lower than 1 watt. Any actuator that dissipates too much energy is not suitable for the pumps. This thesis focuses on the study of the vacuum generation performance of micro displacement pumps, and the integration of actuators is not covered in great detail. The selection of the micro actuators is discussed in Section 1.4 based on the power consumption, and the micro pumps are designed in Chapter 2 accordingly.

(4) Microfabrication capability

The MEMS devices are either assembled at die level or at wafer level. Die level assembly is flexible in practice and the actuators can be integrated manually. On the other hand,

wafer level assembly allows for more precise alignment and is capable of batch fabrication. Also in the long run, the rough pump is going to be bonded with the other parts of the vacuum pump, and microfabricated actuators will facilitate the final product development.

According to all the requirements of the two-stage rough pumps, the micro actuators are discussed next and the design of the pumps is discussed in Chapter 2.

1.2 Micro Vacuum Pumps Overview

Micro vacuum pumps that operate at atmospheric pressure can use mechanics of thermal expansion, vapor diffusion, chemisorption, or mechanical compression. Examples of the first three types of micro vacuum pumps are reviewed in this section, and the last one is discussed in more detail in Section 1.3.

(1) Knudsen pumps

A Knudsen pump is one of the thermal molecular pumps, which uses the principle of thermal transpiration. An example of the Knudsen pumps is from reference [2]. Gas flows from the hotter chamber to the colder chamber, and cascading multiple stages are possible. The lowest reported base pressure of a single-stage Knudsen pump is 350 torr. One point that needs to be noted is the maximum flow rate is only 1×10^{-6} cc/min for the pump. Thus, because of the steady-state thermal dissipation and relatively low flow rate, we will not consider the thermal molecular pumps.

(2) Vapor-jet pumps

Based on a diffusion mechanism, the vapor-jet pumps may be used for vacuum generation. An example is from reference [3][4]. A working fluid is evaporated by a heater. A high velocity vapor jet is obtained through the nozzles. Gas molecules mix with the vapor jet, and then the vapor condenses on the cooled side walls. The fluid returns to the heater unit afterward to complete the working loop. The ultimate pressure the vapor-jet obtained is ~370 torr [3]. The power consumption was not reported, but the heat dissipation would be an obstacle to meet the power budget of this project, and a micro diffusion pump is not considered for this thesis.

(3) Sputter-ion pumps

Micro sputter-ion pumps can be used for vacuum generation from atmospheric pressure. Localized stable micro-plasma discharges can be created between thin-film titanium

electrodes to sputter the cathode and the gas molecules are chemisorbed through reactive sputtering [5]. The base pressure achieved is 592 torr, with operational voltages of 1000~1500 V. The chemisorption pump requires a large area of the getter and the operational voltage is high.

These three types of micromachined pumps have their own limitations. Another type of micro pump is very promising for vacuum generation from atmospheric pressure, the displacement pump, which is discussed in the following section.

1.3 Micro Displacement Pumps Overview

1.3.1 Three Categories of Displacement Pumps

The micro displacement pumps are commonly used in hydraulic pumps, and can also be used for vacuum generation. Displacement pumps fall into three categories by operation styles: reciprocating pumps, rotary pumps, and aperiodic pumps [1].

(1) Reciprocating pumps

The majority of displacement pumps reported are reciprocating pumps. The pumping occurs by alternating gas charging and discharging through the actuation of the pump chamber. The pump chamber is opened and gas fills into the chamber during the gas charging step. The gas inside the pump chamber is compressed out of the pump chamber during the gas discharging step. The schematic view of a displacement vacuum pump is shown in Figure 1-2 with (a) the gas charging step, and (b) the gas discharging step. Actuators are needed for the pump actuation, such as piezoelectric disks [6][10], cylinders [11] or stacks [12], electrostatic actuators [7], electromagnetic actuators [13], thermopneumatic actuators [14], or thermal actuators [15].

Sometimes the pump chamber is not obvious but the operation follows the same peristaltic concept, such as in the pneumatically driven pump from reference [18].

Three reported micro displacement vacuum pumps are listed in Table 1-1. The valve types are discussed in Section 1.3.2, the active valve, the passive valve, and valve-less. The lowest absolute pressure was measured to be 498 torr. Though the pressures reported by the displacement pumps were not as low as that obtained by the Knudsen pump and the vapor-jet pump reviewed before, micromachined displacement pumps have a relatively simple structure and may offer very favorable power performance. Also this type of micro pump is promising to achieve reasonable vacuum levels of a couple

hundred torr, with a high compression ratio (the pumping volume divided by the dead volume).

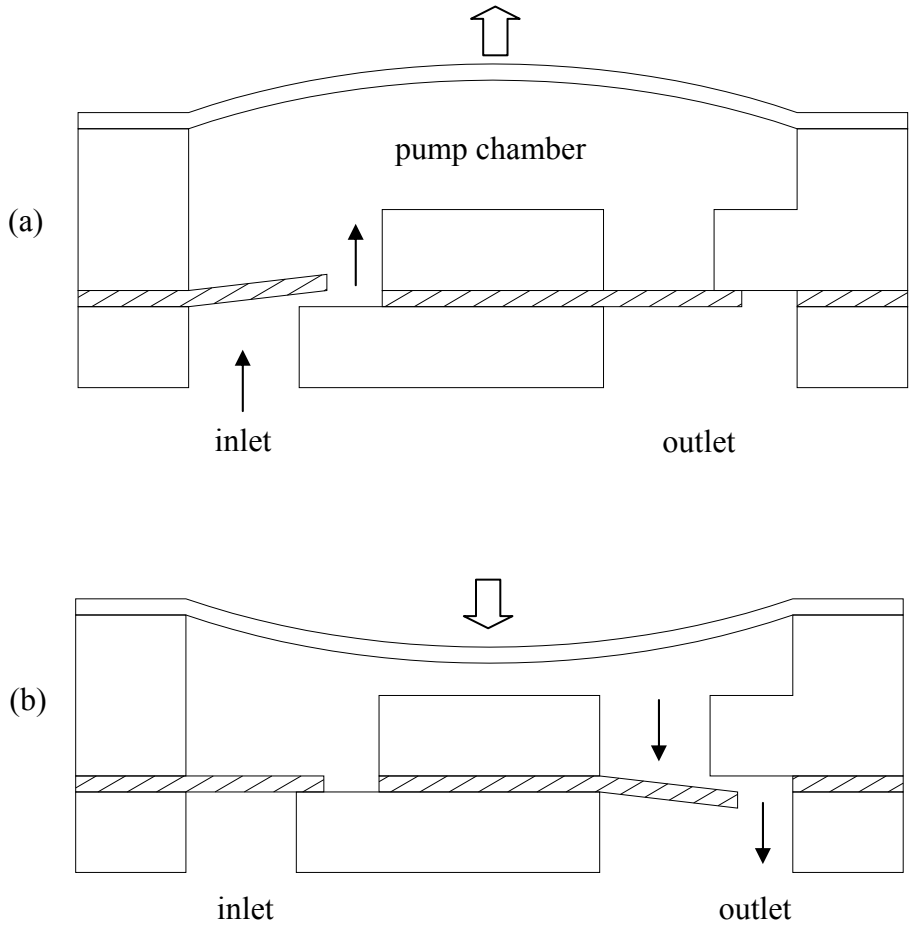

Figure 1-2: Schematic views of a reciprocating displacement pump (adapted from [10]). (a) Gas charging step; (b) gas discharging step.

Table 1-1: Examples of micro displacement vacuum pump.

Author, Year	**Actuation**	**Valves**	**P (torr)**
Kamper, 1998 [6]	Piezoelectric disc	Passive (flap)	498
Rapp, 1994 [25]	Pneumatic	Passive (flap)	725
Sharma, 2009 [26]	Pneumatic	Active	502

(2) Rotary pumps

Rotary pumps are typically driven by gears at a relatively high rotational frequency. The rotary pumps are best suited to use with high viscosity fluids, however, they were also used for vacuum generation achieving a pressure of 741.6 torr [17].

(3) Aperiodic pumps

Most of the micromachined pumps are operated periodically, but in some applications the pumping volume of the fluid is not constant with time and the pumps are then aperiodic. The operations of aperiodic pumps are flexible, and examples include the electrowetting pumps [19] and phase-change pumps [20].

Among all three types of the micro displacement pumps, the reciprocating pumps are the best suited for vacuum generation due to their capability of achieving high compression ratio. The operation of this kind of pumps is then discussed in the following section.

1.3.2 Operation of Micro Reciprocating Pumps

The operation of the reciprocating pumps includes two major steps, gas charging and gas discharging. The two major steps vary based on the exact valve type the pumps incorporate. The three valve types are passive valves, active valves, or valve-less.

(1) Pumps with passive valves

The pump shown in Figure 1-2 uses passive valves, which deflect due to the pressure differential. Therefore, the operation of the pumps with passive valves only includes the two major steps to actuate the chamber open and closed. Gas self-fills the pump chamber when the chamber expands, and is pumped out when the chamber contracts. The passive check valves include cantilevers (flap valves), float (bridge) valves [21], and ball valves [22].

(2) Valve-less pumps

Valve-less pumps are often referred to as no-moving-parts pumps or diffuser/nozzle pumps as shown in Figure 1-3. The operation of valve-less pumps is similar with that of the pumps with passive valves. Two steps are conducted alternatively: (a) gas charging step and (b) gas discharging step. The solid arrows indicate the flow direction, the bigger the arrow, the larger the flow rate.

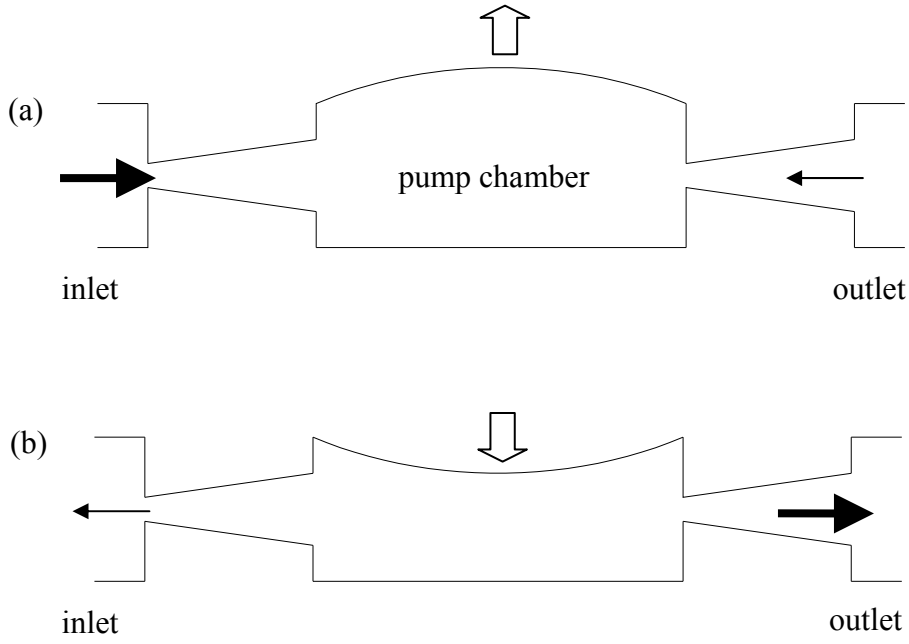

Figure 1-3: Single chamber valve-less micropump (adapted from [23]).
(a) Gas charging step; (b) gas discharging step.

(3) Pumps with active valves

The leaking resistance is proportional to the viscosity of the medium, either hydraulic fluid or gases, as discussed in Chapter 2. Thus, in vacuum pumps, the leakage is much larger than that in hydraulic pumps due to the much lower viscosity of the gases. Diffuser/nozzle pumps are the simplest in terms of structure complexity and are capable of extreme miniaturization. However, without the valves, the leaking from the diffuser/nozzle prevents the pump from reaching a low base pressure. Passive valves help in the valve sealing compared with valve-less structures, but the sealing force is dependent on the pressure differential inside the pump itself as in Figure 1-2. Active valves use independent actuators which provide positive sealing forces, which may be much larger than the sealing forces for the passive valves. Thus the active valves are preferred.

Active valves have actuators attached, and then the operation of the pumps with active valves would have a few more steps for valve operations. The vacuum generation of a single-stage pump with active valves typically uses a 6-step operation cycle, as shown schematically in Figure 1-4. The active valves can be simple rings [24]. For better sealing, the valve can also use complicated structure, e.g. the one in [12].

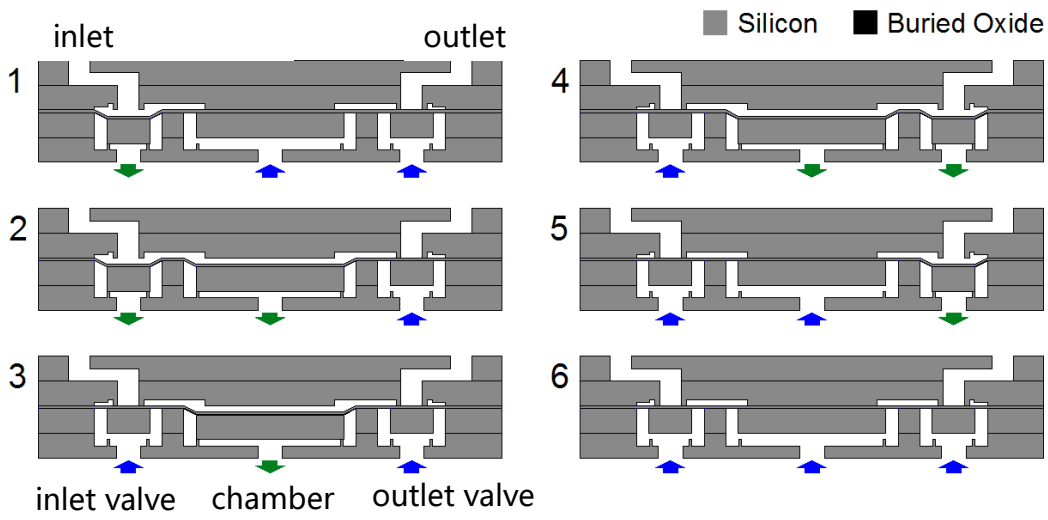

Figure 1-4: The 6-step operation cycle. Blue arrows indicate pushing-up actuations by applying high pressure, and green arrows label pulling-down actuations by using an external vacuum pump. The top left port connects to the test volume, and the top right port is open to the ambient.

1.4 Selection of Micro Actuators

The four most commonly used micro actuators are compared for the actuation of the micromachined vacuum displacement pumps: piezoelectric, electromagnetic, electrostatic, and thermopneumatic actuators [27][28]. Based on the specifications of the rough pump as discussed in the previous section, the micro actuators are expected:

i) to provide a relatively large force (>1N);
ii) to deflect on the order of microns with adequate actuation force;
iii) to have a small size;
iv) to have a low power consumption (<1W);
v) to be compatible with microfabrication.

The four types of the micro actuators are discussed in the context of these five requirements. Although the integration of the micro actuators is not the focus of this thesis, the design of the micromachined displacement vacuum pumps here is based on the appropriate actuation mechanics.

(1) Piezoelectric actuators

The power consumption of the micro actuators includes two parts: dynamic and static power consumption. The dynamic power consumption is the energy consumed for actuation transition, which relates to the electrical to mechanical energy conversion efficiency. The static power consumption is for maintaining the actuation status, which depends on the specific actuation mechanisms and whether it is fundamentally dissipative.

The static power consumption of the piezoelectric actuators, stacks or benders, is low due to their high electrical impedance. Piezoelectric stacks may generate actuation forces as high as hundreds of Newtons [9], which is favored for the pump actuation. However, the deflections of piezoelectric stacks are only approximately 0.1% of the actuator lengths. For a 10μm stroke, the actuators lengths need to be at least 10mm, which limits their use for the pump actuation due to the limited volume budget. Piezoelectric benders may have a large free deflection, but with the force applied, the deflection is very limited. Similar analysis has been done in [29]. Furthermore, piezoelectric actuators are difficult to fabricate on silicon, and can only be integrated with the pump manually die by die.

(2) Electromagnetic actuators

Electromagnetic actuators, solenoids or voice coils, may provide adequate actuation forces along with large displacements. The biggest obstacle to use electromagnetic actuators is their large static power consumption due to thermal dissipation. Also the electromagnetic actuators are relatively large in size because the coils are difficult to microfabricate and the length of the actuators are typically tens of millimeters. If we use commercially available electromagnetic coils, the actuators can be only integrated at the die level.

(3) Electrostatic actuators

Electrostatic actuators have many advantages over other micro actuators. The static power consumption and the size can be small, and the actuators can be fabricated easily on silicon wafers. Two kinds of electrostatic actuators are available, parallel plates and zipper actuators.

Parallel electrostatic plates are commonly used actuators, however, they might not provide sufficient actuation forces except when a very high voltage is applied. If the gap is 10μm between two Φ6mm circular plates, the electrostatic force is only ~12.5mN with 100 volts applied and about 1.25N with 1000 volts applied. Recall that the actuation force

needs to be larger than 1N, and thus the actuation voltage should be larger than 1000 volts.

A well developed variation of parallel electrostatic plates is the interdigitated finger (comb) structures [30][31][32]. Comb drives have been successfully used for inertial force sensing, such as the capacitive accelerometers [37], which are already commercially available. Comb-drive actuators have also been used for large displacements, e.g. a deflection of 30μm was reported in [33]. Multiple parallel electrostatic plates in the comb-drive provide an actuation force multiple times as big as that obtained by a single pair. However, the interdigitated finger structure of the comb-drive actuators is not easy to fabricate vertically as would be needed for the pump system, and most of this type of actuators are only for lateral actuation.

Electrostatic zipper actuators have a minimal gap at one end between the two electrodes, where the electrodes start to zip in. An example of an in-plane electrostatic zipper actuator is shown in [43]. The initial voltage to pull the two electrodes together, the so-called pull-in voltage, is smaller than that of the parallel plates. And with a certain actuation force, the deflection can also be sufficient to actuate the pump membranes. We consider the zipper actuators as the best choice for our pump actuation.

(4) Thermopneumatic actuators

Thermopneumatic actuators normally use a heater to elevate the temperature of a gas cavity in order to actuate the membrane. The force can be big if the temperature of the gas inside the actuation cavity is high, based on the ideal gas law. The thermopneumatic actuators may be small in size and also compatible with microfabrication of the pumping elements. However, thermally actuated actuators also have the problem in dissipating too much power due to the large temperature difference from the ambient temperature, which prevents us from considering them for our pump actuation.

The discussions of the four types of micro actuations are summarized in Table 1-2, in terms of the five major specification of the rough pump. Based on the discussion of the micro actuators, the electrostatic zipper appears most promising for pump integration, with an adequate actuation force, an acceptable deflection, low static power consumption, and microfabrication compatibility. An alternative option is to use piezoelectric stacks, and integrate the stacks with the pump manually at the die level.

The integration of the micro actuators is not part of this thesis work but design needs to be compatible with likely actuation method. The pumping element is characterized with pneumatic actuation, which is easy to set up and has no fundamental limitation for stroke

displacement except for the mechanical stops of the pump. High pressure sources and low pressure sources (vacuum) are used for testing. However, it also needs to be noted that the actuation force is proportional to the pressure difference and the area. If the pressure difference is small, especially when the pressure of the test volume is low (<200 torr), the actuation force is limited.

Table 1-2: Comparison of the four types of micro actuators for the displacement vacuum pump operation.

Micro Actuators		Force	Deflection with Force	Power	Micro-fabrication	Size
Piezo-electric	stack	large	small	low	no	large
	bender/disk	medium	small	low	yes	medium
Electro-magnetic	solenoid	medium	large	high	difficult	large
	voice Coil	medium	large	high	difficult	large
Electro-static	plate	small	small	low	yes	small
	zipper	medium	medium	low	yes	small
Thermopneumatic		large	large	high	yes	small

Good Bad

1.5 Previous Work at MIT

Our group had developed a micromachined displacement vacuum pump for the Micro Gas Analyzer project in 2009, which was archived in Sharma's Ph.D. thesis [26]. The initial implementation of the pump is shown schematically in Figure 1-5. The single-stage pump includes three pneumatic actuation ports for two sealing valves and one pumping piston. The pump chamber was designed to have a diameter of 20mm and a height of 6μm.

A silicon-on-insulator (SOI) wafer was chosen to form the moving membrane and piston of the valves and pump chamber. One SOI wafer and one double-side polished silicon wafer were fabricated by deep-reactive ion etching (DRIE) and other standard micromachining techniques. A key process was to create fillets at the corners of the membrane and the substrate, as discussed in [34], to reduce stress concentration. The SOI

wafer and silicon wafer were bonded first, and two Pyrex wafers (L1 and L4) were then bonded to the top and bottom sides. An image of the pump chip is shown in Figure 1-6 and is 30mm × 50mm × 2mm in dimension. The first iteration of pumps generated a vacuum pressure of 597 torr. The valve geometry was modified in the second iteration, and the absolute pressure was further reduced to 502 torr. These numbers are comparable to the best vacuum results ever reported of this type of pumps.

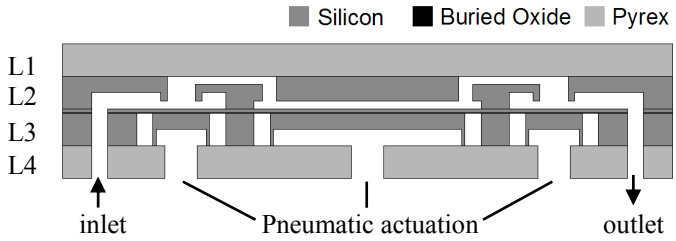

Figure 1-5: Schematic cross-section view of the initial implementation of micromachined displacement vacuum pump (reproduced from [26]).

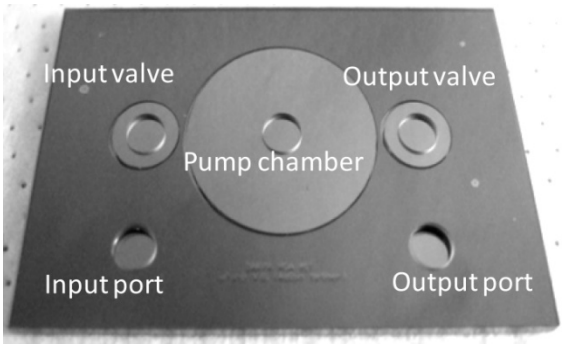

Figure 1-6: Initial micromachined displacement vacuum pump [26].

The pumps developed by Sharma validated the concept of micromachined displacement pumps for vacuum generation. A base pressure of 502 torr was achieved and a preliminary model was also built. Sharma's results indicated clear directions for improved designs, but before initiating a redesign, we conducted more detailed experiments using the Sharma's pump to further clarify directions for improvement. These experimental results are included in Chapter 4 Testing Results.

1.6 Thesis Outline

An improved micromachined displacement pump is designed, and features of the new design are demonstrated in Chapter 2. The new design focuses on minimized dead volume and better valve sealing. Chapter 3 describes the key processes to achieve the robust micro displacement pumps. Critical processes are also discussed in detail. The pumps are characterized and the testing results are discussed in Chapter 4. A testing strategy is first introduced, and the testing setup is built upon the testing plan. Testing results include the prescreening flow measurement, leakage testing results, and also vacuum generation results. Computer-aided modeling is conducted to explain the testing results and a universal actuation-independent model is developed for micromachined displacement vacuum pumps. Limits of the pneumatic actuation are revealed through the experimental testing and modeling, and a hybrid actuation testing is proposed. The thesis contributions are discussed and future development directions are suggested in Chapter 5. Additional supporting materials are contained in Appendixes.

Chapter 2

Pump Design

The pump design is based on the previous design but with some very significant modifications. The micromachined displacement vacuum pumps continue to use active valves. The dimensions of the pump chamber, the valves, and the interconnection are modified. For characterization purposes, pneumatic actuation continues to be used for characterization and the pump is designed accordingly.

The displacement diaphragm is first modeled with plate theory and numerical methods. A gas dynamics modeling principle is then described, using a computer-aided lumped element modeling approach. The fundamental expression of the final base pressure is derived through the 6-step operation cycle, and the pump is then designed.

2.1 Pump Design

The previous work at MIT provides a starting point to study the limitation of displacement pumps for vacuum generation. The vacuum performance of a micromachined displacement vacuum pump is limited by the relative sizes of the pumping volume and the dead volume, as well as the valve leakage. If a vacuum displacement pump is operated from atmospheric pressure, the generic expression for the ultimate vacuum that can be generated is (derived later this chapter):

$$P_{vacuum} = \frac{P_0 \cdot V_{dead} + P_0 \cdot Q_{leak} \cdot T}{V_{dead} + V_{pumping}}$$

where

P_{vacuum}: ultimate base pressure
P_0: atmospheric pressure (~760 torr)
Q_{leak}: leak rate (which is a function of P_{vacuum})
T: operational cycle time
V_{dead}: dead volume
$V_{pumping}$: pumping volume

The two major limiters on the vacuum generation performance of the micromachined displacement pumps are the dead volume (V_{dead}) and pump leakage (Q_{leak}). The pumps are re-designed by following two principles: reducing the dead volume and improving the valve sealing.

Dead volume of the displacement pump includes four parts: (1) channel volume (as shown in Figure 2-1); (2) un-evacuated chamber volume between the chamber piston fully pushed-up and fully pulled-down; (3) dead volume caused by non-ideal fabrication artifacts like wafer bow; and (4) virtual dead volume caused by insufficient pump chamber gas charging and discharging. Part (3) can be minimized through the fabrication process, which is to be discussed in Chapter 3. Part (4) is optimized through operation. The experimental results are reported and discussed in Chapter 4. The pump sealing can be improved with smoother valve surfaces and better tuning of the testing setup. The valve leakage is characterized in Chapter 4.

2.1.1 Pump Design Overview

The comparisons between the two generations are visually illustrated in Figure 2-1 for closed states and Figure 2-2 for open states (not to scale). In the new design, two valves and the pump chamber are normally closed in the idle state, as shown in Figure 2-1 (b). Maximum deflection occurs during pulling-down with vacuum actuation. Part (2) of the dead volume is minimized in this new design, and other features of the new design are discussed in the rest of this chapter.

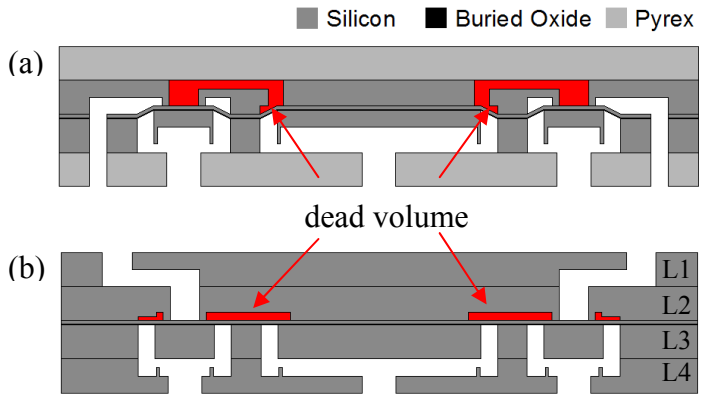

Figure 2-1: Schematic views of pumps in closed states (vacuum actuation). (a) The previous generation pump (1G pump) and (b) the new design (2G pump).

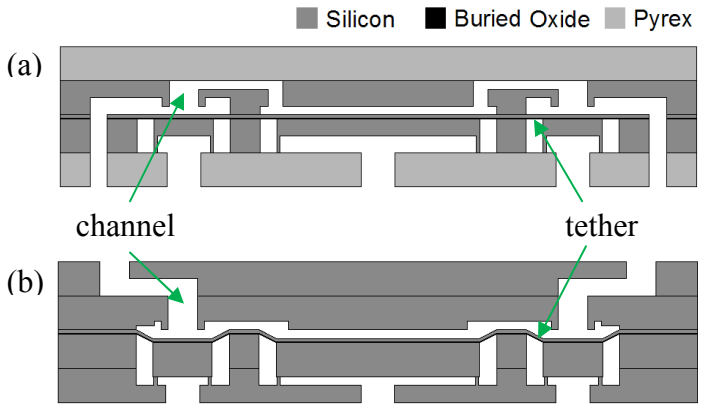

Figure 2-2: Schematic views of pumps at open states (high pressure actuation). (a) The 1G pump and (b) the 2G pump.

2.1.2 Chamber Design

The previous pump design uses a Φ20mm chamber, as shown in Figure 2-3. The circular chamber is in the middle, and two valves are next to the chamber. The green color indicates the flow path, which includes a few segments of lateral channels and four through wafer channels between the two valves.

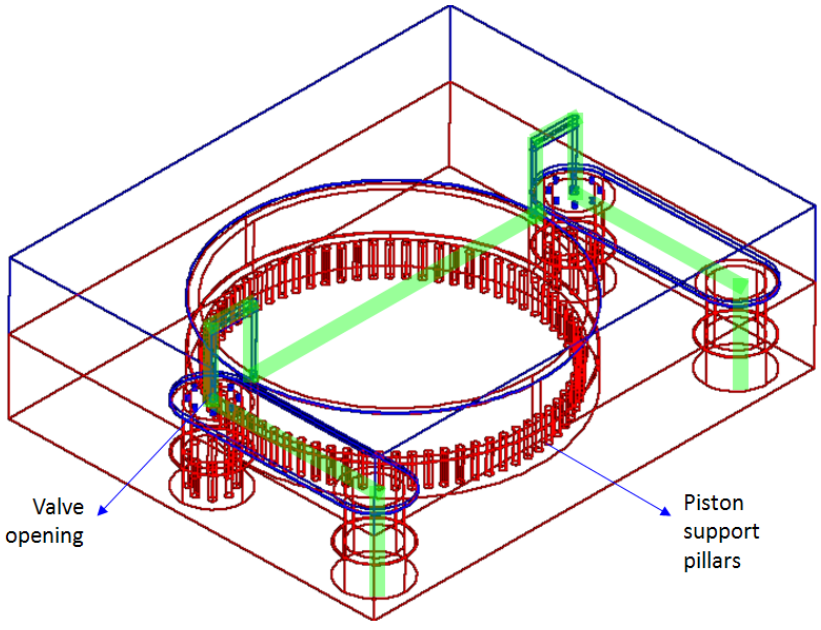

Figure 2-3: Schematic view of the previous generation pump [26].

This project requires a smaller size (less than $1cm^3$), and a smaller chamber is desired. Suppose the height of the micro rough pump is ~1cm, and thus the area for the top surface would be around $1cm^2$. For a two-stage concept, as discussed in Section 1.1, the diameter of a pump chamber is reduced to 6mm to meet the $1cm^2$ surface area requirement. The chamber area is then only 9% of that of previous pump chamber. The width of the tether, the deflection diaphragm as shown in Figure 2-2, is designed as 500μm, with a Φ5mm piston in the middle. A schematic drawing of a two-stage pump is shown in Figure 2-4. There are eight ports in total on a test chip, which is 22mm × 26mm × 2mm. One port connects to the test volume and one is open to the ambient. The other six ports are for pneumatic actuation connection.

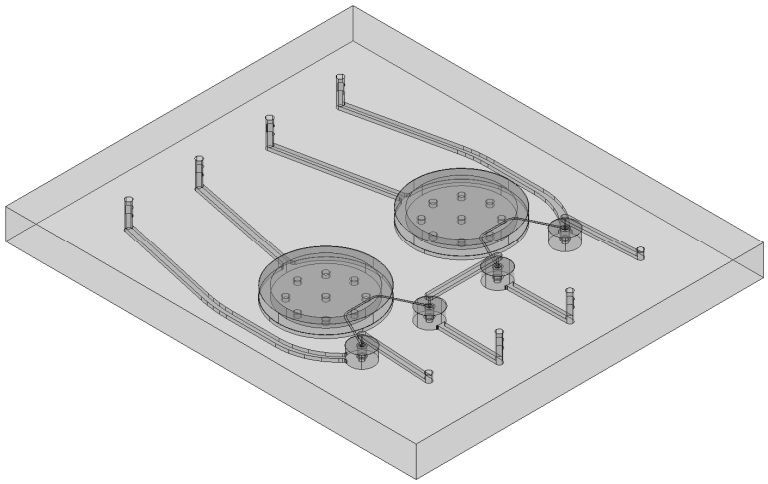

Figure 2-4: Schematic view of a two-stage micromachined displacement pump.

To study the vacuum generation performance of the micromachined displacement pumps, a single-stage pump is used first. The test chip of a single-stage pump is shown in Figure 2-5, and the fabrication details are discussed in Chapter 3. The flow path is dyed in dark green and the actuation cavities are dyed in light green. An enlarged view of a valve region is shown in Figure 2-6. The valve seat, which is defined in the following section, is highlighted in red.

The stroke of the new pump chamber is designed to be ~10μm to be compatible with the deflection capability of the micro actuators and to enable two-stage pumping to reach pressures of tens of torr. At the full deflection position, the maximum stress is ~200 MPa on tether surfaces. Weibull reference strength of silicon, which is correlated to the surface roughness, ranges from 1.2 GPa to 4.6 GPa [47], and the maximum stress of the diaphragm is 0.04~16.7% of the Weibull fracture strength, which we believe provides adequate safety margins.

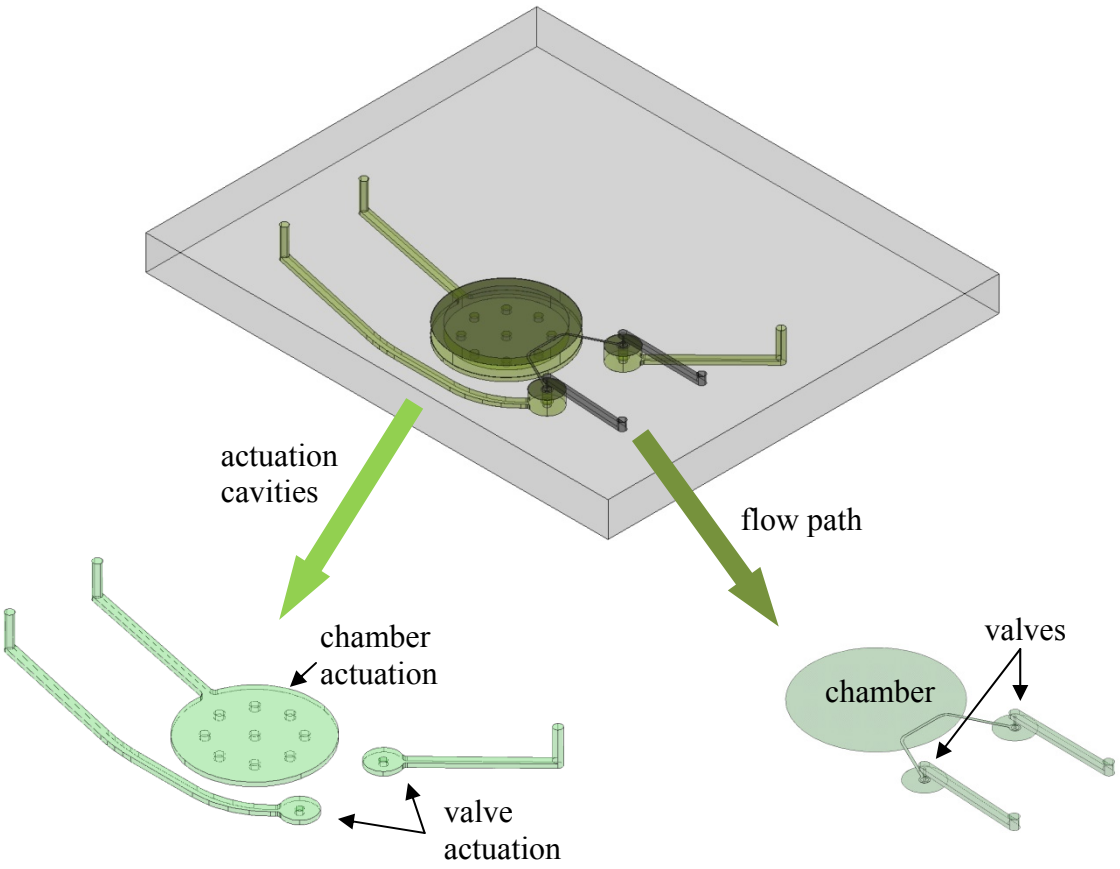

Figure 2-5: Schematic views of a single-stage micromachined displacement pump.
Lower left: actuation cavities for the chamber and two valves.
Lower right: flow path inside the test chip.

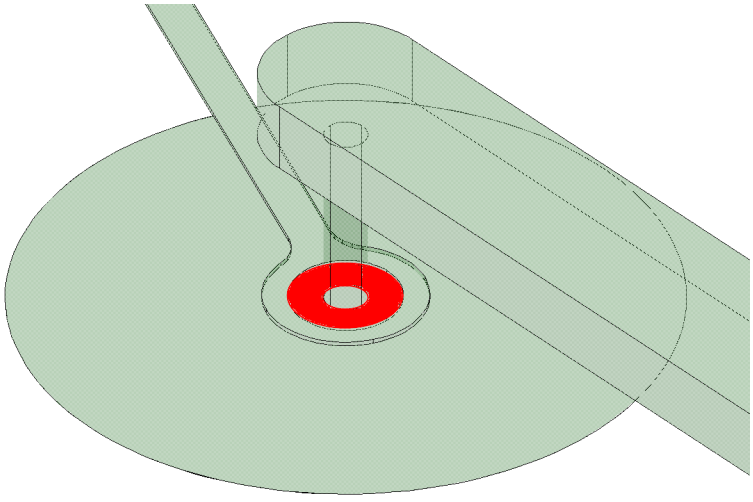

Figure 2-6: Enlarged view of a valve, with the valve seat highlighted in red.

2.1.3 Valve Design

A schematic view of the valve is shown in Figure 2-7 (a), with the valve seat and boss labeled, and a cross-sectional view is shown in Figure 2-7 (b). The valve boss is 1.5 mm in diameter, also with the 500μm wide tether. Both the valve boss and the valve seat are made of silicon, which is discussed in detail in Chapter 3. The valve tether thickness is the same as the chamber tether thickness, i.e. the thickness of the device layer of the silicon-on-insulator wafer which is 10μm. The deflection stops are also 10μm away from the valve's Φ0.5mm piston.

The valve seats are roughened to prevent accidental bonding during fabrication. The surface is treated with plasma etch, for 3 seconds to remove about 160nm silicon. Detailed fabrication processes are described in Chapter 3. The valve is sealed by high pressure actuation, and the pump is sealed by the silicon surface contacting. Variations of the valves are designed and the four types of the valves are shown in Figure 2-8. The prevalent design is the upper left design, with a Φ100μm inner hole and 40μm wide a valve seat. Other three designs share the same inner through hole diameters, but the valve seal ring width is 80μm (lower right), 120μm (upper right), or double 40μm rings (40×2, lower left). The four types of valves are measured for leakage and the results are included in Chapter 4.

2.1.4 Interconnection Design

To minimize the dead volume, the new design adopts a planar channel design. As shown in Figure 2-3, there were four vertical connecting holes between the pump chamber and the two valves in the previous design, which are through an entire wafer's thickness (~500μm). The vertical holes would be larger than 5% of the pump chamber volume for the new design, and to minimize the dead volume, there are instead only lateral connecting channels between the two valves. The channels are 10μm high and 50μm or 100μm wide, as shown in Figure 2-5. Because the pump chamber is normally closed, there is also a narrow channel in the chamber region to reduce the gas damping during chamber operation. The top view of the planar interconnect channels are shown with the chamber and the valves in Figure 2-9.

Aside from the improvements on the designs of the chamber, the valve, and the interconnection, the fluid ports are moved to the side opposite the actuators to facilitate the integration of actuation in the future development.

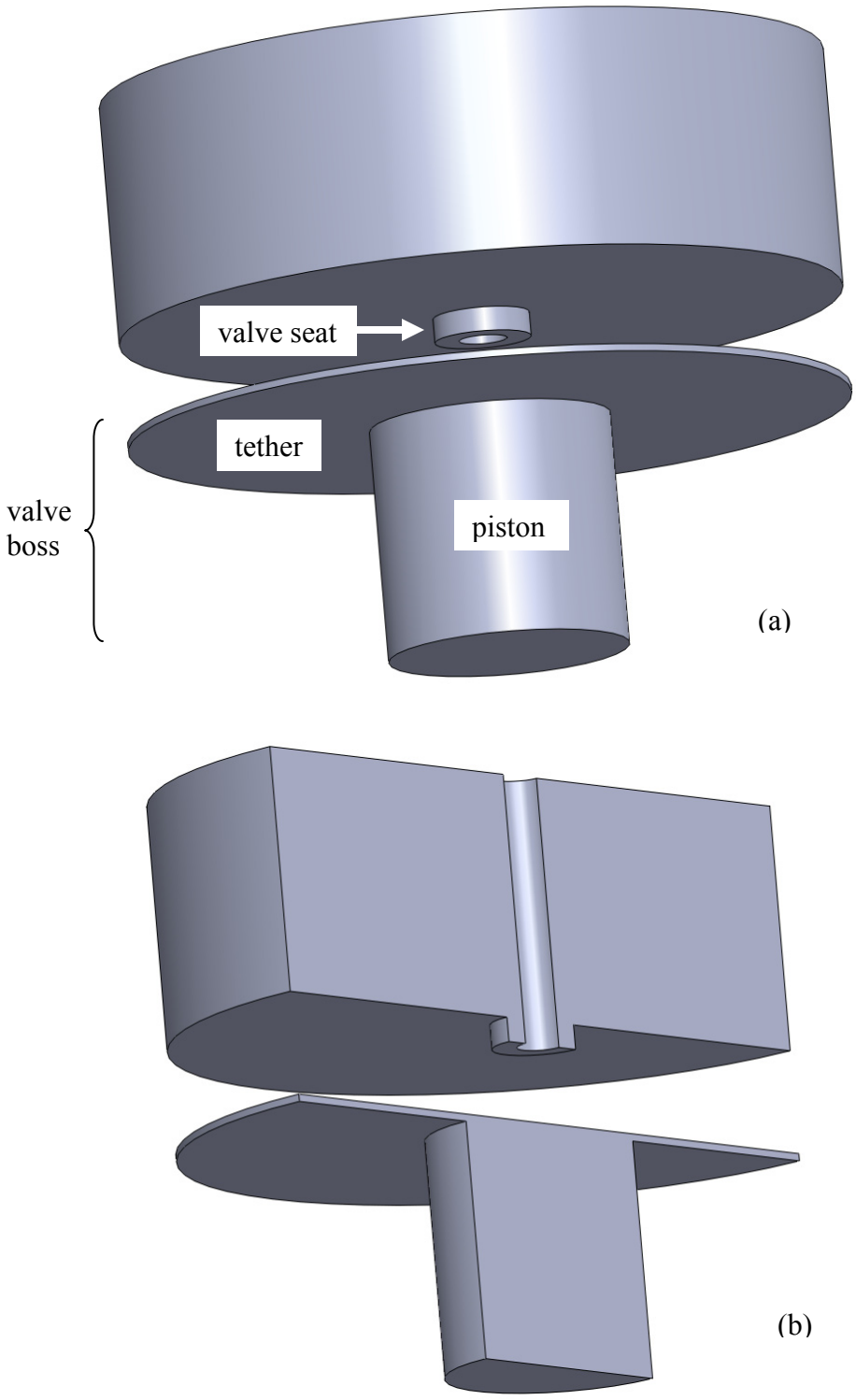

Figure 2-7: Schematic views of a pump valve. (a) 3D view, (b) cross-section.

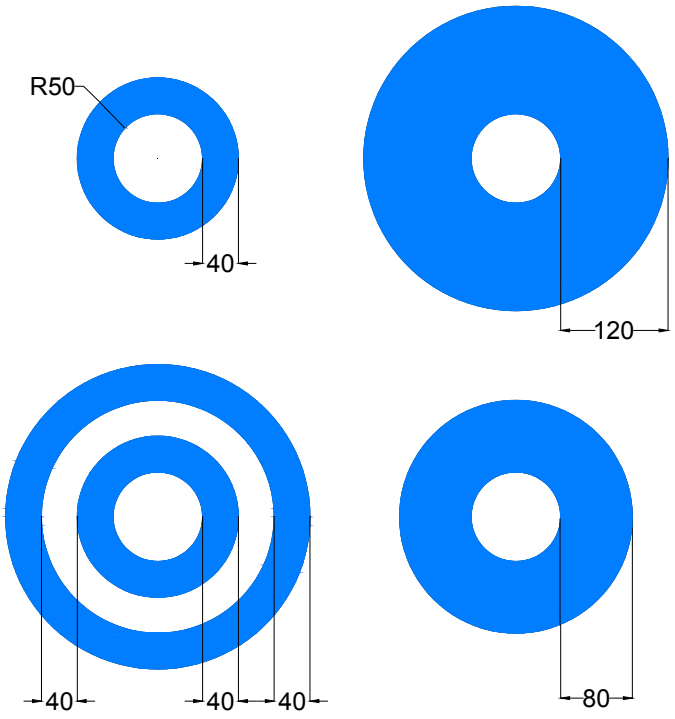

Figure 2-8: Four types of valve seats (unit: μm)

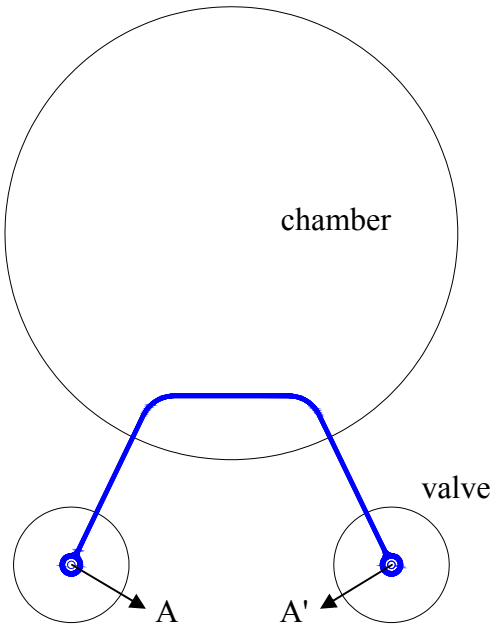

Figure 2-9: Interconnection channels (blue). The cross-section through the channel (A-A') is shown in Figure 2-1 and 2-2.

2.2 Mechanical Analysis

The deflections of the valves and the pump chamber are important to understand the pump operation. Plate theory and finite element modeling are used for the mechanical analysis.

2.2.1 Plate Theory Modeling

The valves and the pump chambers are subject to a pressure differential with pneumatic actuation through the operation as shown in Figure 2-10. The diaphragm for deflection will be about 10μm thick and the valve or chamber pistons, which are about 500μm thick, can then be assumed rigid in plate theory modeling. Thus the valve or chamber pistons are simplified to the case in Figure 2-11. Assume the valve or the chamber is open sufficiently and a uniform distributed load (pressure differential, ΔP) is applied on the diaphragm. The maximum displacement of the piston is less than 10μm as limited by the mechanical stops, which is far less than the diameter of the valve (500μm) and that of the chamber (6mm), and thus the direction of the load is simplified to be vertical. The force applied to the central rigid piston area is converted to the distributed load (F) around the diaphragm inner circle. A moment (M) ensures the zero slope boundary condition of the displacement at the inner circle. Superposition is used to calculate the piston deflections, with the plate formula for the circular plates with central holes [35]. Detailed mechanical analysis is shown in Appendix A.

The case in Figure 2-11 has specific boundary conditions. For the diaphragm, the circular plate with a central hole, the boundary conditions are:

1. $w = 0$ when $r = r_{outer}$
2. $dw/dr = 0$ when $r = r_{outer}$
3. $dw/dr = 0$ when $r = r_{inner}$

where

w: deflection;
r: position of the deflection;
r_{outer}: radius of the chamber/valve;
r_{inner}: radius of the chamber/valve piston.

The preset parameters are listed in Table 2-1 for the mechanical analysis and gas dynamics modeling.

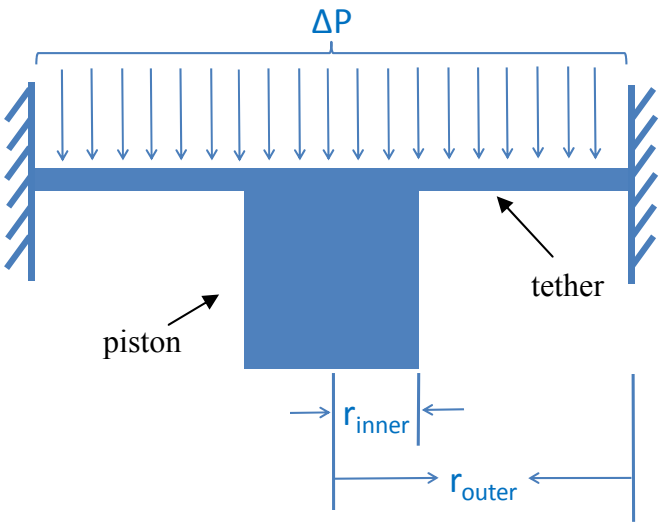

Figure 2-10: Schematic drawing for plate deflection modeling: uniform load ΔP is distributed on the top surface.

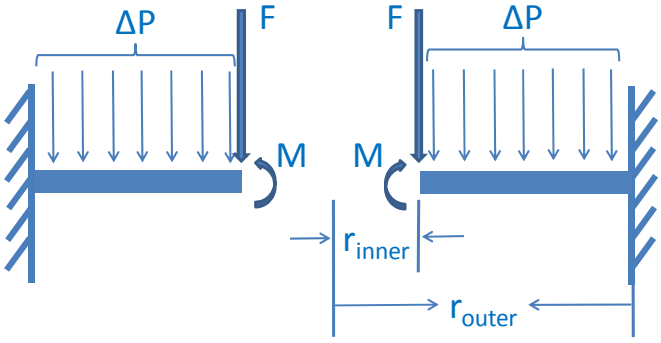

Figure 2-11: Schematic drawing for plate deflection modeling. A uniform load (ΔP) is distributed on the diaphragm and another load (F) is applied on the inner circle of the diaphragm. A moment (M) ensures the zero slope boundary condition of the displacement at the inner circle.

Table 2-1: Preset parameters for mechanical analysis and gas dynamics modeling.

Type	Piston Diameter	Piston Thickness	Tether Width*	Tether Thickness
Pump Chamber	5mm	575μm	500μm	10μm
Pump Valve	0.5mm	575μm	500μm	10μm

* Tether width = $r_{outer} - r_{inner}$.

With the preset parameters listed in Table 2-1, if the pressure differential is 100 torr, the piston deflection of the valves are calculated, with the plate theory, to be 2.14μm. The chamber piston has a deflection of 12.4μm, without considering the mechanical stops. The detailed calculation using the plate theory may refer to Appendix A.

2.2.2 Finite Element Modeling

The numerical method gives close results for the valve or chamber deflections, as shown in Figure 2-12 and Figure 2-13. With a 100 torr pressure differential, the valve and the chamber deflect 1.99 μm and 11.49 μm, respectively.

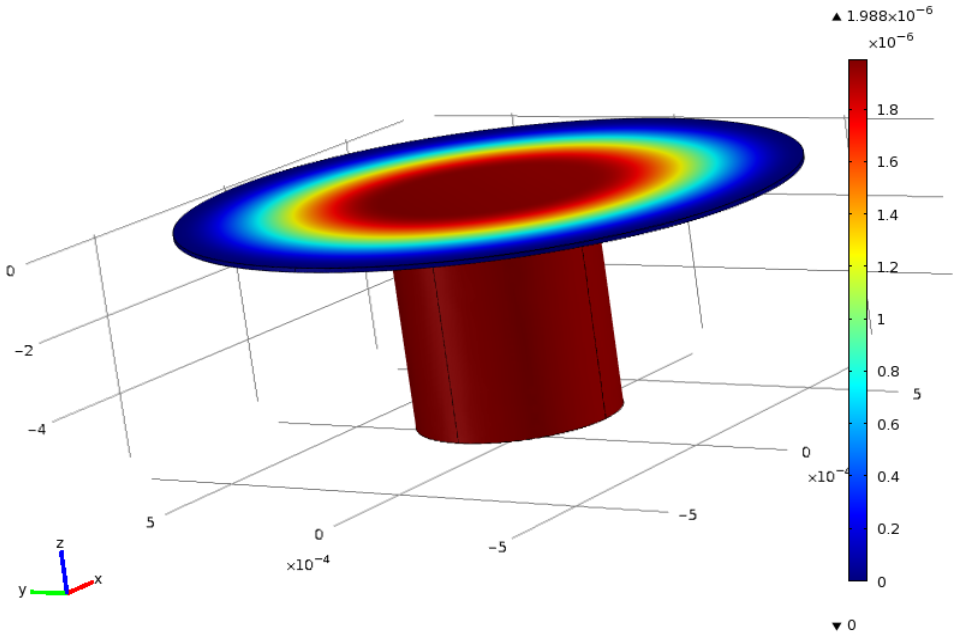

Figure 2-12: Finite element modeling results of the valve.

The FEA method is useful to verify the plate theory results, and more importantly, the numerical method can be powerful in modeling complicated geometry. For example, as described in Chapter 3 Pump Fabrication, the fillet is essential to ensure the robustness of the thin tether. The deflection is inversely proportional to the third order of the tether thickness as seen in plate theory, and the fillet would hinder the deflection. But it is difficult to calculate the deflection of the tether with fillets on both sides by using the simple plate theory formulas. The pump chamber deflection is then modeled using FEA method versus the fillet radius, as shown in Figure 2-14.

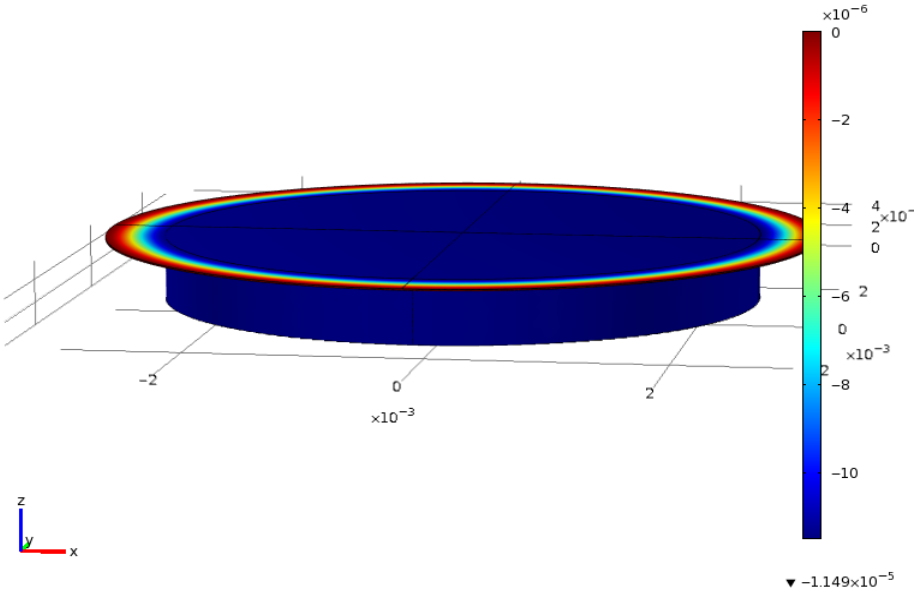

Figure 2-13: Finite element modeling results of the chamber.

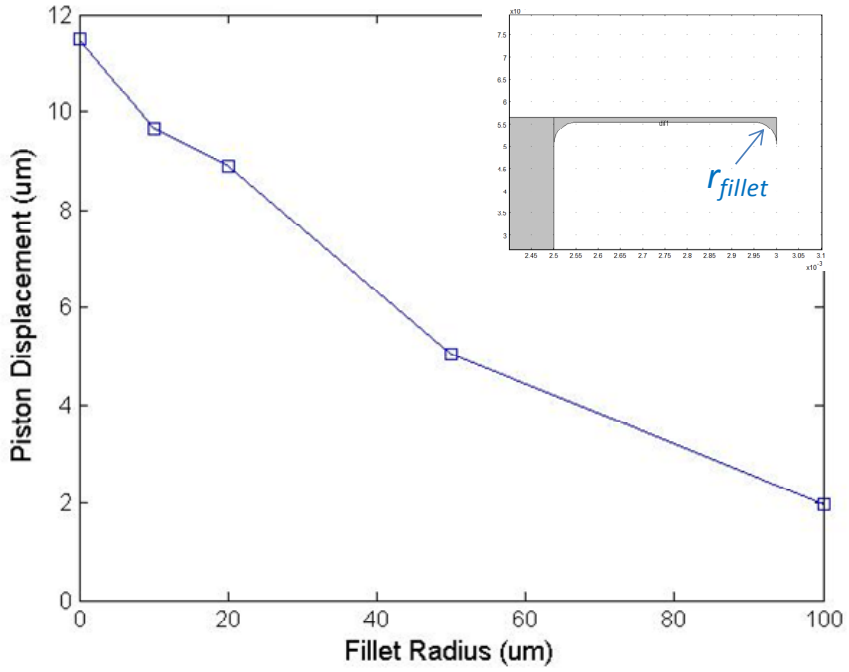

Figure 2-14: Effect of the fillet radius on pump chamber deflection. Inset: the cross-section of a tether with fillets on.

From the plot in Figure 2-14, if the fillet radius is larger than 20μm, the chamber deflection will be 20% smaller than designed. If the fillet radius is larger than 45μm, the deflection will be 50% smaller. The fillet may affect the vacuum generation performance of the micromachined displacement pumps, which will be further discussed later.

2.3 Gas Dynamics Modeling

As shown in the experimental results later in Chapter 4 (vacuum generation testing), the vacuum generation performance depends on gas charging time and it is important to understand the gas dynamics during the pumping cycle of the displacement vacuum pump. This section is to introduce the quantitative modeling method.

2.3.1 Lumped Element Modeling Method

Electrical analogy methods, or lumped element modeling methods, have been widely used to study the dynamics of MEMS devices. Simplified device representations are extracted and expressed with equivalent circuits [37][39]. The equivalent circuits can then be analyzed with an electrical simulation tool like SPICE. Compared with numerical methods, lumped modeling runs faster and reveals the direct relationship to the variables. Equivalent circuit analysis has been expanded to the fluid flow domain [40][41]. The analogous parameters are listed in Table 2-2. Lumped modeling serves very well for incompressible fluid flow, and also works for gas flow at low pressure differences [42]. As a matter of fact, a weakly-compressible flow can be assumed to be incompressible if the density changes less than 10%, i.e. the Mach number is below 0.3 [45]. As will be shown later in Section 2.4, the pressure differences are smaller than 10% in five of the six operational steps, where the incompressible fluidic modeling are adequate. And the only exception, the pre-discharging step, will be justified.

Table 2-2: Fluidic parameters and their electrical analogies (reproduced from [37]).

Energy Domain	Effort	Flow	Displacement
Electric circuits	Voltage (V_{elec})	Current (I_{elec})	Charge (Q_{elec})
Fluid flow	Pressure (P)	Volumetric flow (Q)	Volume (V)

With the electrical analogy method, the resistance and capacitance can then be derived within fluid flow domain, as they are defined in electrical circuits. Fluid resistance is defined as the effort divided by the flow, i.e. the pressure differential divided by the flow rate as shown in Eq. 2-1:

$$R = \frac{\Delta P}{Q} \ (Eq. 2-1)$$

The definition of the fluidic resistance is based on the incompressible fluid mechanics and works very well for weak compressible gas flow. For high compressible gas flow, the flow rate may be calibrated with the pressures on the two terminals. The fluidic resistance concept is widely used to characterize the microfluidic systems, but the fluidic capacitance for gas flow, on the other hand, is not as widely used. The derivation of the gas capacitance is based on the compressible flow, where the density depends on the pressure. Before we introduce the expression of the gas capacitance, let us review how the concept of capacitance is expressed in electrical circuit with the effort (voltage) and the flow (current). In electrical circuit, the capacitance can be defined as the current divided by the derivative of voltage over time, as shown in Eq. 2-2, by assuming the capacitance is time invariant:

$$I_{elec} = C_{elec} \cdot \frac{dV_{elec}}{dt} \ (Eq. 2-2)$$

where I_{elec}, V_{elec}, and C_{elec} are the electrical current, voltage and capacitance.

Similarly, we can write the expression of fluidic capacitance as in Eq. 2-3, with the effort and flow in fluid flow domain. Fluidic capacitance is also assumed not to depend on time.

$$Q = C \cdot \frac{d\Delta P}{dt} \ (Eq. 2-3)$$

The mass conservation equation relates the flow rate with the fluidic density change as shown in Eq. 2-4:

$$Q = \frac{V}{\rho}\frac{d\rho}{dt} \ (Eq. 2-4)$$

where

Q: flow rate
V: gas volume
ΔP: pressure differential
ρ: density

From Eq. 2-3 and Eq. 2-4, we have

$$C = \frac{Q}{d\Delta P/dt} = \frac{V}{\rho}\frac{d\rho}{dt}\Big/\frac{d\Delta P}{dt} \ (Eq. 2-5)$$

Along with the ideal gas law

$$P = \rho RT$$

and by assuming the pressure of the other end to be constant, we finally get the expression of the gas capacitance as shown in Eq. 2-6:

$$C = \frac{V}{P} \ (Eq. 2-6)$$

The micro vacuum pump is made of silicon with a Young's modulus as large as 170 GPa, and the pump volumes could be regarded to be rigid. Therefore, the assumption that the gas capacitance is invariant of time, as shown in Eq. 2-3, is valid.

Next, we can then have the fluidic time constant similarly, which will be used extensively in the vacuum generation modeling and leakage modeling, as the product of the fluidic resistance and capacitance, as shown in Eq. 2-7:

$$\tau = R \cdot C \ (Eq. 2-7)$$

Now that we have the basic analyzing tools, i.e. the fluidic parameters, for our lumped element modeling, the only obstacle to prevent us from developing the fully quantitative model of the gas dynamics is to obtain the values of the fluidic resistance and capacitance. Fluidic capacitance calculations are straightforward (Eq. 2-6), as long as all the assumptions can be met. Fluidic resistances for simple structures, such as rectangular channels and straight tubes, can also be calculated approximately [37], as illustrated in Appendix B. However, our pump geometry, e.g. the part between two valves, consists of not only straight channels but also a circular chamber, as shown in Figure 2-15. There is no approximate solution available for such a complicated geometry.

One way to calculate the disk resistance is using integration. The entire disk is split into finite rectangle segments, and the disk resistance is the integration of all the segment resistances:

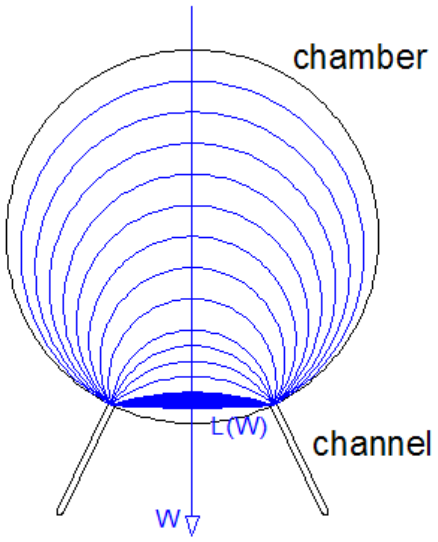

Figure 2-15: Resistance model for the pump chamber.

$$R_{chamber} = \left(\sum_W (R_W)^{-1}\right)^{-1} = \left(\sum_W \left(\frac{12\eta L(W)}{Wh^3}\right)^{-1}\right)^{-1} \quad (Eq. 2-8)$$

where

$R_{chamber}$: chamber fluidic resistance
η: viscosity of air ($\eta \approx 1.98\times10^{-5}$ *kg/m·s)*
W, L(W): as labeled in Figure 2-15
h: chamber height, ~10μm

There is a limitation though. One of the challenges to use the approximation method is how to define the finite segments. A possible set of segments is shown in Figure 2-15. However, the width of each segment changes through the total flow path, and the use of the fluidic resistance expression of simple rectangular channels may not be adequate. In this thesis, I would use a computer-aided method to derive the fluidic resistance of the complicated pump structure, which will be further used to develop the comprehensive pump model.

2.3.2 Computer-Aided Lumped Element Modeling

The single-phase fluid flow modeling is based on the Navier-Stokes equations. Computational fluid dynamics (CFD) has been around for many years. Most of the popular CFD packages use finite difference method, but finite element analysis (FEA) is also gaining more and more popularity nowadays [38].

2.3.2.1 Fluidic Resistance of Our Pump Chamber

A schematic view of the volume between two valves during the gas charging step is shown in Figure 2-16. A set of parameters, which are used for one of the pumps of this build, are used for preliminary modeling in this section.

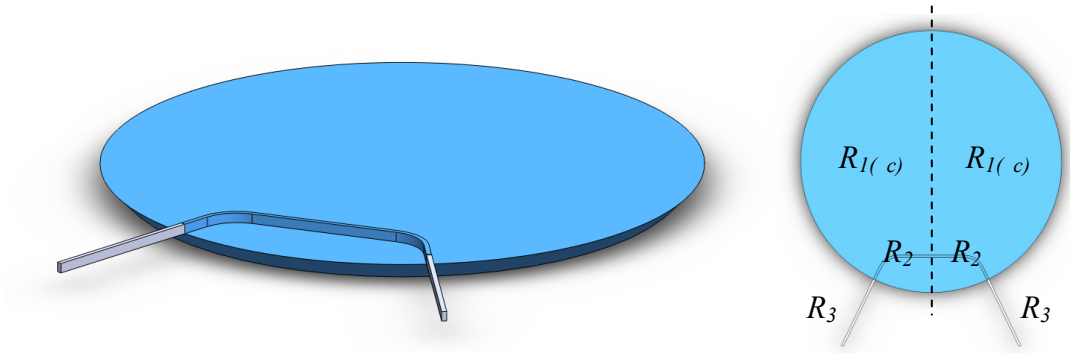

Figure 2-16: Schematic view of the pump volume between the valves.
(a) 3-D view (not to scale); (b) top view (to scale).
Blue region: pump chamber; gray regions: connecting channels.

The entire volume is split into three parts with resistances:
(1) $2R_1$ – opened chamber disk (Φ = 6mm, h = 10μm);
$2R_{1\_c}$ – closed chamber disk (Φ = 6mm);
(2) $2R_2$ – chamber channel (curved, W = 50μm, h = 10μm, mean length L = 3.16mm);
(3) $2R_3$ – two connecting channels (W = 50μm, h = 10μm, L = 1.7mm each).
The total fluidic resistance is simplified as $R_{total} = (2R_{1(\_c)} \parallel 2R_2) + 2R_3$

Also for the three parts, the capacitances are labeled as C_1, C_2, and C_3 (please note the two connecting channels have a capacitance of C_3 in total). Careful FEA modeling is conducted with adequate meshing to calculate the fluidic resistances of the three parts.

With all the parameters, the resistance of the opened chamber disk $2R_1$ is calculated with finite element modeling tool:

$$2R_1 = 0.21 \times 10^{13}\ Pa \cdot s \cdot\ m^{-3}$$

Similarly, the resistances for the channels are

$$2R_2 = 2.26 \times 10^{13}\ Pa \cdot s \cdot\ m^{-3}$$
$$2R_3 = 1.88 \times 10^{13}\ Pa \cdot s \cdot\ m^{-3}$$

The equivalent circuit diagram of the pump volume is then drawn in Figure 2-17.

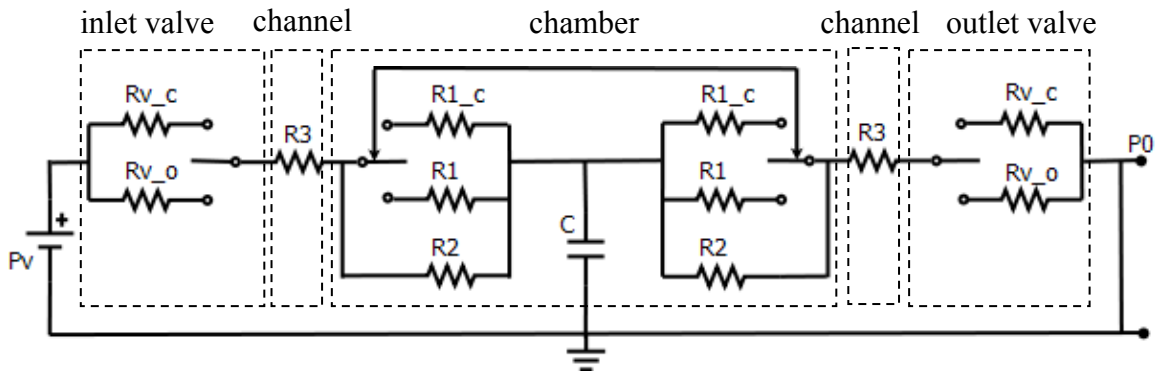

Figure 2-17: Equivalent circuit for the micromachined displacement pump.

Resistances descriptions:

R_1: a half of the open chamber; R_{1_c}: a half of the closed chamber; R_2: a half of the channel inside the chamber; R_3: a channel connecting the chamber to a valve (R_1, R_{1_c}, R_2, R_3: refer to Figure 2-13); R_{v_c}, R_{v_o}: resistances of closed or open valves.

Capacitance:

C: pump gas capacitance.

Note: the two switches in the chamber circuit move simultaneously.

The valve resistance is calculated with the equation from [42]:

$$R_{valve} = \frac{6\eta}{\pi h^3} ln\left(\frac{r_1}{r_2}\right) (Eq. 2-9)$$

where

R_{valve}: valve fluidic resistance

r_1: outer radius of valve seat (90 μm for a 40 μm wide valve seat ring)

r_2: inner radius of valve seat (50 μm)

h: gap between valve seat and valve boss

The fluidic resistance of a wide open valve with the full displacement of 10μm is

$$R_{v\_o} = 2.23 \times 10^{10}\ Pa \cdot s \cdot\ m^{-3}$$

The surface profile measurement by VEECO WYKO surface profiler shows that the 3 seconds surface roughening etches away around 0.16μm silicon, as mentioned in Section 2.1.3 and detailed in Layer 2 fabrication in Chapter 3. At the idle state, the resistance of a

valve is

$$R_{v\_idle} = 5.43 \times 10^{15}\ Pa \cdot s \cdot\ m^{-3}$$

The relationship between the resistances so far is

$$R_{v\_idle} \gg\ R_2,\ R_3 >\ R_1 \gg\ R_{v\_o}\ \ (Eq. 2-10)$$

The fluidic resistances are summarized in Table 2-3.

Table 2-3: Fluidic resistances for the pump.

Fluidic Resistances	Chamber $2R_1$	Chamber Channel $2R_2$	Connect Channels $2R_3$	Open Valve R_{v_o}
$(Pa \cdot s \cdot\ m^{-3})$	0.21×10^{13}	2.26×10^{13}	1.88×10^{13}	2.23×10^{10}

There are three states during the pump operation, as labeled in Figure 2-18: 1) fast pumping, the initial state; 2) slow pumping, the following state; and 3) quasi-static state, the final state. At the fast pumping state, the test volume pressure drops the fastest and relatively linearly. At the slow pumping state, the test volume pressure drops gradually to a steady pressure. At the final state, the test volume pressure maintains a static value, which is called quasi-static state. The base pressure achieved by the micromachined displacement pumps are the most important figure of merit for vacuum generation performance. The gas dynamics modeling will also focus on the quasi-static state, starting with the step-by-step analysis, and continuing with experimental results modeling.

As shown in Figure 2-18, the base pressures of interest in the quasi-static state is approximately 200 torr, and the capacitance is calculated with Eq. 2-6:

$$C_{total} = \frac{V_p}{P} \approx \frac{2.38 \times 10^{-10}\ m^3}{200\ torr} = 9.02 \times 10^{-15}\ m^3 \cdot Pa^{-1}$$

The pumping volume V_p is calculated with the geometry of the pump chamber (Φ6mm of the chamber and Φ5mm of the chamber piston) by assuming a simplified frustum of a cone structure, with the maximum stroke of 10μm.

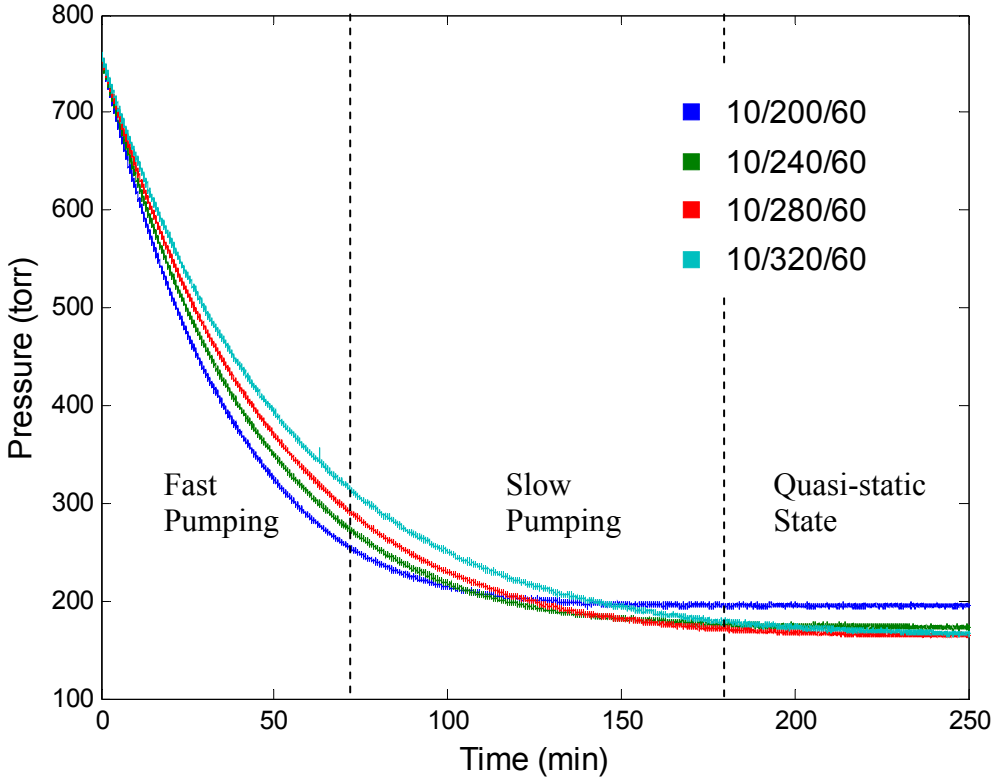

Figure 2-18: Threes states of pump operation: fast pumping, slow pumping, and quasi-static state, as marked on a family of experimental curves. Operation descriptions: e.g. 10/200/60 – valve operation times/charging time/discharging time.

2.3.2.2 Virtual Dead Volume

In the lumped element modeling, the pressure change during the gas charging step is analogous to the step response in RC circuit. A concept of virtual dead volume is then introduced as the inefficiency of chamber filling caused by insufficient gas charging time, as shown in Eq. 2-11:

$$V_d(virtual) = V_p \cdot e^{-T_c/\tau} \; (Eq. 2-11)$$

where

τ: the fluidic time constant
T_c: gas charging time
V_p: pumping volume

The concept of virtual dead volume will be used in the model for the gas pumping in the following sections. Insufficient pumping time leads to a virtual dead volume. The longer the pumping time, the less the virtual dead volume.

2.3.2.3 Leakage Modeling

The pump leakage includes two parts, inherent pump valve leak and parasitic testing apparatus leak, which will be discussed in section 4.3.3 (leakage testing). The total system leakage was evaluated by measuring the pressure change in the test volume through time, and a typical pressure transient curve is shown in Figure 2-19:

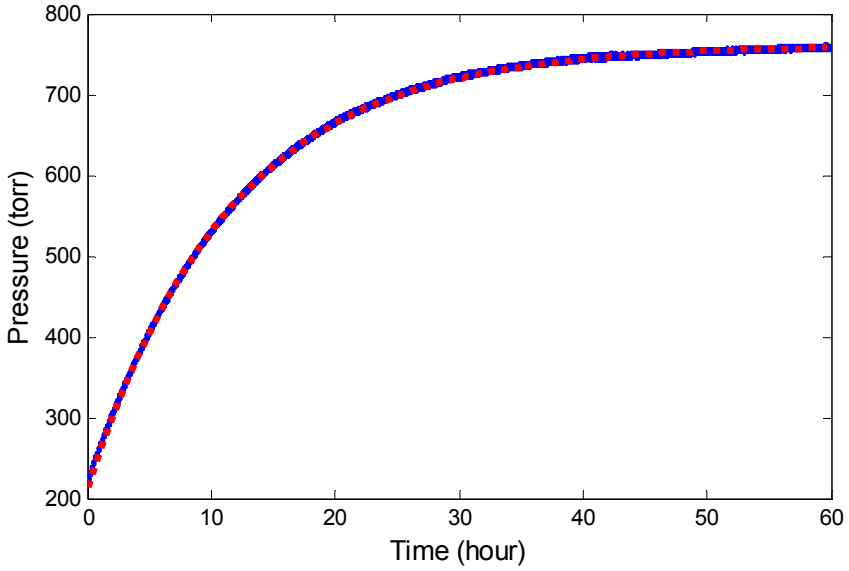

Figure 2-19: An example pressure transient curve for leak testing. Experimental results (blue) and mathematical fitting curve (red).

The pump leakage of the pump is then extracted from the pressure transient curve. With the electrical analogy method, the flow rate for a fluidic network Q equals to the pressure differential between the test volume and the atmosphere divided by the fluidic resistance.

$$Q = \frac{\Delta P}{R}, and\ \Delta P = P_0 - P_t$$

where

P_t: test volume pressure
P_0: atmospheric pressure
R: the fluidic resistance

If we assume the pressure for the flow leaked into the test volume is constantly P_0, the pressure of the test volume is then

$$V_t dP_t = \left(\frac{P_0 - P_t}{R} dt\right) \cdot P_0 \ (Eq. 2-12)$$

where V_t is the test volume. So the derivative of the pressure is

$$\frac{dP_t}{dt} = \left(\frac{P_0 - P_t}{R}\right) \frac{P_0}{V_t} \ (Eq. 2-13)$$

This equation can also be described as

$$\frac{dP_t}{dt} = -\frac{P_0}{RV_t} P_t + \frac{P_0^2}{RV_t} \ (Eq. 2-14)$$

Therefore the pressure P_t can be expressed as

$$P_t = K_0 e^{-t/\tau_{leak}} + K_P \ (\text{Eq. } 2-15\text{a})$$

where

$$\tau_{leak} = \frac{V_t}{P_0} \cdot R \quad (Eq. 2-15b)$$

K_0: a constant that relates to the starting pressure and time point

$$K_P = P_0 \quad (Eq. 2-15c)$$

With Eq. 2-15a, by matching the pressure transient curve, we can find the leakage time constant τ_{leak}, which is directly proportional to the leaking fluidic resistance as in Eq. 2-15b. The matching equation for the example curve in Figure 2-19 is

$$P_t = -546.8 e^{-t/4.162\times10^4} + 761.1$$

The time constant $\tau_{leak} = 4.162\times10^4$ seconds, with P_t in torr. This leakage time constant will be used as one way to calculate the system leakage at vacuum, which is essential to develop the full model in the next section. The test volume is estimated to be ~0.6 cm^3, and with Eq. 2-15b, the leaking resistance (closed valve, R_{v_c}) is calculated to be

$$R_{v\_c} = 1.75 \times 10^{19}\ Pa \cdot s \cdot\ m^{-3}$$

which corresponds to a gap of 10.8nm with Eq. 2-9. However, the mean free path at a pressure of 200 torr is around 250nm, which is much larger than the 10.8nm gap. The flow is not in viscous regime and Eq. 2-9 may not work, and the calculation results will not reflect the actual gap when the valve is closed. As will be shown in Chapter 3, the AFM results tell us that the mean square root of the valve surface roughness is 3.88nm, with the maximum peak to depth distance of 43nm. In addition, the leaking resistance also comprises of the parasitic leaking resistance, and the intrinsic closed valve resistance is even higher.

The fluidic resistance is proportional inversely to the third order of the height. Similarly, the resistance of a closed pump chamber is much larger than that of an opened chamber. The relationship between the resistances in Eq. 2-10 is now expanded to Eq. 2-16:

$$R_{v\_c},\ R_{1\_c} \gg R_2,\ R_3 > R_1 \gg R_{v\_o} \quad (Eq. 2-16)$$

2.4 6-Step Operation Cycle Analysis

The operation cycle of the vacuum generation experiments includes 6 steps, alternating between gas filling into the pump chamber from the test volume and gas being pressed out of the pump chamber to the outside. The 6-step cycle has been shown in Chapter 1, and here the operation will be analyzed in detail step by step for the final quasi-static state. The preset parameters listed in Table 2-1 are used for the analysis in this section.

Before we continue with the 6-step operation cycle analysis, let us have a look at the response times of the valves and the chamber piston. The damped resonant frequency ω_d, for $\omega_0 > \alpha$, is given by

$$\omega_d = \sqrt{\omega_0^2 - \alpha^2} \quad (Eq. 2-17)$$

where

ω_d: damped resonant frequency
ω_0: undamped resonant frequency
α: damping constant

The undamped resonant frequency ω_0

$$\omega_0 = \sqrt{\frac{k}{m}} \quad (Eq. 2-18)$$

And the damping constant

$$\alpha = \frac{b}{2m} \quad (Eq. 2-19)$$

where

k: spring constant
m: mass
b: damping coefficient

The spring constants are calculated with the mechanical modeling results in Section 2.2. The mass is calculated with the piston volume and density of silicon. The damping coefficient for a circular plate is given by Griffin in [46]

$$b = \frac{4.45 \cdot \eta \cdot r^4}{c^3} \quad (Eq. 2-20)$$

where

r: radius of the circular pad
c: initial squeeze-film thickness (10μm)

Table 2-4: Device constants of the pump valves and chamber.

Type	k (N/m)	m (kg)	b ($kg \cdot rad/s$)	α (rad/s)	ω_0 (rad/s)
Pump Valve	1.18×10^4	3.00×10^{-7}	0.0279	4.66×10^4	1.985×10^5
Chamber Piston	3.27×10^4	2.65×10^{-5}	7.15	1.35×10^5	3.51×10^4

The device constants are listed in Table 2-4. The undamped resonant frequency of the pump chamber is smaller than the damping constant, and the chamber is overdamped. The response of the pump chamber to an actuation of 100 torr pressure differential is drawn in Figure 2-20. The chamber piston reaches its full deflection in 2ms, which is much less than the typical chamber operation time of larger than 80ms. On the other hand, the valve is underdamped, and the damped resonant frequency and the operation

parameters are listed in Table 2-5. The valve operation time 10ms is over 300 times as big as the period time. We may then assume the valve and chamber pistons reach their full deflection instantly, and the step-by-step analysis will be based on this assumption.

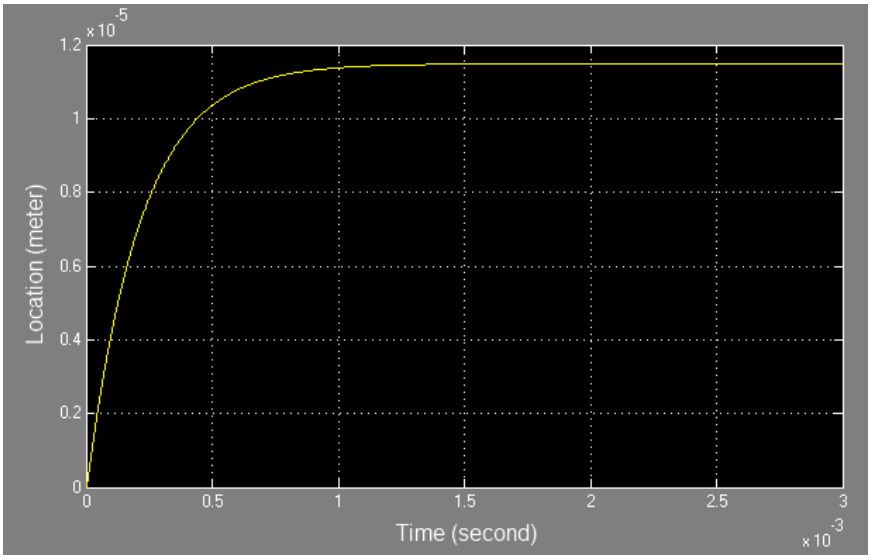

Figure 2-20: Response time of the overdamped pump chamber to a ΔP = 100 torr actuation.

Table 2-5: Operation parameters for the pump valve.

Type	ω_d **(rad/s)**	$\frac{1}{f_d}(s)$	**Operational Time (t_o)**	$\frac{t_0}{1/f}$
Pump Valve	1.93×10^{5}	3.256×10^{-5}	10 ms	307

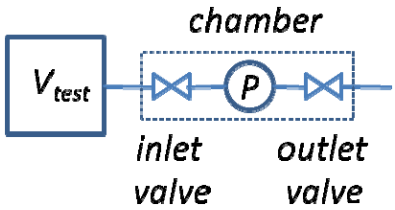

Figure 2-21: Schematic view of the pump connection.

The schematic of the pump connection is redrawn in Figure 2-21. The inlet and outlet valves are defined by the flow direction. For vacuum generation, gas flows from the test volume to the ambient. The inlet valve refers to the one in the middle of the test volume and the pump chamber, and the one connecting to the ambient is labeled as outlet valve. The six step operation has been shown in Section 1.3 and is now analyzed step by step.

Step 1: pre-charging

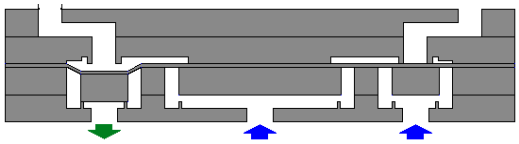

Before the chamber piston is pulled open with vacuum actuation, the inlet valve is opened first. The pump chamber and the outlet valve are assumed to be fully closed. The equivalent circuit in Figure 2-17 turns into the one in Figure 2-22 for Step 1.

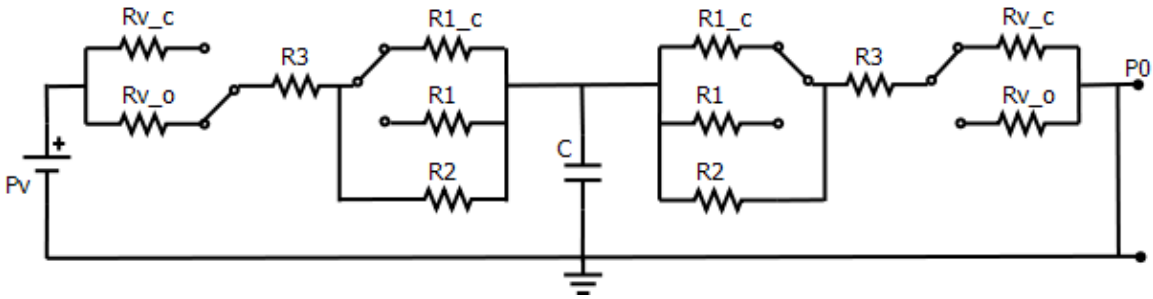

Figure 2-22: Equivalent circuit for Step 1.

For the capacitance of C, the total resistance

$$R = \left(R_{v\_o} + R_3 + R_{1\_c} \parallel R_2\right) \parallel \left(R_{v\_c} + R_3 + R_{1\_c} \parallel R_2\right)$$

With the relationship in Eq. 2-16, R_{v_c}, $R_{1\_c} \gg R_2$, $R_3 > R_1 \gg R_{v\_o}$, the resistance is then simplified into

$$R \approx R_{v\_o} + R_3 + R_{1\_c} \parallel R_2 \approx R_{v\_o} + R_3 + R_2$$

The equivalent circuit is simplified into Figure 2-23. The resistance comprises of three parts: (i) the open valve resistance R_{v_o}; (ii) the connecting channel resistance R_3; (iii) the pump channel resistance R_2. The values of the resistances are listed in Table 2-3, and the

total resistance is then approximately

$$R(step\ 1) = R_{v\_o} + R_3 + R_2 = 2.07 \times 10^{13}\ Pa \cdot s \cdot m^{-3}$$

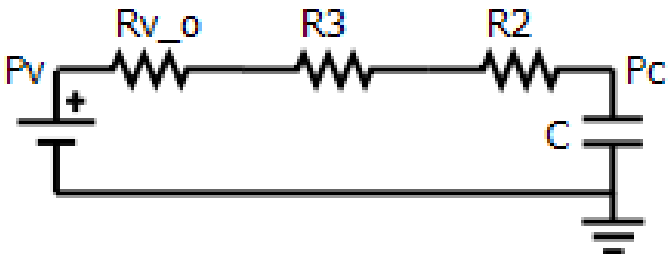

Figure 2-23: Simplified equivalent circuit for Step 1.

The capacitance at 200 torr is

$$C(step\ 1) = \frac{V(channels)}{P} = \frac{3.28 \times 10^{-3}\ mm^3}{200\ torr} = 1.233 \times 10^{-16} m^3 \cdot Pa^{-1}$$

The time constant for step 1 is

$$\tau(step\ 1) = R(step\ 1) \times C(step\ 1) = 2.55\ ms$$

During Step 1, the gas inside the test volume flows into the channels, and also there is gas leaking into the pump with a pressure of P_0 (atmospheric pressure). From the mass conservation equation for ideal gas, the pressure inside the test volume, as well inside the channels, P_1 gets an expression as Eq. 2-21. Note that the pressure inside V_d is the atmospheric pressure P_0 at the beginning of the cycle.

$$P_1(V_t + V_d) = P_i V_t + P_0 V_d + P_0 Q t_1\ (Eq. 2-21)$$

where

P_1: test volume pressure after Step 1
V_t: test volume
V_d: dead volume
P_i: test volume pressure before Step 1
P_0: atmospheric pressure (760 torr)
Q: leak rate
t_1: duration of Step 1

The two valves are designed identical, and the pressure differential between the two sides of a closed valve is relatively steady through the cycle. Therefore, to simplify the analysis, we assume the leak rate is constant through the 6-step operation.

Step 2: gas charging

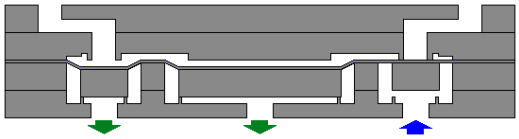

In this step, the pump chamber is pulled open with vacuum actuation while keeping the inlet valve open. Gas fills into the chamber, and is to be compressed out in the following steps. This step can be simplified to a simple gas charging process and the equivalent circuit turns into Figure 2-24.

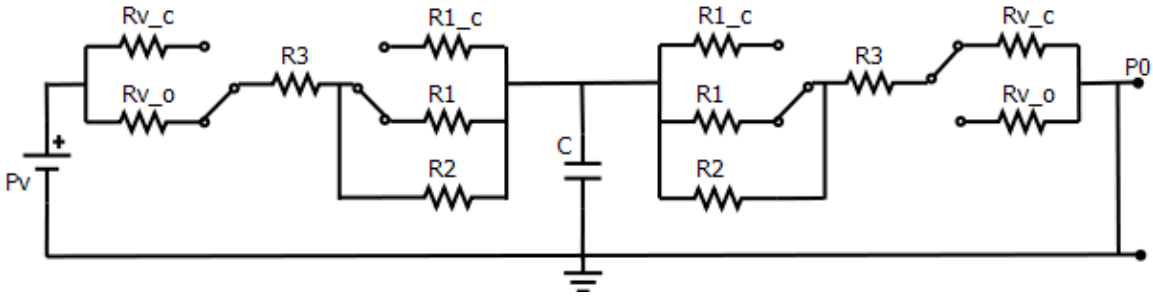

Figure 2-24: Equivalent circuit for Step 2.

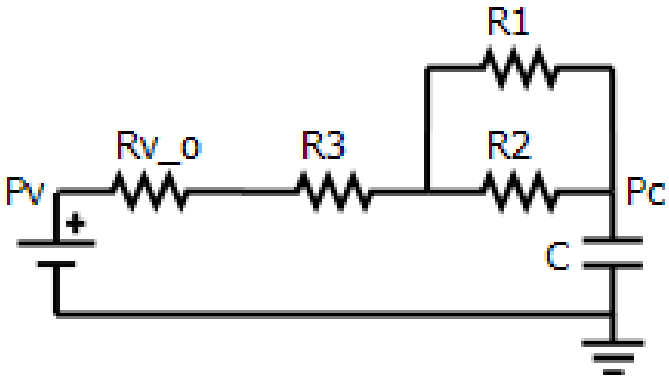

Figure 2-25: Simplified equivalent circuit for Step 2.

With Eq. 2-16, the equivalent circuit is simplified into Figure 2-25, and the total resistance is

$$R(step\ 2) = R_{v\_o} + ((R_1 \parallel R_2) + R_3) = 1.04 \times 10^{13}\ Pa \cdot s \cdot m^{-3}$$

The capacitance at 200 torr is approximately that of the opened chamber:

$$C(step\ 2) \approx C_{chamber}(200\ torr) = 8.95 \times 10^{-15}\ m^3 \cdot Pa^{-1}$$

The gas charging time constant is then

$$\tau(step\ 2) = R(step\ 2) \times C(step\ 2) = 93.1\ ms$$

Similarly as in Step 1, we can derive the expression for test volume pressure after Step 2 as in Eq. 2-22.

$$P_2(V_t + V_d + V_p) = P_i V_t + P_0 V_d + P_0 Q(t_1 + t_2) \quad (Eq.\ 2-22)$$

where

P_2: test volume pressure after Step 2
V_p: pumping volume
t_2: duration of Step 2

The gas charging step is the most important step limiting the vacuum generation of the micromachined displacement micro pumps, and extensive analysis will be conducted with the experimental results in the following section.

Step 3: post-charging

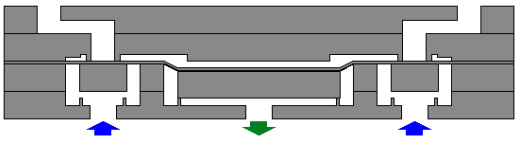

After the gas charging step, the inlet valve is closed. Leakage continues to contribute to the increase of the pressure inside the pump. Air leaks into the chamber and then the test volume, through outlet valve and inlet valve. If we simplify the leaking process and assume the pressures in the chamber and in the test volume to be equal, the test volume pressure will be:

$$P_3(V_t + V_d + V_p) = P_2(V_t + V_d + V_p) + P_0 Q t_3 \ (Eq. 2-23)$$

where

P_3: test volume pressure after Step 3

t_3: duration of Step 3

Step 4: pre-discharging

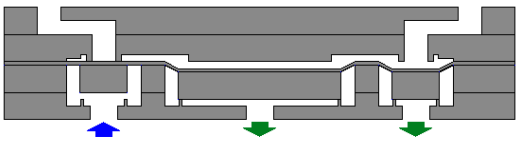

Before the gas is compressed out of the pump chamber into outside, the outlet valve is open, and a backflow occurs. If we assume the gas resistances calculated with incompressible fluidic flow modeling method are valid, the equivalent circuit then turns into Figure 2-26. The simplified equivalent circuit is similar to that in Step 2, as shown in Figure 2-27.

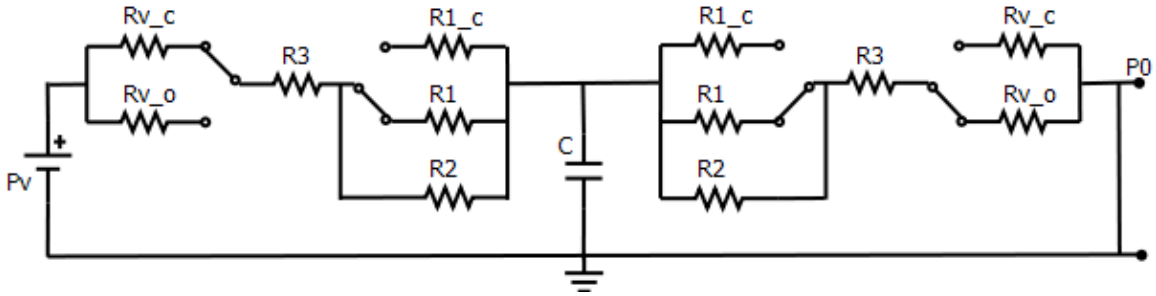

Figure 2-26: Equivalent circuit for Step 4.

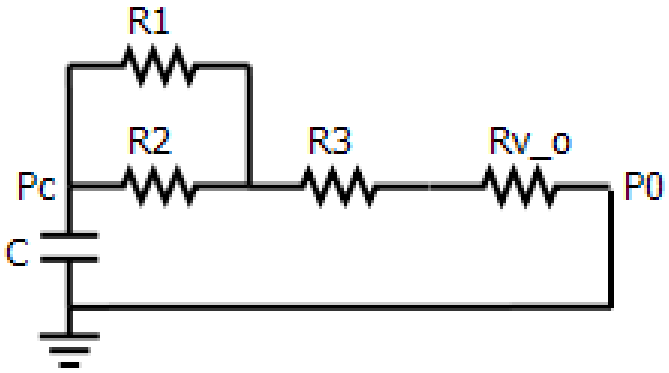

Figure 2-27: Simplified equivalent circuit for Step 4.

The capacitance is calculated based on ambient pressure 760 torr.

$$C(step\ 4) \approx C_{chamber} = \frac{V(chamber)}{P_0(760\ torr)} = 2.36 \times 10^{-15}\ m^3 \cdot Pa^{-1}$$

$$\tau(step\ 4) = R(step\ 4) \times C(step\ 4) = 24.5\ ms$$

Note that the gas resistance calculations here are based on the incompressible flow model, however, the pressure difference is larger than 10% and the model has to be modified. On the other hand, the combination of the operational times for Step 4 and 5 are typically between 50ms and 90ms, which are larger than twice the $\tau(step\ 4)$, and the discharging could be assumed to be complete.

The pressure in the pump chamber increases because of the back flow, which allows gas leak into the test volume via the inlet valve. The leakage in this step is taken into consideration together with the one in the following Step 5 later for the development of the fundamental base pressure equation. To simplify the analysis, the leak rate "Q" uses the average value through the 6 steps.

Step 5: gas discharging

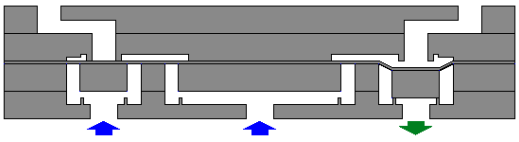

The gas chamber is closed with a positive actuation to compress the gas out into atmosphere. The equivalent circuit for Step 5 turns into Figure 2-28. Based on Eq. 2-16, the simplified equivalent circuit is shown in Figure 2-29.

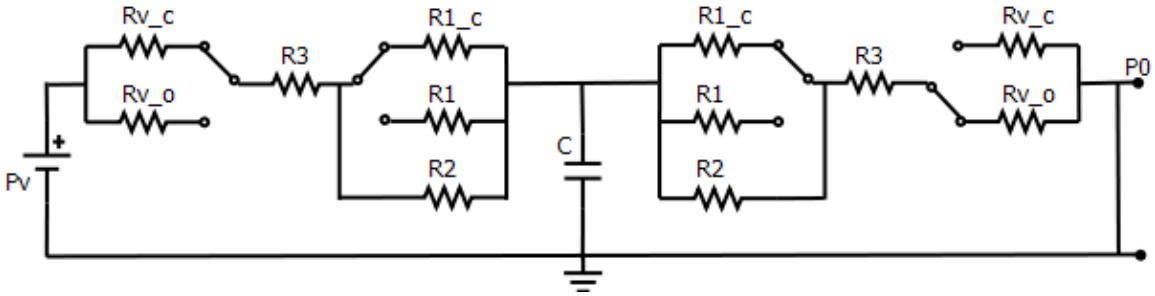

Figure 2-28: Equivalent circuit for Step 5.

The resistance for the flow is similar with that in Step 1, and the capacitance is estimated with the new pressure, 760 torr.

$$C(step\ 5) = \frac{V(channels)}{P} = \frac{3.28 \times 10^{-3}\ mm^3}{760\ torr} = 0.324 \times 10^{-16} m^3 \cdot Pa^{-1}$$

and $\tau(step\ 5) = R(step\ 5) \times C(step\ 5) = 0.67\ ms$, which is far less than the operational gas discharging time that we set (>80 ms).

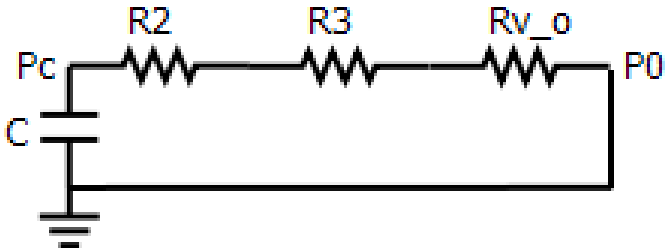

Figure 2-29: Simplified equivalent circuit for Step 5.

For Step 4 and Step 5, air leaks directly into the test volume, and the test volume pressure at the end of Step 5 is

$$P_5 V_t \approx P_3 V_t + P_0 Q(t_4 + t_5)\ (Eq. 2-24)$$

where

P_5: test volume pressure after Step 5

t_4, t_5: duration of Step 4 & 5

Step 6: post-discharging

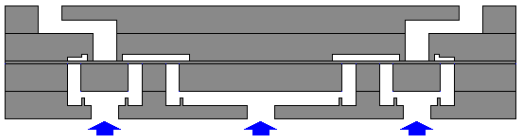

After gas discharging step, the outlet valve is closed again and the pump is ready for the next cycle operation. Chamber pressure is assumed to be atmospheric pressure during Step 6, and thus there is air leaking into the test volume.

$$P_6 V_t = P_5 V_t + P_0 Q t_6\ (Eq. 2-25)$$

where

P_6: test volume pressure after Step 6

t_6: duration of Step 6

From the Eqs. 2-21~25, we can have

$$P_6V_t = P_3V_t + P_0Q\sum_{i=4}^{6} t_i$$
$$= \frac{V_t}{V_t + V_d + V_p}\left(P_iV_t + P_0V_d + P_0Q\sum_{i=1}^{3} t_i\right) + P_0Q\sum_{i=4}^{6} t_i \quad (Eq.2-26)$$

A final equation to complete the analysis is the quasi-static equation:

$$P_6 = P_i = P_v \ (Eq.2-27)$$

where

P_v: the ultimate base pressure (vacuum pressure).

Eq. 2-26 turns into

$$P_vV_t = \frac{V_t}{V_t + V_d + V_p}(P_vV_t + P_0V_d) + P_0Q\left(\frac{V_t}{V_t + V_d + V_p}\sum_{i=1}^{3} t_i + \sum_{i=4}^{6} t_i\right) \quad (Eq.2-28)$$

Furthermore,

$$\frac{V_t}{V_t + V_d + V_p}P_v(V_d + V_p)$$
$$= \frac{V_t}{V_t + V_d + V_p}P_0V_d + P_0Q\left(\frac{V_t}{V_t + V_d + V_p}\sum_{i=1}^{3} t_i + \sum_{i=4}^{6} t_i\right) \quad (Eq.2-29)$$

If we assume $V_t \gg V_d + V_c$, which is true for our micro pump, Eq. 2-29 will become the fundamental equation we use to do the experimental results modeling:

$$P_v = \frac{P_0 \cdot V_d + P_0 \cdot Q_{leak} \cdot T}{V_d + V_p} \ (Eq.2-30)$$

where

T: operational cycle time, i.e. the sum of t_1 to t_6;
Q_{leak}: leak rate.

2.5 Summary

The design of the micromachined displacement pump is discussed in this chapter, with the aids of mechanical analysis and gas dynamics modeling. Plate theory and finite element modeling are used for mechanical analysis. Computer-aided lumped element modeling is adopted for gas dynamics modeling. The operation cycle is also analyzed, and the fundamental equation to describe the vacuum generation performance of this type of pumps is derived.

The schematic drawing of a two-stage micromachined displacement pump is shown in Figure 2-30. A single stage is about 8 mm × 10 mm in top surface area with 1 mm edges on all sides. For the demonstration of the micromachined displacement pumps for vacuum generation, single-stage pumps are first built and tested. Analysis and modeling are further developed based on the testing results and operation of single-stage pumps in Chapter 4.

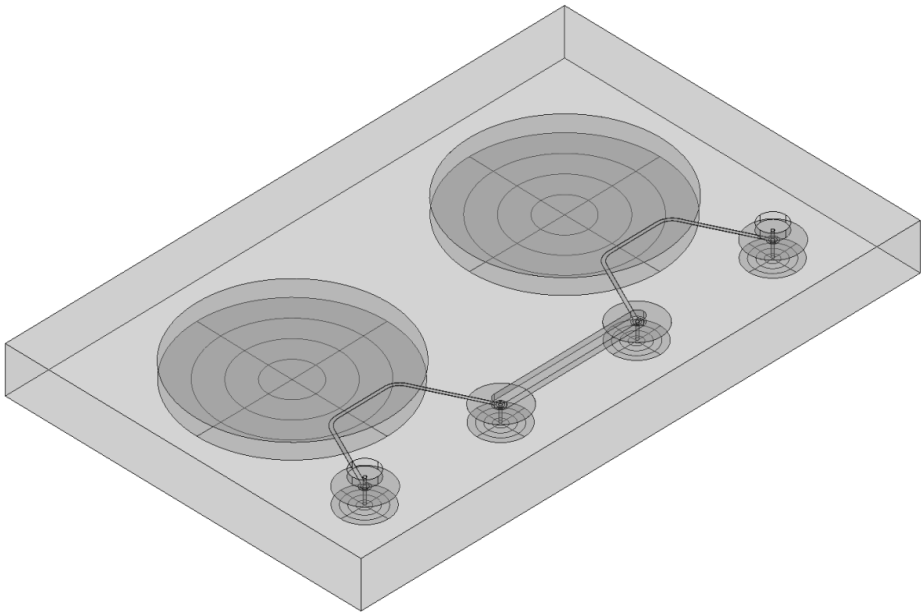

Figure 2-30: Schematic drawing of a two-stage micromachined displacement pump.

Chapter 3

Pump Fabrication

3.1 Introduction

As shown in Chapter 2, the micromachined displacement pump comprises of four layers, and the role of each layer is summarized as below:

Layer 1: connecting the valves to the ambient via through holes;
Layer 2: valve seats and chamber ceilings, with through holes connecting to Layer 1;
Layer 3: valve bosses and chamber floors, with deflection tethers;
Layer 4: pneumatic actuation channels and mechanical deflection stops.

The four layers are assembled by direct silicon fusion bonding, and thus all the layers start with double-side polished wafers. Aside from the need of polished to bondable surfaces, the third layer also functions as the displacement component, which is actuated pneumatically. Therefore, a SOI wafer with a 10μm thick device layer is chosen for Layer 3. The SOI handle layer is 575±25μm thick, and the silicon wafers used for the other three layers have thicknesses of 450±10μm.

3.2 Fabrication Process

The four layers are fabricated by deep-reactive ion etching (DRIE) and other standard micromachining techniques. The cross-section of the displacement pump is shown again in Figure 3-1. The process flows are described in this section, and details are attached in Appendix C.

DRIE is conducted with ICP etcher from Surface Technology Systems (which is SPTS now). Lithography is done with Electronic Vision contact aligner, with thick resist (AZ 4620) and thin resist (OCG 925) spin casted. Wafer bonding is done with Electronic Vision aligner and bonder.

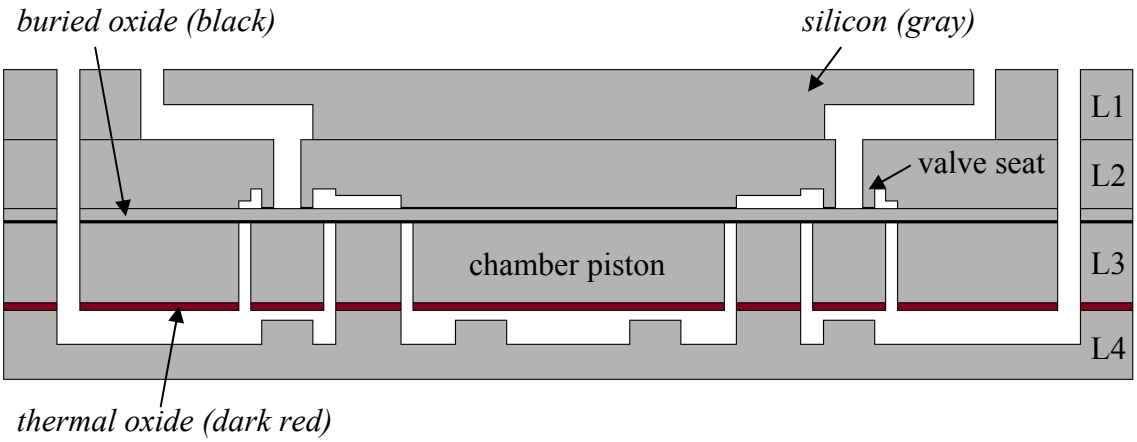

Figure 3-1: Cross-section of the micromachined displacement pump.
Gray: silicon; black: buried oxide layer; dark red: thermal oxide.

1. Layer 1

The process flow for Layer 1 is shown in Figure 3-2.

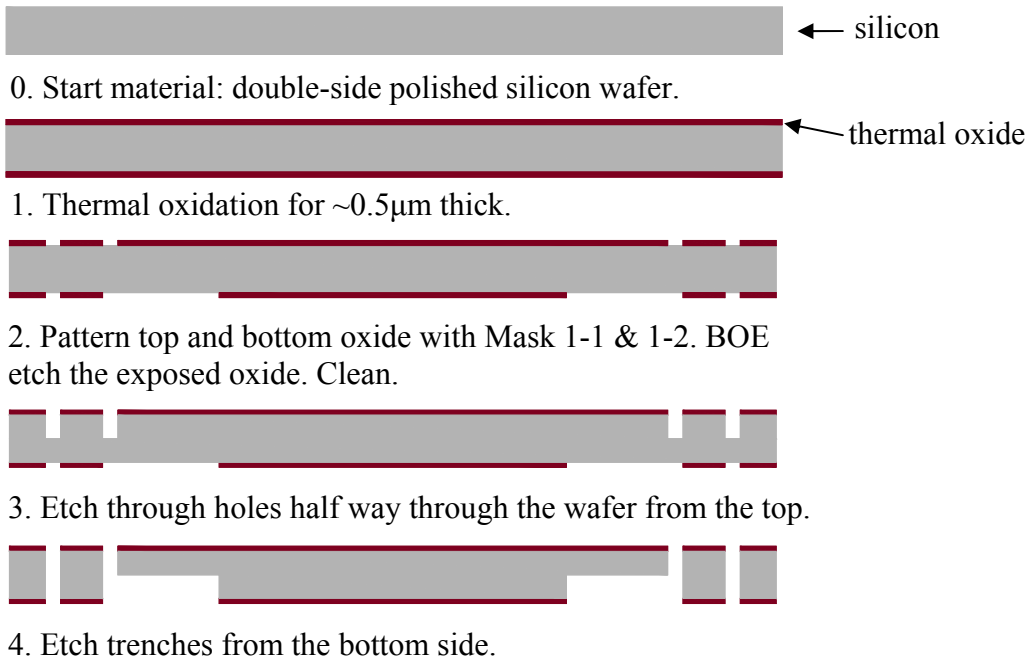

Figure 3-2: Process flow for Layer 1.

2. Layer 2

The second layer starts with a DSP wafer. The process flow is shown in Figure 3-3. There are four dry etch steps: 1) shallow etch to prevent accidental bonding between the valve seats on Layer 2 and the opposite silicon surface on Layer 3; 2) another shallow etch to offset the valve seats with their surrounding area; 3) through etch the connecting holes; and 4) etch ~10μm connecting channels between valves and chambers.

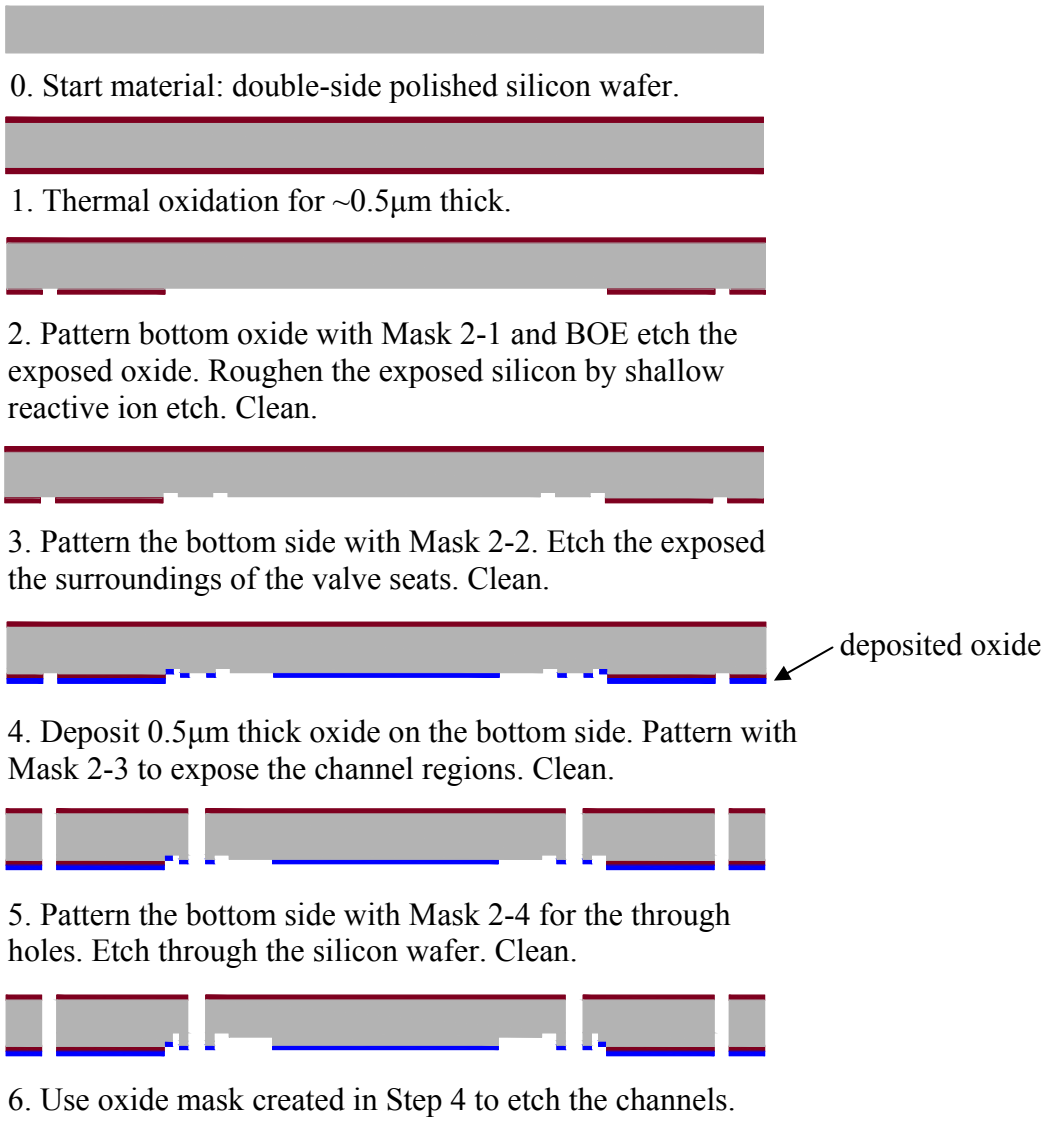

Figure 3-3: Process flow for Layer 2.

3. Layer 3

Layer 3 is to fabricate the thin deflection membrane. This layer starts with SOI wafer with a device layer of 10μm. A layer of thermal oxide is protected through the fabrications with deposited nitride. The nitride will finally be removed right before the wafer bonding. It is critical to form the tether fillets, with the fillet width ~50μm, to ensure robust deflection membranes. The fabrication flow is shown in Figure 3-4.

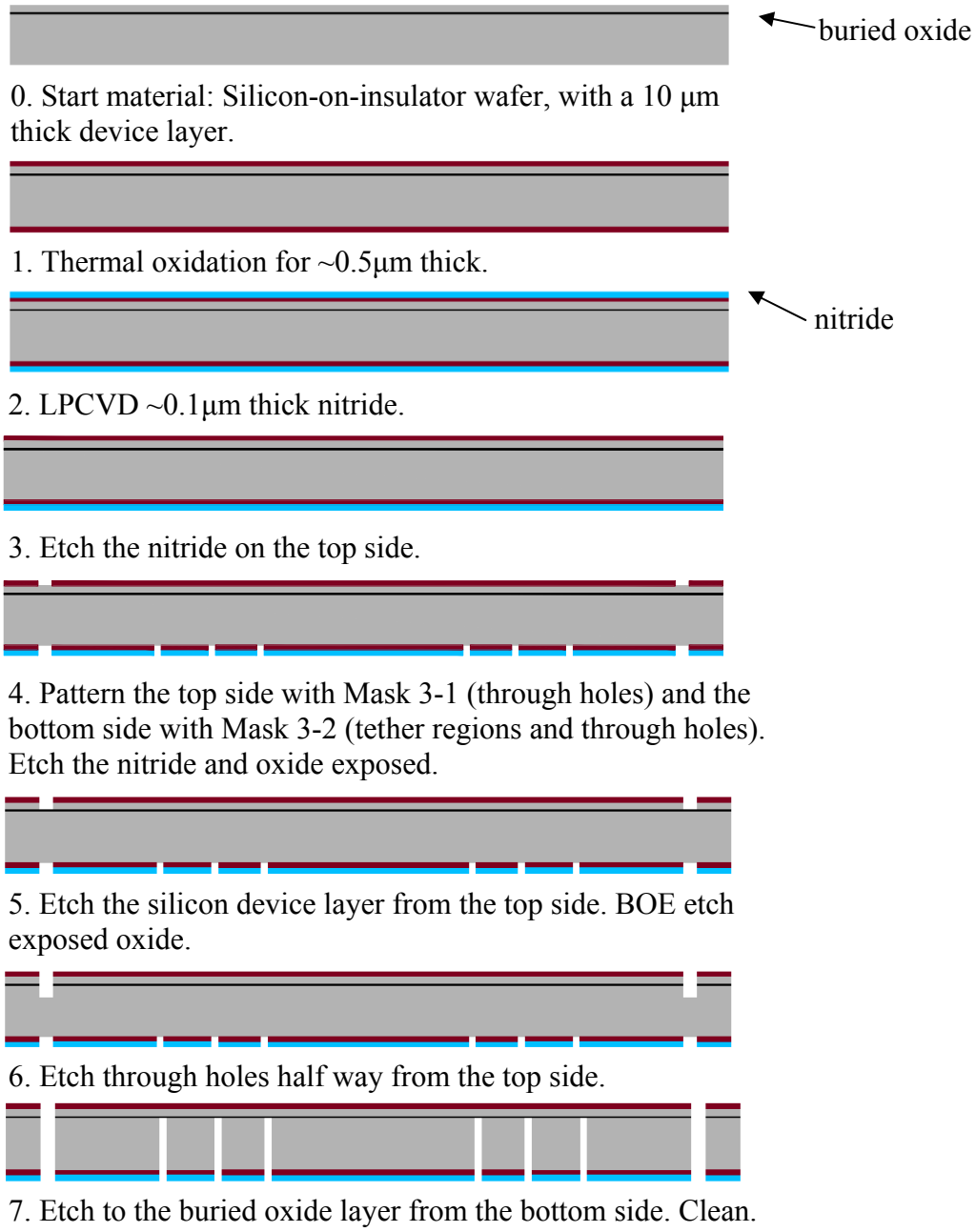

Figure 3-4: Process flow for Layer 3.

4. Layer 4

The bottom layer is to form the actuation cavities with deflection stops. The cavities are etched first, and another 10μm is etched away to reach the deflection stops. The process flow is shown in Figure 3-5.

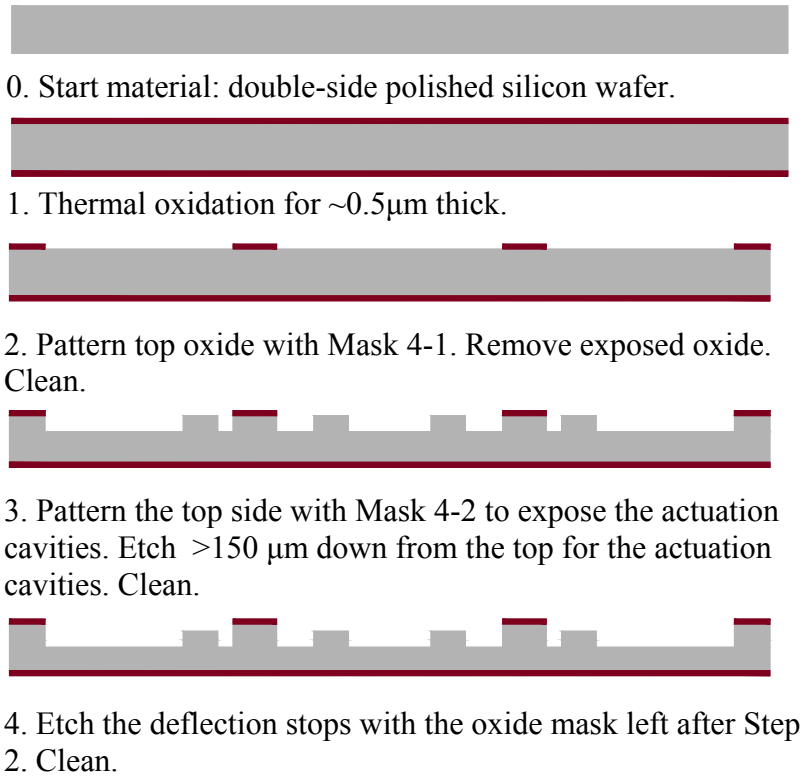

Figure 3-5: Process flow for Layer 4.

5. Assembly

The final assembly includes oxide and nitride removal, wafer cleaning, and wafer bonding. The process flow is shown in Figure 3-6. The four layers are cleaned first, and the oxides are removed next. Note that the oxide on the bottom of Layer 3 is left behind due to the protection from LPCVD nitride, which is used to compensate the stress caused by the buried oxide layer. The nitride on Layer 3 is removed next. After a RCA clean step, the four wafers are aligned. The wafer stack is compressed at 2500 N and then annealed at 1000^{o}C under nitrogen ambient for one hour. The test dies are obtained after the final dicing.

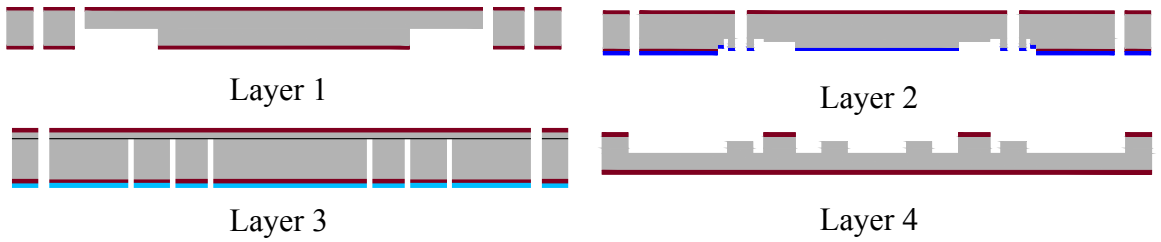

0. Start. All four layers are cleaned.

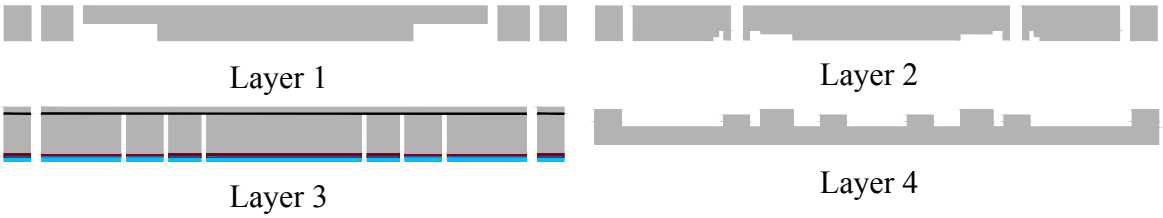

1. Remove oxide with diluted hydrofluoric acid.

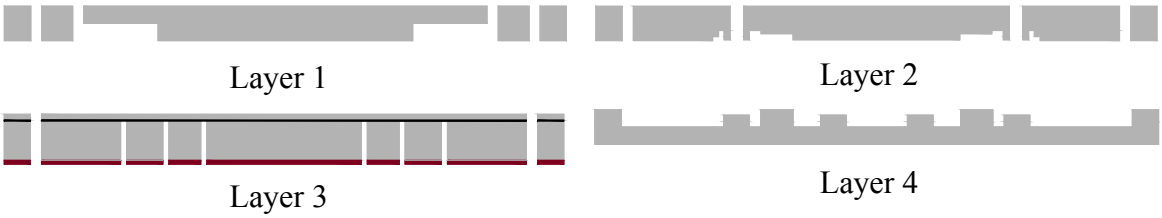

2. Remove nitride on Layer 3.

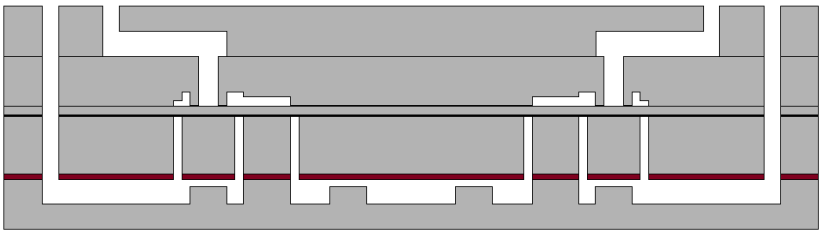

3. Fusion bonding after RCA clean.

Figure 3-6: Process flow for assembly.

The wafer stack after bonding step is inspected under infra-red camera, and the IR image is shown in Figure 3-7. The variation of the 20 test dies is discussed in the next section. The fabricated dies are shown schematically in Figure 3-8 with top and bottom views, layer by layer. Besides, the images of actual chips are shown on the side. A typical assembled test die is shown in Figure 3-9, with a single valve next to a single-stage pump. The valves will be used to study the valve sealing, and the single-stage pump is to be tested for vacuum generation.

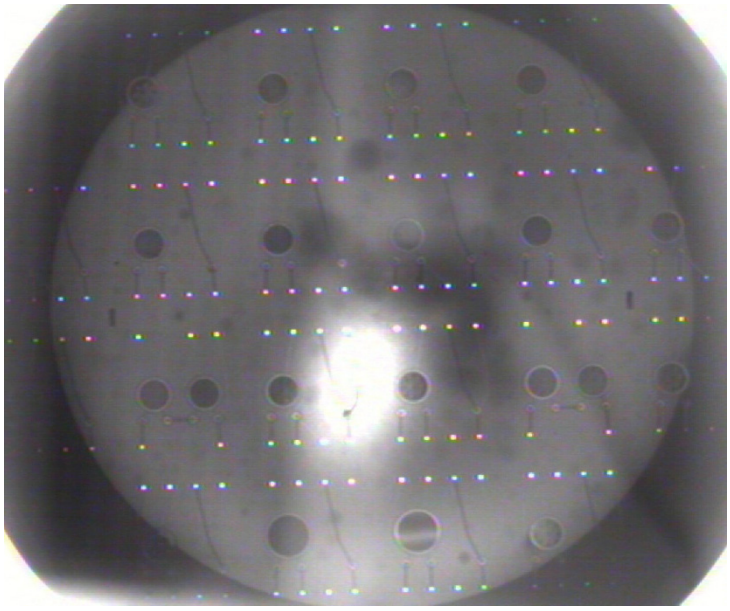

Figure 3-7: Infra-red image of bonded wafers.

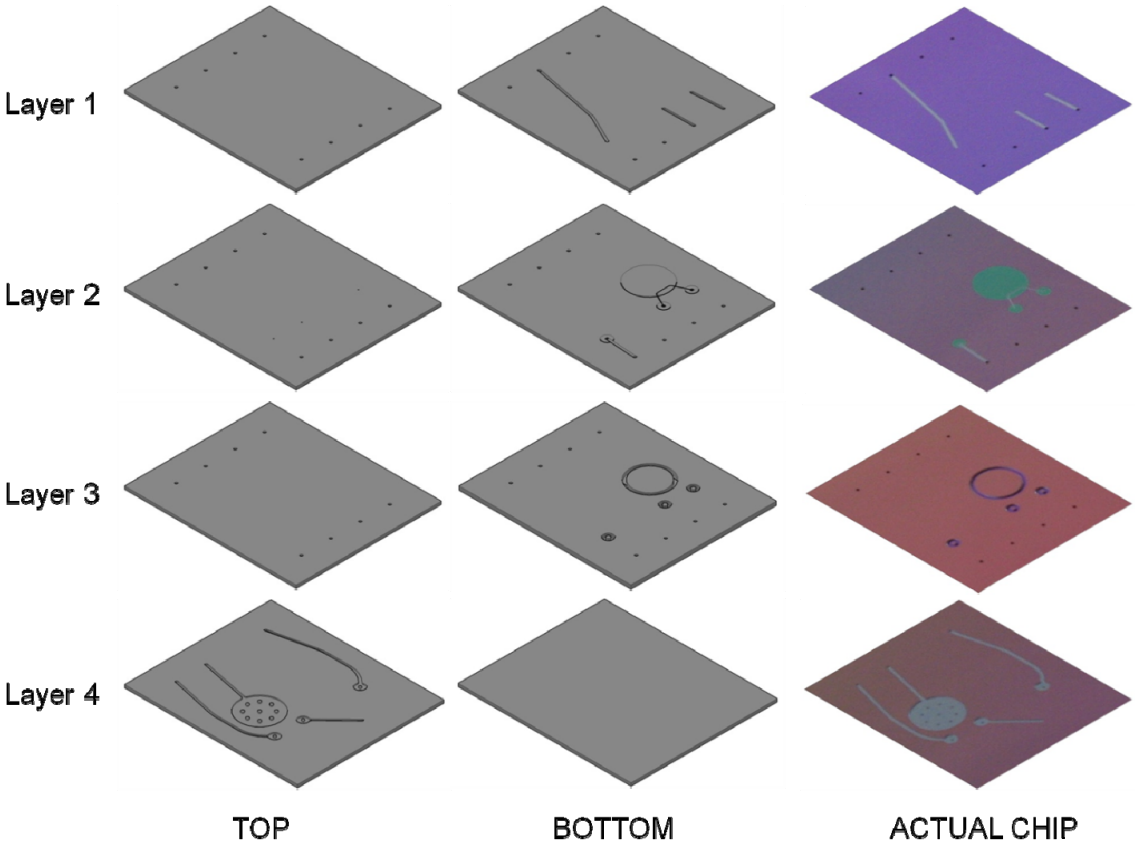

Figure 3-8: Schematic views of each layer, CAD drawings and actual images. Column 1: top views; column 2: bottom views; column 3: actual images.

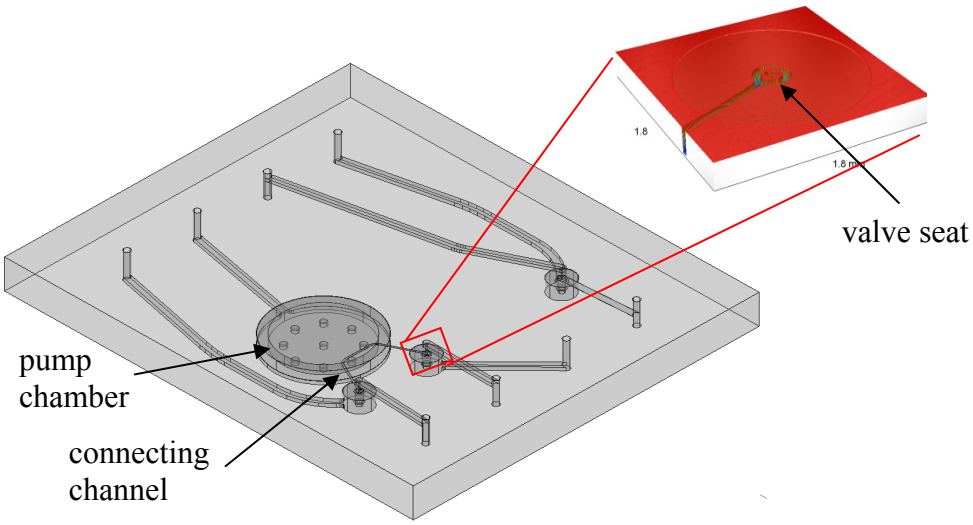

Figure 3-9: 3-D schematic view of a test die, with a measured valve seat structure.

3.3 Variation of Fabrications

There are 20 dies in total on a 6" wafer. Two of them are two-stage pumps, and the remaining 18 dies include a single-stage pump and a single valve each, as shown in Figure 3-9. For the pumps, the valve seats, as illustrated in Figure 3-10, vary in the ring width (r_w) as 40μm, 80μm, or double 40μm rings (40μm × 2). The connecting channel (refer to Figure 3-9) widths are either 50μm or 100μm. Besides, there are two single-stage pumps have chambers with a diameter of 8 mm, while the rest are 6 mm. The distribution of the pump variation is shown in Figure 3-11.

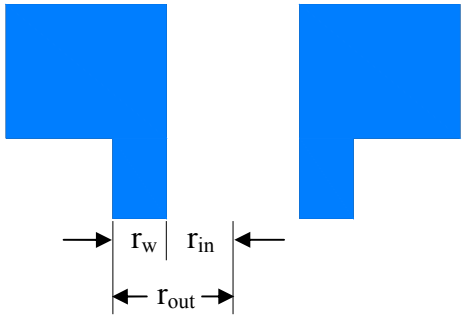

Figure 3-10: Schematic view of the valve seat ring.

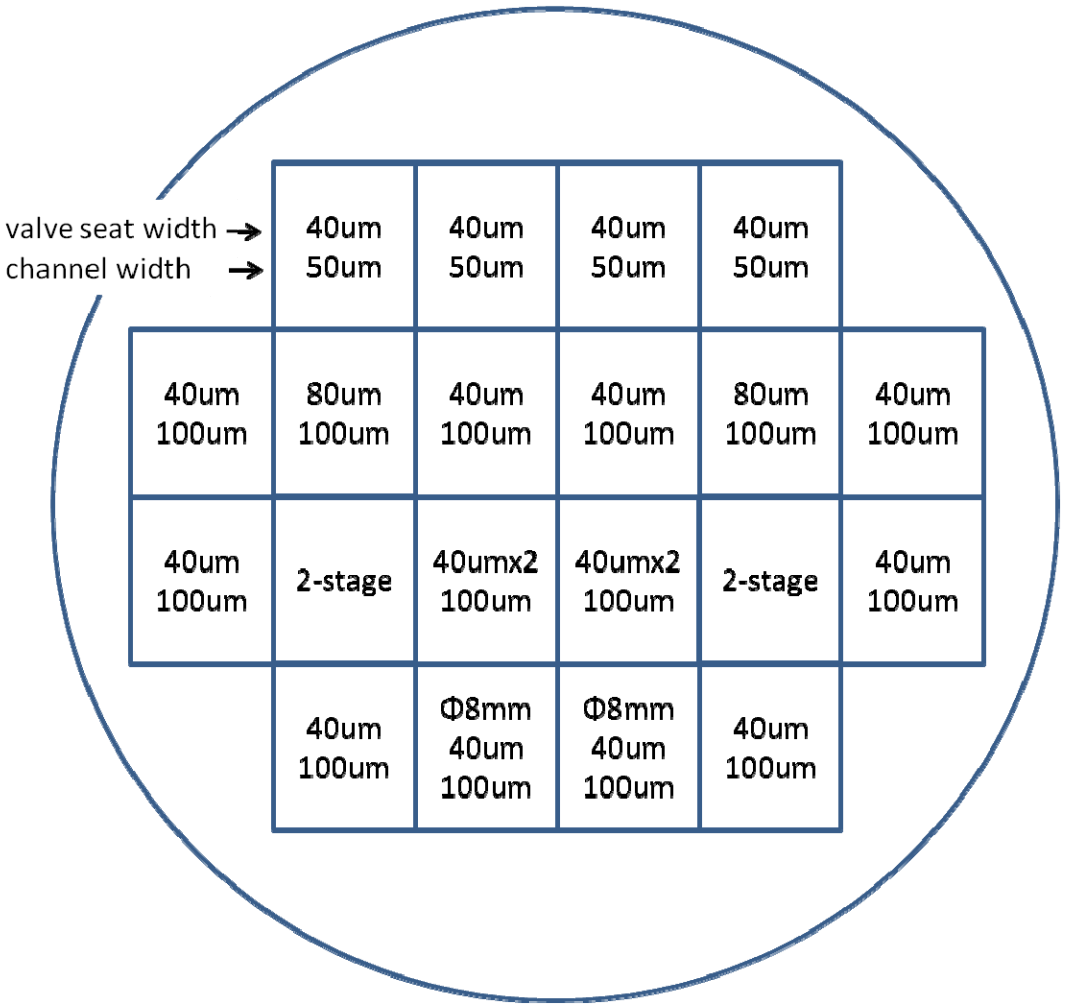

Figure 3-11: Variation of the pumps through the 6" wafer.

The 18 single valves have more variations on the valve seat ring structure. Among all the single valves, there are four types of valve seats as listed in Table 3-1.

Table 3-1: Variation of the single valves (refer to Figure 2-4 for the valve structures)

Valve Types	r_w = 40μm	r_w = 80μm	r_w = 120μm	r_w = 40μm x 2
Quantity	6	4	4	4

3.4 Critical Processes

The four layers are fabricated by deep-reactive ion etching (DRIE) and other standard micromachining techniques. Among all the fabrication processes, there are three processes that are critical in achieving a robust device: 1) DRIE; 2) stress compensation; 3) wafer surface protection and roughing.

3.4.1 Tether Fabrication (DRIE)

DRIE is used to etch through holes, create deep channels, and very importantly, form the deflection membranes. The DRIE process is developed by Bosch, using alternating plasma of SF6 and C4F8 for etching and passivation. A common etch profile is shown in Figure 3-12, if the recipe is not well tuned.

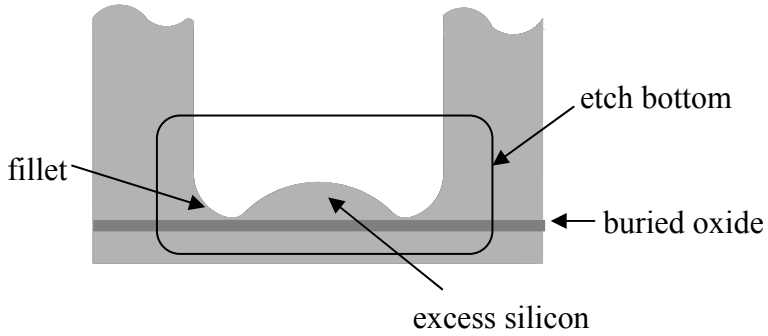

Figure 3-12: An undesired DRIE profile.

1. Excess silicon removal

Excess silicon in the middle of the trench affects the deflection of the tether very much. The spring constant of the membrane is proportional to the third order the membrane thickness. The thickness of the excess silicon can be as large as tens of microns for a 500μm wide trench, and any excess silicon might reduce the practical deflection to one tenth or even only a few percent of its ideal value. For this sake, excess silicon must be removed and the central etch rate should be the same as or higher than that of the edge area.

Middle excess silicon is left mainly because of un-directional ion bombardment during the etch periods. The C4F8 layer is deposited during the passivation period, and ions remove the passivation layer normal to the top surface during the etch period first. Un-directional ions have the edge area exposed and therefore the edge silicon is etched faster,

as shown in Figure 3-13. Two ways can be used to control the excess silicon: 1) increase the etch power, which improve the directionality; 2) elongate the passivation time relative to the etch time for each etch cycle. DRIE recipe is tuned to achieve a smooth etch profile (see Appendix C.3 for the recipe details).

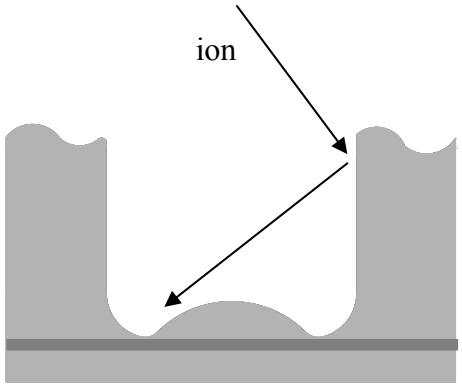

Figure 3-13: Un-directional ion bombardment due to low power.

2. DRIE uniformity

An issue with the DRIE tool we have is the etch uniformity. A preliminary uniformity study is conducted with round holes, as shown in Figure 3-14. Microscopic images of 34 holes on the wafer are captured and are shown side by side to the wafer. The diameters of the holes are 0.4mm. The cross-section of one of the etched holes (A-A') is schematically shown in Figure 3-15. Dark orange areas are the resist, bright areas are the flat silicon surface, and dark areas are due to the optical effect for the large slope of the silicon surface, i.e. the areas between the bottom flat silicon surfaces and the straight side walls. As shown in the figure, the dark regions are not always uniform along the circumference of the holes, i.e. the bright circles are not always concentric with the holes. The drift directions of the etch profile are labeled with arrows.

The central region of the wafer is etched slower than the edge region, but the central region is etched more uniformly. The non-uniformity problem is intrinsic for the DRIE tool. The gas flow is not uniformly distributed inside the etch chamber, and unless the gas shower head is replaced, which is beyond the scope of this research, uniformity remains an issue to us. To minimize the uniformity effects on the tether fabrication, the wafer is rotated by 90^{o} every half hour or every hour (with the available DRIE tool, the total etch time for the tether fabrication is about 4~5 hours).

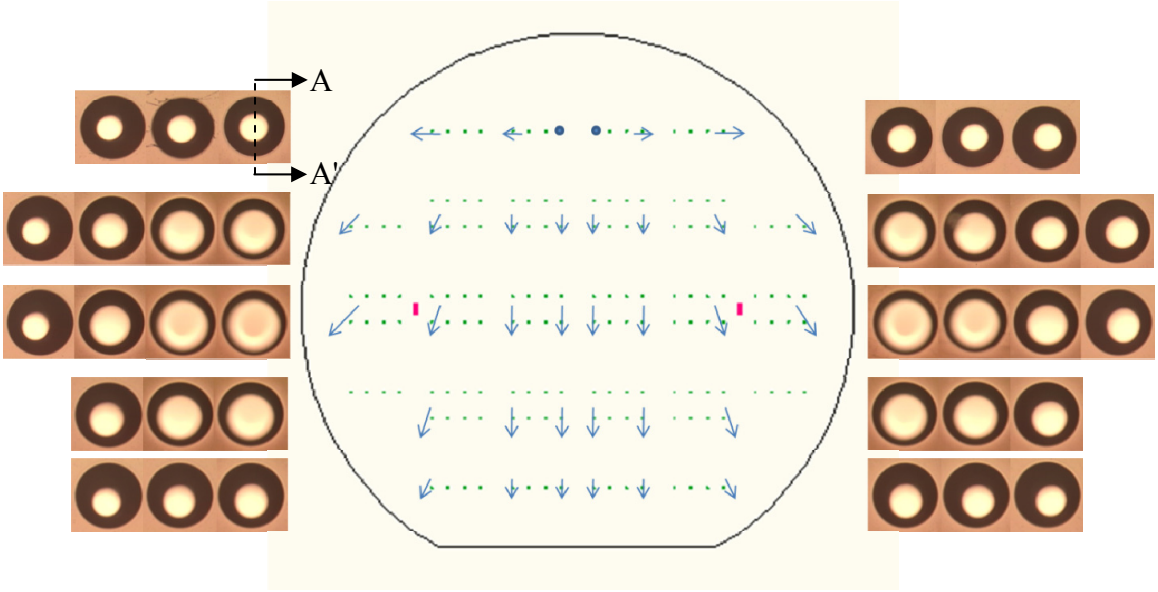

Figure 3-14: Etch uniformity study. The diameters of the holes: 0.4mm.

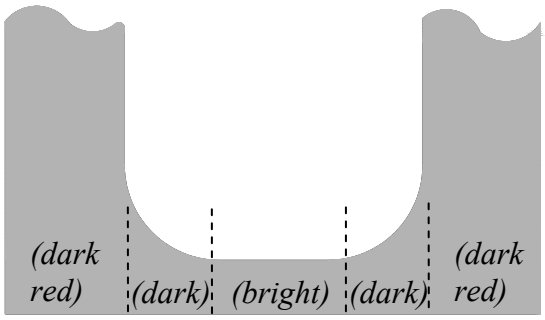

Figure 3-15: Schematic view of the cross-section of the etched hole in Figure 3-14 (A-A').

3. Fillet

To ensure a robust 10μm deflection membrane through a testing with hundreds of thousands of cycles, fillets are critical to be left between the membrane and the bulk silicon. With the fillets, the stress won't concentrate on the tether edges. Therefore the trenches should not be over etched, which will remove the fillet entirely and the tether would not be reliable at all. The trenches should not be under etched either, which will make the tether deflect less than expected, similar with the case of excess silicon. To have the best fillets on all chambers and valves, at the final stage of etch close to the

buried oxide layer, the wafer is taken out of the DRIE etch process every 15 seconds for inspection under the microscope. The finished chambers and valves are covered with Kapton tape, which prevent them from further etching. A typical fillet width is 40~80μm for the best pump performance. An example of the fillet fabrication is shown in [34]. A micromachined displacement pump is diced through the chamber diameter, and the SEM image of the cross-section is shown in Figure 3-16, with the fillet width ~60μm.

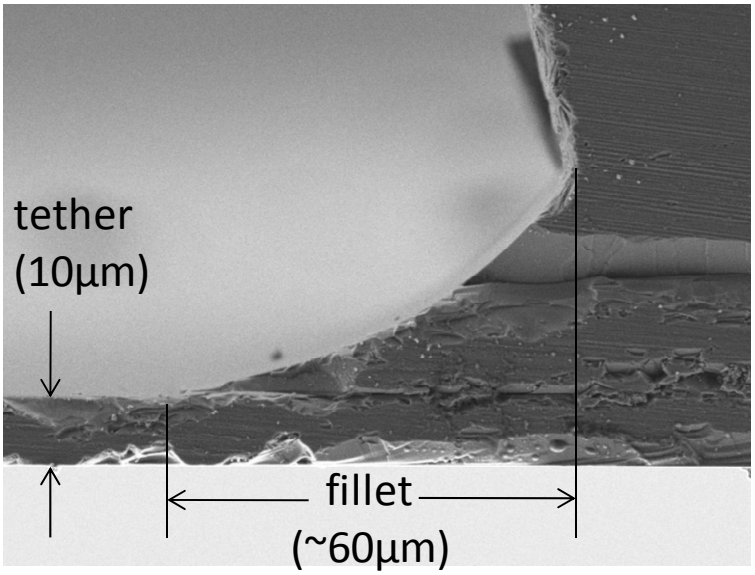

Figure 3-16: SEM image of the fillet.

3.4.2 Stress Compensation

For Layer 3, the buried oxide layer introduces stress on the silicon wafer. A bare 6" SOI wafer with the 0.5μm buried oxide has a bow of ~60μm across the wafer. Because the maximum deflection is designed as 10μm for a Φ6mm chamber, any wafer bow would reduce the total deflection. The stress is compensated with a 0.5μm thick thermal oxide on the handle side, as detailed in Section 3.2 for Layer 3 fabrication.

3.4.3 Surface Protection and Roughing

The four layers are bonded together for assembly. For direct silicon fusion bonding, the surface needs to be smooth. It has been experienced that if a surface is exposed to lithography processes, the surface may or may not be bondable. So we could not take for granted that the surface is bondable without any protection, or not bondable without any intended roughing. For example, for the first trial of fabrication, the valve seats are exposed to all the lithography steps, but during the wafer bonding step, the valve seats on

Layer 2 are bonded to the top surface of Layer 3 permanently and the flow path is blocked. A practical roughing step uses 3 seconds SF6 plasma etch, and the surface roughness is measured with AFM and the results is shown in Figure 3-17. The mean square root of the roughness is 3.88nm, with the maximum peak to depth distance of 43nm. The surface is rough enough to prevent accidental bonding, which is proved with experiment results.

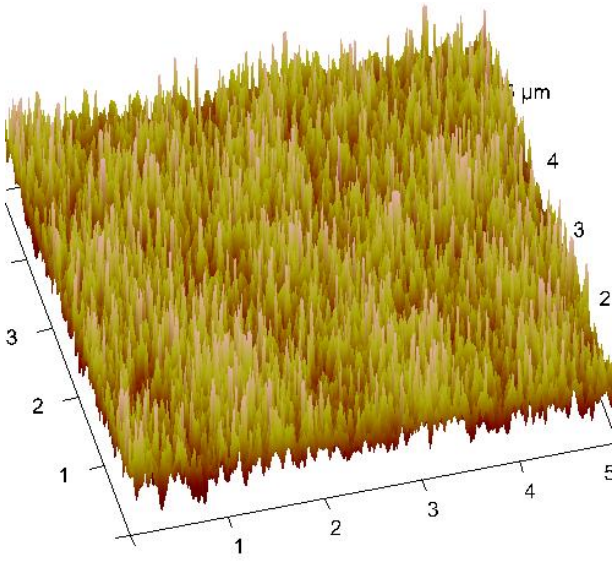

Figure 3-17: Valve seat surface profile measured by AFM.

For the area not to be bonded, the surface is roughened. For the bonding area, the surface is protected with thermal oxide (Layers 1, 2, 4, and top surface of Layer 3) or deposited nitride (bottom surface of Layer 3). This is the very reason why we do the thermal oxidation on all layers, and also nitride deposition on Layer 3, before any other processes. The oxide layers, and the nitride for Layer 3, are removed right before the final RCA clean for fusion bonding.

3.5 Summary

In this chapter, the fabrication processes of the micromachined displacement pumps are illustrated layer by layer. The wafer level assembly is also demonstrated. DRIE and other standard microfabrication techniques are used in the fabrication. Three critical processes are discussed to achieve a robust pump: 1) tether fabrication; 2) stress compensation; and 3) bonding surfaces treatment. Detailed fabrication processes are included in Appendix C. The fabricated test dies are tested and the results are summarized in the following Chapter 4.

Chapter 4
Testing Results and Discussions

The test dies fabricated as described in Chapter 3 are characterized and the experimental results are discussed in this chapter. The testing strategy is firstly described. The testing apparatus is then built and used for the characterization of the micromachined displacement pumps. The experimental results are next summarized, with flow measurement, leakage testing, and also vacuum generation results. The discussions on the experimental results are conducted with lumped element modeling method.

4.1 Testing Strategy

Before we go into the testing setup and characterization results, the testing strategy is first illustrated in this section. Pneumatic actuation is chosen for characterization purpose, and the testing plan is described afterward.

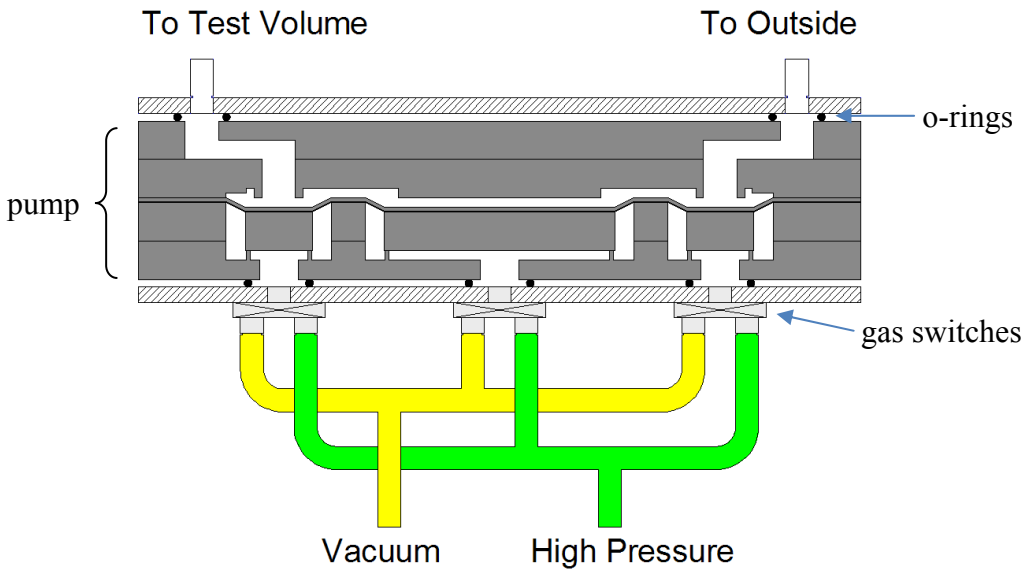

Figure 4-1: Schematic view of the pneumatic actuation testing.

A high pressure source is used for pushing-up actuations, i.e. the chamber compression and the valve sealing actuations. House compressed nitrogen is chosen as the high

pressure source, with an actuation pressure of ~2 atmospheric pressures. A low pressure source is used for pulling-down actuations to open the pump chamber or the valves. An external vacuum pump is adopted as the low pressure source, with an ultimate pumping capability of 0.5mtorr and a practical actuation pressure of ~100 torr within the short actuation transition times. A schematic view of the pneumatic actuation testing is shown in Figure 4-1. Note that the actuation ports on the test dies are moved to the bottom surface in the figure for demonstration purpose. The actual geometry is drawn in Figure 3-9, and a schematic cross-section closer to the actual pumps is shown in Figure 3-1.

The testing with pneumatic actuations will follow three steps: the prescreening testing (flow measurement), the valve leakage testing, and the vacuum generation measurements. The single-stage pumps and the single valves from the build of "HZ2", with the wafer map shown later in Figure 4-11 of this chapter, are used for pump and valve characterization. A single pump from Vikas Sharma ("VS2-1") is also used for the preliminary vacuum generation testing.

4.1.1 Prescreening testing: flow measurement

Before the vacuum generation test, the pumps are subject to a prescreening step with flow measurement. The two ends of a displacement pump are connected to a high pressure source and a low pressure source, respectively, with a flow sensor in the middle of the flow path, as shown in Figure 4-2.

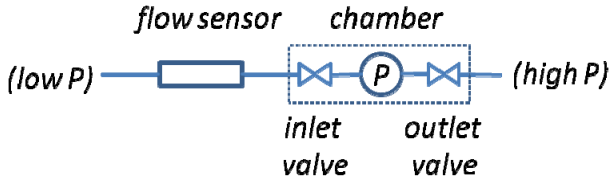

Figure 4-2: Schematic drawing of flow measurement.

Three flow sensors, Honeywell (0719-AWM3150V), Sierra (M101-DD-1-OV1-PV2-V1-V3), and MKS Japan (M200M-O2C4VA) are considered and Honeywell flow sensor is chosen for its simplicity in gas tube connection and electrical output interface. A calibration is conducted before any actual flow testing.

The prescreening step is important in practice. The first build of fabrication did fail because of unexpected bonding at the valve areas (The details for such accidental bonding are discussed in Section 3.4.3), and the prescreening testing has saved our time and effort on the failed test dies. The low pressure end is open to the ambient (~760 torr),

and the high pressure end connects to a tunable pressure source between 2 atm to 1 atm. The valves and the chamber are vacuum actuated, and if the flow path is open the magnitude of the flow rate is on the order of 0.1 ~ 1 sccm; if the flow path is blocked there would be no detectable flow. An example of the flow measurement of a failed pump is shown in Figure 4-3. No matter how the positive pressure changes, there is no flow measured by the flow meter and thus there is no voltage output from the meter. The flow testing of a working pump and a valve is discussed in more detail in Section 4.3.1.

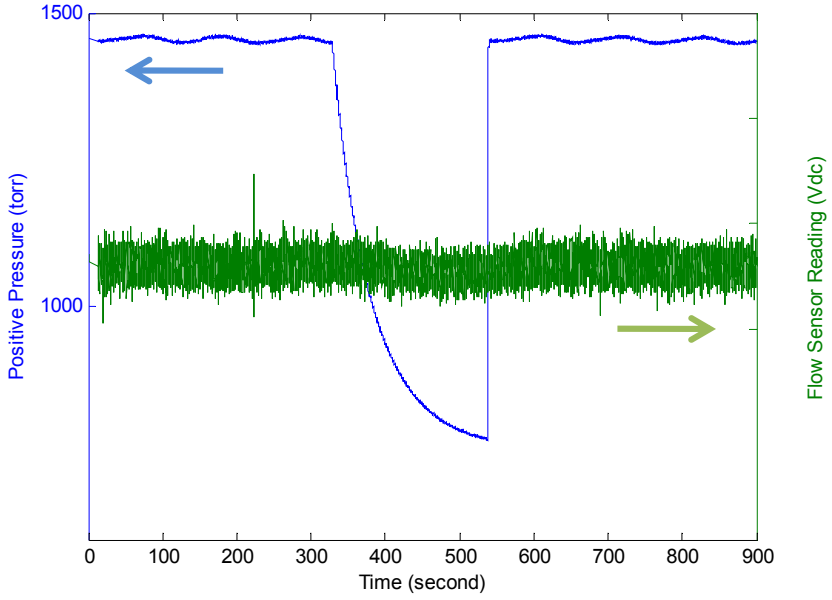

Figure 4-3: Flow rate measurement of a failed test die.

4.1.2 Leakage Testing

The leakage of the displacement pumps and the single valves are also tested. The leakage value is essential to understand the performance of the single-stage pump. The leakage is tested in two ways, full-scale testing and near-zero-point testing.

Full-scale testing is conducted with three steps: 1) open the flow path with vacuum actuations and evacuate the test volume by connecting the outlet to external vacuum source; 2) wait until the test volume pressure is reduced to below 200 torr and close one or two valves; and 3) restore the outlet pressure to atmospheric pressure by disconnecting the vacuum source and measure the pressure change inside the test volume. The pressure change curve is mathematically fitted to extract a leakage time constant, which has been derived in Section 2.3. An example of the full-scale testing has been shown in Section 2.3.2.3 Figure 2-19.

However, the full-scale testing not only measures the intrinsic pump valve leakage, but also parasitic leakage from the testing setup. The parasitic leak might be comparable or even larger than the pump valve leak, and therefore another testing is also conducted to estimate the actual pump valve leakage, which we call “near-zero-point testing”. The "zero-point" means zero pressure difference between the test volume pressure and the ambient pressure.

Near-zero-point testing is similar to the full-scale testing in operations, except the pressure change is measured around atmospheric pressure, i.e. the differential pressure between the test volume and the ambient pressure is close to zero. The slope of the pressure change around atmospheric pressure, 760 torr, is used to characterize the valve leakage. The full-scale and near-zero-point leakage testing results are shown in Section 4.3.2.

An indirect way to measure the leakage is to use the vacuum generation results. The leakage is proportional to operation times, and the leakage can be derived by tuning a certain operation time. A systematic approach is described in Section 4.4 with the complete understanding of the displacement pumps' vacuum generation performance.

4.1.3 Vacuum Generation

The vacuum generation performance of the single-stage pump is characterized with a 6-step operation cycle, which has been shown in Figure 1-9. Another way to describe the 6-step operation sequence is to label the actuation pressures for inlet and outlet valves and the pump chamber, as shown in Figure 4-4. The first three steps are for gas charging into the pump chamber from the test volume: I) pre-charging; II) charging; and III) post-charging. The last three steps are for gas discharging from the pump chamber out to the ambient: IV) pre-discharging; V) discharging; and VI) post-discharging. To achieve the best vacuum generation performance, the operation times are tuned and the testing results are discussed in Section 4.3.3.

4.2 Testing Setup

4.2.1 Test Setup Overview

The test setup includes three parts: 1) test jig; 2) actuation apparatus; and 3) data acquisition system. The test jig holds the test die, and the actuation apparatus conducts

the vacuum generation actuation. The pressure changes inside the test volume and the actuation ports are captured with the data acquisition system.

The test die is 22mm wide, 26mm long, and 2mm thick, which is shown again in Figure 4-5. All the actuation ports and inlet/outlet ports are facing up. The test die is flipped upside down onto the test jig with o-rings in between for sealing. The test jig lid is then clamped on top.

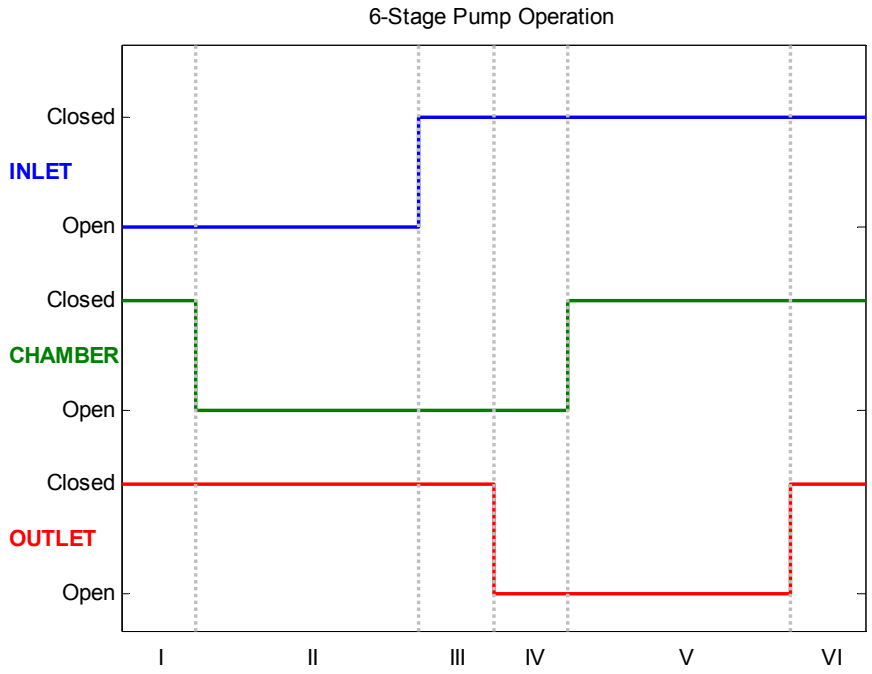

Figure 4-4: The 6-step operation cycle for the valves and the pump chamber: "open" -- vacuum actuations; "closed" -- high pressure actuations.

Test Jig: the eight ports of the test die connect to the eight channels on the test jig, which further connect to outer components through Swagelok connectors, as shown in Figure 4-6. For each channel, a pressure sensor (Omega PX209-030A5V) is attached to monitor the pressure changes. In addition, for each actuation port, a gas switch, Parker Kuroda VA01PEP34-1U, is attached to switch between high pressure and vacuum actuations.

Actuation apparatus: the house compressed nitrogen, the high pressure source, and an external vacuum, the low pressure source, are connected to the gas switches with plastic tubes. The high pressure source is controlled to be around 2 atm absolute pressure, and is monitored with another pressure sensor (Parker Convum MPS-L3N-PGA) with a LED

indicator. The gas switches are controlled by a microcontroller through OMRON relays. Details of the testing jig and hardware components are discussed in Appendix D.

Data acquisition: the eight Omega pressure sensors output voltages between 0 and 5 volts. A National Instruments (NI) DAQ card is used to convert the voltages into digital signals, which are recorded with NI Labview program. The voltage data are then converted into the pressure values.

A summary of all the components is included in Appendix D.3.

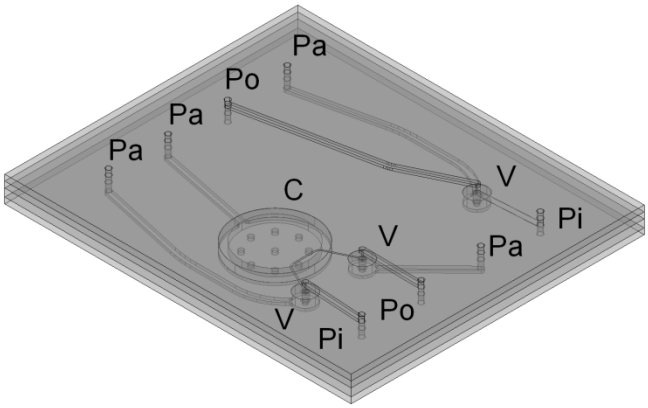

Figure 4-5: Perspective CAD drawing of the test chip.
Labels: C - chamber, V - valve, Pi - inlet port, Po - outlet port, Pa - actuation port.

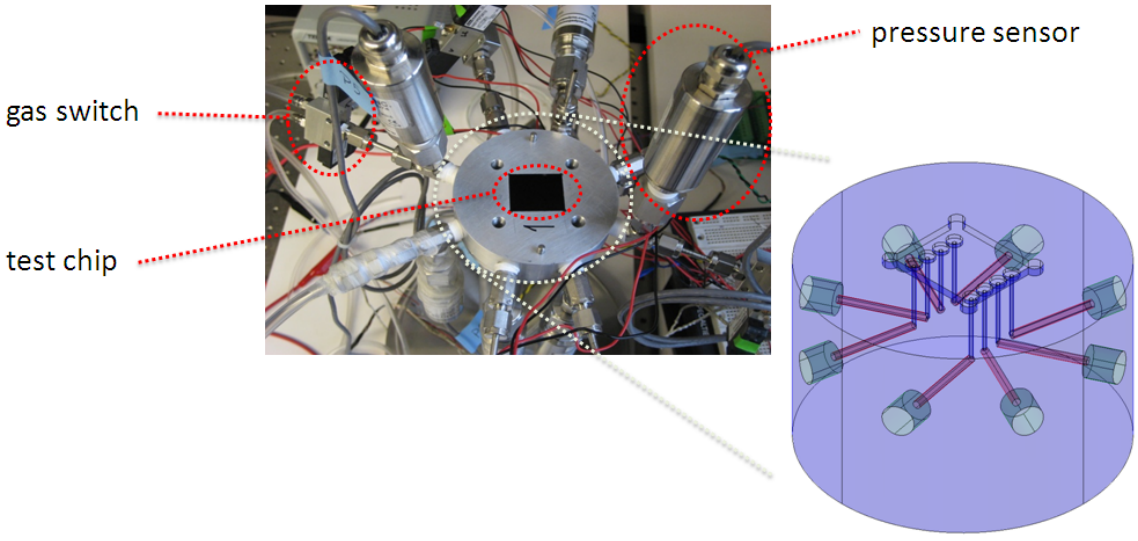

Figure 4-6: Test setup overview.

4.2.2 Test Setup Calibration

The eight ports on the test jig side are connected to outside through tee or straight Swagelok connectors, and pressure sensors are connected to the Swagelok connectors with NPT connectors. To ensure the connections seal well, the test setup is calibrated while we assemble all the components.

An o-ring is placed to isolate the eight ports on the test jig, as shown in Figure 4-7 (a). The connection of a pressure sensor to the test jig is shown in Figure 4-7 (b). The test jig lid is clamped and a calibration pressure sensor is connected to one of the eight ports, as shown in Figure 4-7 (c). Another port connects to a vacuum source, and all the components on other ports are assembled. The calibration sensor has a pressure indicator as shown in Figure 4-7 (d). If any of the ports has significant leak, the reading of the calibration sensor is high. If all the components are tuned well, a good vacuum reading will maintain. All the eight ports are fine tuned and the test setup is ready for characterizing the displacement pumps and the valves.

4.3 Testing Results

4.3.1 Flow Testing

A prescreening flow test is important to check whether the flow path is open or not before extensive vacuum generation testing. A plastic tube is used to calibrate the flow measurements first. Then the flow measurements are done on the single-stage pumps and the single valves.

1. Calibration of Flow Testing

As shown in Figure 4-3, the tolerance of the flow meter is in a range and for the particular meter we use, the output needs to be calibrated. A microfluidic tube is prepared to calibrate the flow measurement. The inner diameter of the tube is measured with optical microscope as 0.2mm, and the length is 1.27m. By assuming Poiseuille flow, the fluidic resistance of the tube is calculated as

$$R_{tube} = \frac{8\eta L}{\pi r^4} = 6.4 \times 10^{11} Pa \cdot s \cdot m^{-3}$$

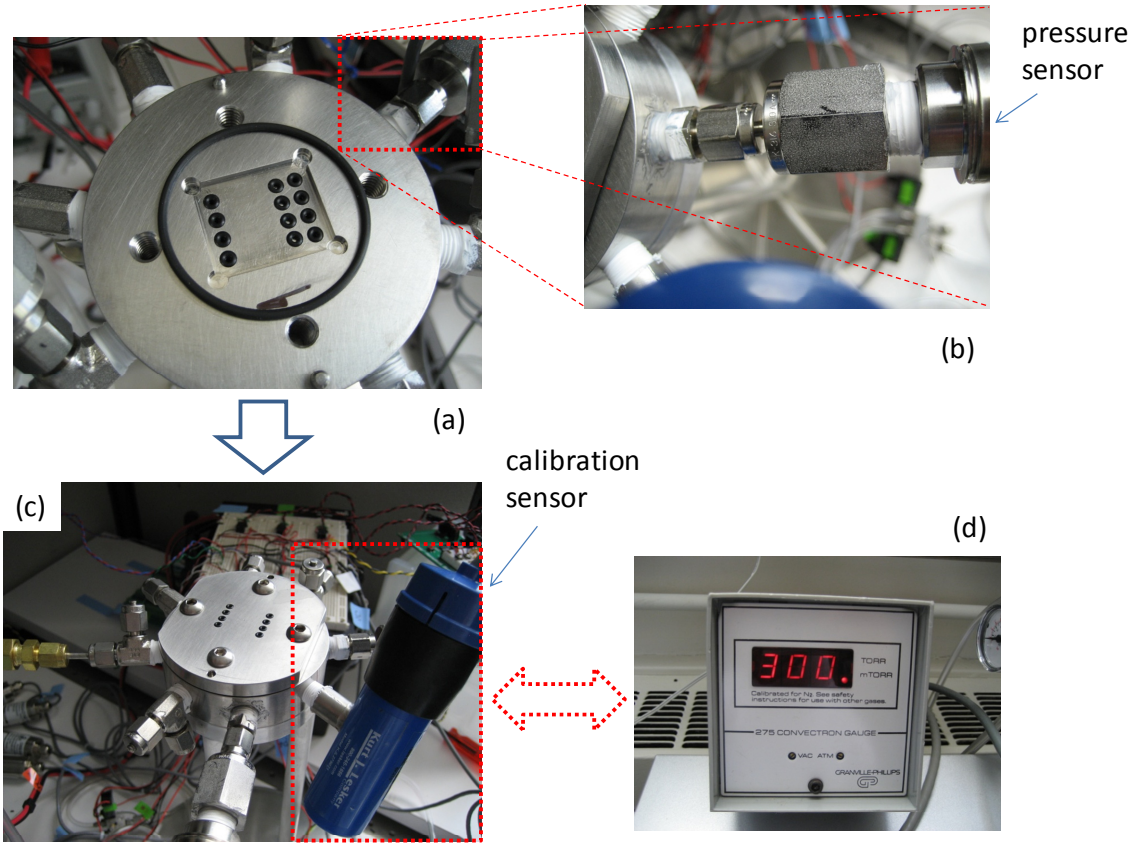

Figure 4-7: Test setup calibration. (a) O-ring is used to isolate the eight ports; (b) connection of a pressure sensor; (c) the lid is clamped and the calibration sensor is attached; (d) the indicator of the calibration sensor.

The flow meter baseline, i.e. the voltage output without any flow, has been measured with a mean value of 1.0515 volt. With a pressure difference between the two ends (refer to Figure 4-2) of 690 torr, the voltage output has a mean value of 3.65 volt. With the resistance calculated in Eq. 4-1, the flow rate is then 16.4 sccm. The corresponding flow meter voltage output slope is then

$$Slope\ (flow\ meter\ output) = \frac{voltage\ output}{flow\ rate}$$

$$= \frac{(3.65 - 1.05)\ volt}{16.4\ sccm} = 0.16\ volt/sccm$$

The flow rate measured from the flow meter is then calculated based on Eq. 4-1.

$$flow\ rate\ (sccm) = \frac{voltage\ output - 1.0515\ (volt)}{0.16\ \left(\frac{volt}{sccm}\right)} \quad (Eq.\ 4-1)$$

2. Flow Testing of the Single-Stage Pumps

A pump is connected to the flow meter with pressure differential applied on both ends, as shown in Figure 4-2. The flow is measured with either valve closed, pump chamber closed, or both valves and the chamber closed.

The high pressure source is measured to be ~1405 torr, and the low pressure source is the ambient pressure ~760 torr. From the calculation in Section 2.3, the resistance of the pump is 2.07×10^{13} Pa·s·m^{-3} when both valves and the pump chamber are open, or 4.14×10^{13} Pa·s·m^{-3} when both valves are open but the pump chamber is closed. The corresponding flow rates are 0.46 sccm and 0.23 sccm as calculated, respectively.

A typical flow testing curve is shown in Figure 4-8 for a working pump (HZ2-A3). When either valve is closed, the flow rate is close to zero. When both valves and the pump chamber are vacuum actuated open, the flow rate is 0.46±0.03 sccm. When both valves are open and the pump chamber is closed, the flow rate is 0.25±0.03 sccm, as shown in Table 4-1. The errors are estimated based on the biggest and smallest values of the flow rates. The experimental results, which are based on the flow meter calibration in the previous part, agree with the calculation. On the other hand, if the flow path is blocked and the pump will not work, the flow rate would be around zero at all times.

Table 4-1: Flow rate for the pump HZ2-A3 with a pressure drop of 645 torr.

Chamber State	Lumped Element Modeling	Experimental Results
Open	0.46 sccm	0.46 ± 0.03 sccm
Closed	0.23 sccm	0.25 ± 0.03 sccm

Note: both valves are open while measuring the flow rate.

The flow testing is very useful to prescreen the test dies before extensive vacuum generation testing. As shown in the following section: vacuum generation results, a

typical vacuum generation testing lasts over three hours, and the prescreening step helps to save time in pump characterizations.

A test die also includes a single valve beside the single-stage pump. The single valve is also going to be tested for valve leakage, and the valve is subject to flow testing as well. Similar to the flow testing of a single-stage pump, when the valve is open, a flow is detected; when the valve is closed, the flow is not detectable. A typical flow testing result for a good valve on the die HZ2-B2 is shown in Figure 4-9. The measured flow rate in Figure 4-9 is 1.25±0.10 sccm, and the calculated flow rate of an ideal valve is 1.18 sccm, which agrees to the experimental results.

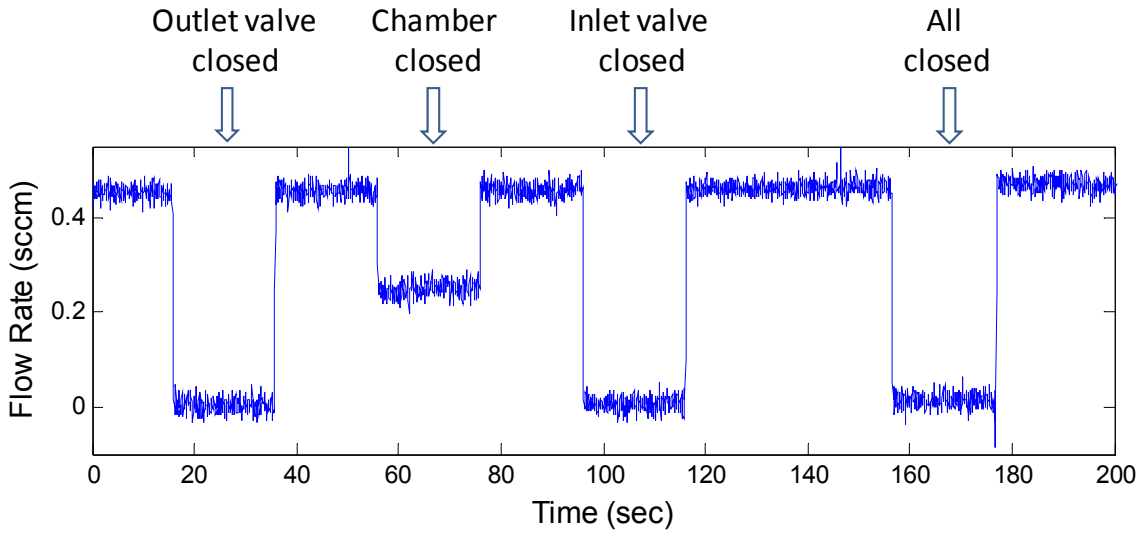

Figure 4-8: A flow testing result for the single-stage pump HZ2-A3.

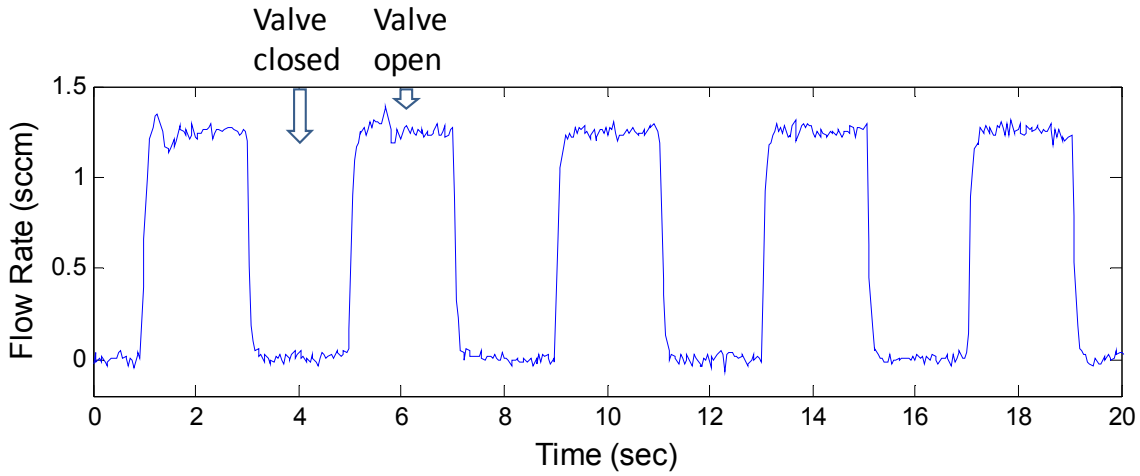

Figure 4-9: A flow testing result for a working valve on the die HZ2-B2.

4.3.2 Leakage Testing

The pump leak is another major limiter beside the dead volume on the vacuum generation performance of micromachined displacement pumps. For a complete analysis of the experimental results and a better understanding of the vacuum performance, the pump leakage is essential to characterize. The pump leakage is measured directly and can also be derived indirectly.

1. Pump leakage measurement: full-scale testing

The pump leakage is measured directly with pressure changes inside the test volume. Full-scale testing and near-zero-point testing are done, as described in Section 4.1.2. Full-scale testing has three steps:

Step 1: test volume pressure is reduced with external vacuum source;
Step 2: a valve is closed when the test volume pressure is below 200 torr;
Step 3: the outlet pressure is restored to atmospheric pressure and the test volume pressure is measured and analyzed.

The pressure in Step 3 is recorded, as shown in Figure 2-19. The pressure curve is mathematically fitted to extract a leakage time constant, which is defined in Section 2.3 Eq. 2-15. Two of the 18 single-stage pumps in the current build fail the valve leakage testing: one has a blocked flow path which could be caused by contamination and one has a valve that could not be closed normally possibly due to the defect of the valve. The remaining sixteen single-stage pumps are tested. The time constants are extracted and shown in Figure 4-10. The corresponding pump feature sizes may refer to Chapter 2 & 3. The gas leakage resistance can be calculated based on the leakage time constants with Eq. 2-15b: $\tau_{leak} = V_t \cdot R/P_0$, and the leakage rate is then derived with Eq. 2-1: $R = \Delta P/Q$. For example, the leakage rate for the pump HZ2-B4 (refer to Figure 4-11 for the chip location) is derived as 0.70 sccm.

The leakage time constants are also visualized in Figure 4-11 and the results are sorted by the seal ring width in Figure 4-12.

2. Pump leakage measurement: near-zero-point testing

The leakage measured with the full-scale testing method includes not only the intrinsic pump valve leak but also the parasitic leak of the testing setup. The leakage is proportional to the pressure differential between the test volume and the ambient, and to measure the pump valve leak more accurately, a near-zero-point testing is done. The test

volume pressure is around the ambient pressure, ~760 torr, and the pump outlet is connected to a high pressure source or a vacuum source when the valve is closed. The slope of the pressure change around the ambient pressure is measured.

	2.44	3.01	2.96	5.96	
1.15	6.86	2.88	4.75	4.82	2.82
(Fail)	(Two-Stage)	(Fail)	3.09	(Two-Stage)	4.63
	2.84	2.43	2.62	4.11	

(× 10^4 seconds)

Figure 4-10: Wafer map of pump leakage time constants (build HZ2).

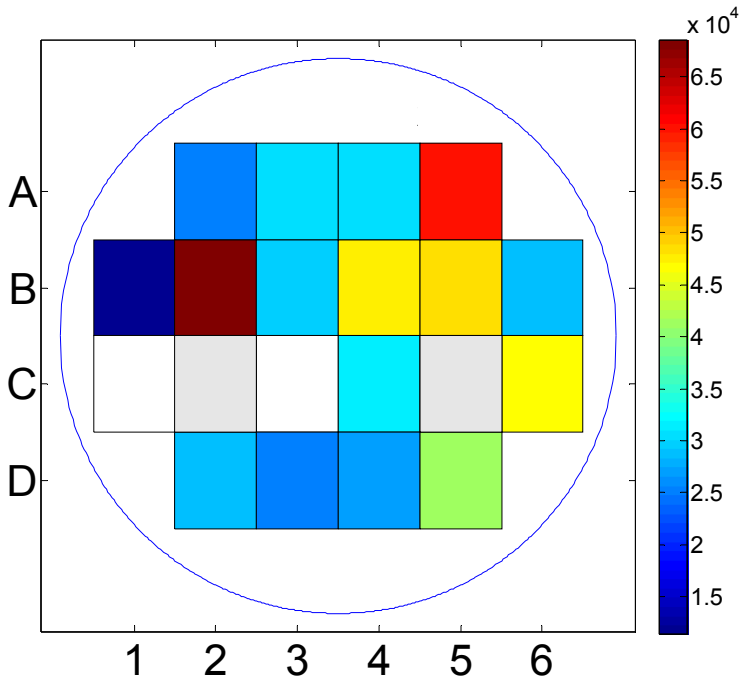

Figure 4-11: Pump leakage time constants (build HZ2), visualized in color.

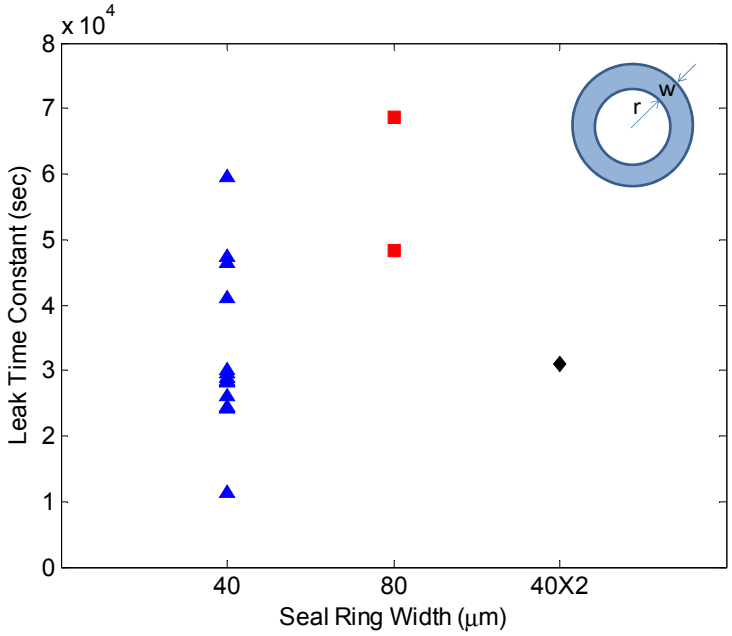

Figure 4-12: Pump leakage time constants (build HZ2), sorted by the seal ring width ("w" in the inset image). Please refer to the wafer map in Figure 3-11 for location of each seal ring width.

The testing results of the pump HZ2-B4 (refer to Figure 4-11 for the chip location) are shown in Figure 4-13 with the outlet pressure of 2 atmospheric pressures. The slopes are (a) 6.62×10^{-3} torr/sec when the outlet is connected to a high pressure source, and (b) -5.51×10^{-3} torr/sec when the outlet is connected to a vacuum source. The test volume is ~0.6 cm^3, and thus the valve leak rate is 0.31×10^{-3} sccm or 0.26×10^{-3} sccm, respectively, with a mean value of 0.29×10^{-3} sccm. This number is only 41% of what has been derived in full-scale testing, which shows that the parasitic leak contributes to more than half of the system leak. The discussion of the parasitic leak continues in Chapter 5.

3. Pump leakage measurement: in-direct method

The pump leakage can also be estimated with the vacuum generation testing results. For example, as we will see later in Table 4-5 of this chapter, when the charging time changes from 320 ms to 640 ms, the base pressure increases from 165 torr to 207 torr. In other words, the 320 ms longer operation time leads to a 42 torr base pressure increase. If we can assume that the pumping efficiency between the two operations are the same or very close, the effect of the leakage on the base pressure will be 42 torr/0.32 sec = 131.25

torr/sec. From the fundamental equation of the pump vacuum generation performance, the leakage is calculated with

$$Q_{leak} = \frac{V_d + V_p}{P_0} \cdot \frac{\Delta P_v}{\Delta T} \quad (Eq. 4-2)$$

If at the quasi-static state, the pumping volume, i.e. the pump chamber volume, stays fully open with a volume of 0.238 mm^3, the leak rate will be 2.47×10^{-3} sccm. A more accurate estimation is done with the full system gas dynamic modeling in Section 4.4 with mathematical fitting of experimental results.

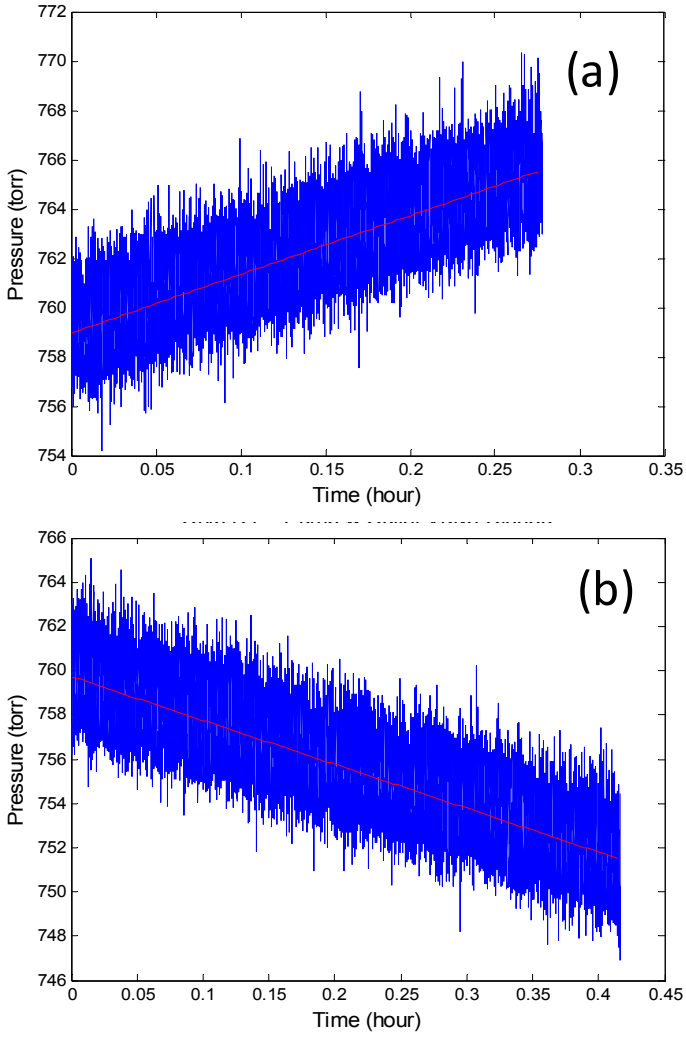

Figure 4-13: Pump valve leakage measurement (HZ2-B4), near-zero-point testing (ΔP = 1 atm). The pump outlet is connected to (a) a high pressure source; or (b) a low pressure source.

4. Single valve leakage measurement

There are four types of single valves, as shown in Table 3-1. The valve seal ring width varies from 40μm, 80μm, 120μm, to double 40μm rings with a 40μm gap. The valve leakage time constants, which are derived similar to those for pump leakage time constants in part 1 of this section, are listed in Figure 4-14. The data are also visualized in color, as shown in Figure 4-15, and sorted by valve type, as shown in Figure 4-16.

Sharma found that the sealing performance (closed valve resistance) of his pumps followed the relationship of Eq. 2-9 [26], but the leakage time constants of our pump valves or single valves do not show a clear trend with the valve types. The reason behind this phenomenon is that the valve leakage in our new design has been reduced greatly and parasitic leak of the test jig is no longer negligible. The lowest leak rate in Sharma's pump is found, if there is 1 torr pressure drop across the valve, to be 4.1×10^{-5} sccm, while in our pump with the new design, the corresponding intrinsic valve leak rate under 1 torr pressure drop, for example Chip B4 discussed previous in this section, is only 3.7×10^{-7} sccm, which is two orders of magnitude smaller. The parasitic leakage contributes more than half of the total leakage, and thus the total leakage time constants would not follow Eq. 2-9 due to the dominant parasitic leakage.

	1.16	1.19	1.32	(Fail)	
1.48	(Fail)	1.40	1.48	1.86	(Fail)
1.27	(Two-Stage)	1.43	(Fail)	(Two-Stage)	0.63
	1.34	1.52	0.62	1.67	

(× 10^4 seconds)

Figure 4-14: Wafer map of single valve leakage time constants (build HZ2).

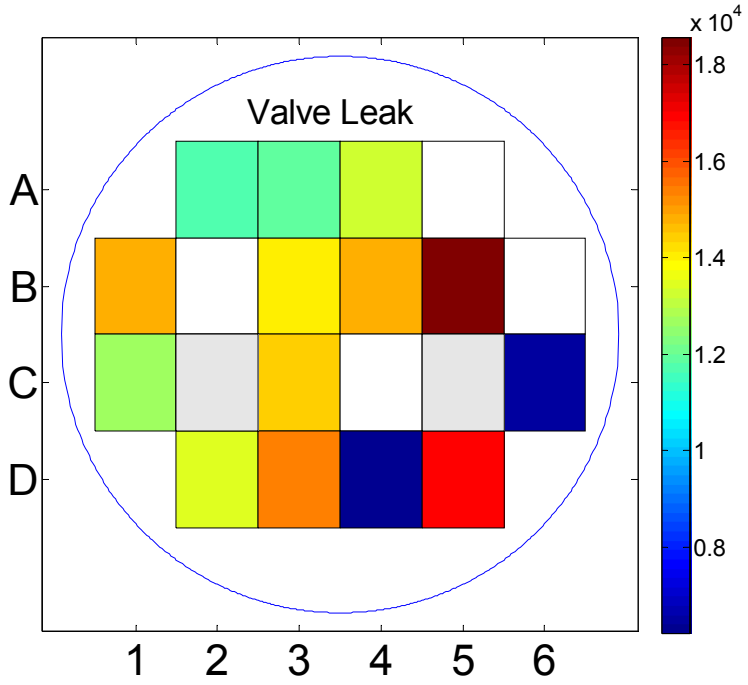

Figure 4-15: Single valve leakage time constants (HZ2-B4), visualized in color.

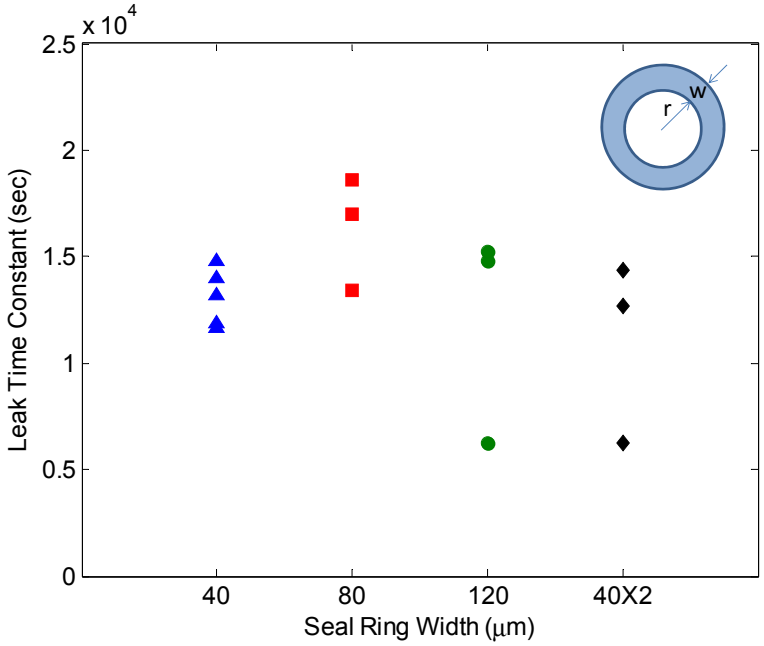

Figure 4-16: Single valve leakage time constants (build HZ2), sorted by the seal ring type ("w" in the inset image).

4.3.3 Vacuum Generation Results

The vacuum generation performances of the pumps are measured. The testing sequence is shown in Figure 1-9 and Figure 4-4, with three steps for gas charging from the test volume into the opened pump chamber, and the other three steps for gas discharging to outside by closing the pump chamber with high pressure actuation.

Before the characterization of the current design, the previous pump, as introduced in Section 1.5 and revisited in Chapter 2, is tested first and the vacuum generation performance of micromachined displacement pumps are studied preliminarily. The pumps from current design are measured by sweeping the operational parameters. Parametric testing is also done.

1. Preliminary vacuum generation results

As an initial exploration of the effect of charging/discharging times, a pump from the previous design, VS2-1, is tested, and the results are listed in Table 4-2. The importance of the preliminary testing results is not just further lowering the base pressure by another 8 torr, 494 torr from 502 torr as reported in [26], but also demonstrating the influence of the charging time and discharging time on the displacement pump's vacuum generation performance.

A two-step experiment is designed to show the effect of gas discharging time on pump vacuum generation performance. With the valve operation times of 100ms and gas charging time of 300ms, run the 6-step operation with the gas discharging time of 300ms. When the pressure of the test volume is stabilized, change the gas discharging time to 600ms, and the base pressure changes from 530 torr to 494 torr, as shown in Figure 4-17.

Table 4-2: Preliminary vacuum generation results of the pump VS2-1.

T_{valve}* (ms)	$T_{charging}$** (ms)	$T_{discharging}$** (ms)	Base Pressure (torr)
100	300	300	530
100	300	600	519
100	600	300	547
100	600	600	494

* T_{valve}: valve operation times
** $T_{charging}$, $T_{discharging}$: gas charging and discharging times

2. Initial round testing

The testing of the new micromachined displacement pump design for vacuum generation is conducted with the 6-step operation as shown in Figure 1-9 and Figure 4-4. An actual actuation profile is shown in Figure 4-18. When the actuation is switched between high pressure and low pressure, there are delays on the order of tens of milliseconds. From the realtime actuation profile as shown in Figure 4-18 (a), we can see the actuation pressure can be either elevated or reduced to atmospheric pressure in 10~20ms.

As shown in Section 4.3.2, there is a wide range of the leakage time constants for different pumps, and the vacuum generation testing will be conducted with the same chip for the initial and the second rounds testing (HZ2-B5, refer to Figure 4-11 or 4-15 for the chip location). Another chip (HZ2-A5) is chosen for the third round testing and parametric testing (Run 1~3) because of its better vacuum generation performance.

As derived in Chapter 2, the gas capacitance is proportional to the volume. The modified design in this thesis work has a pump chamber which was 10% of the previous pump chamber in volume, and the starting operational parameters are then set about 1/10 that of the preliminary vacuum testing. The initial round testing has gas discharging times from 30ms to 80ms, and the gas charging times range from 20ms to 80ms. Valve operation times are set as 10ms, and combined with gas charging and discharging times, the pumping operation is accomplished.

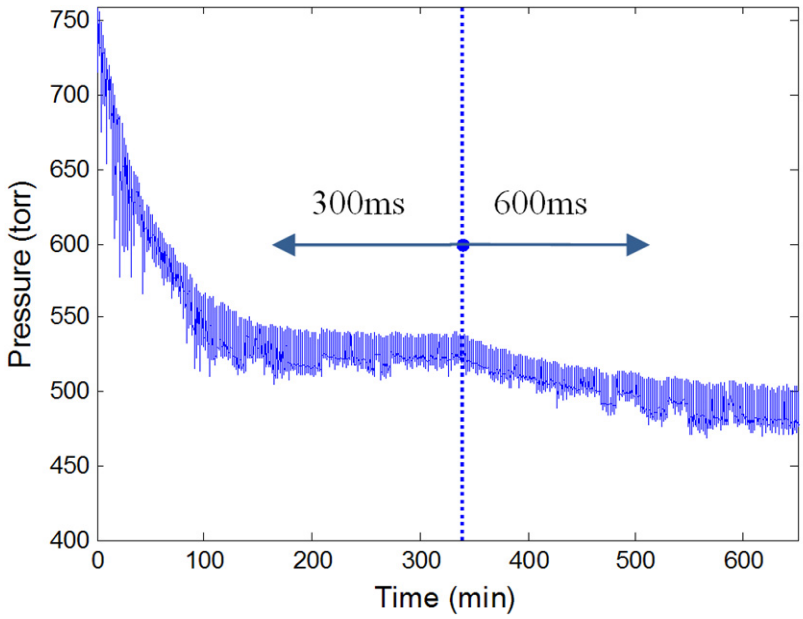

Figure 4-17: Vacuum generation by tuning discharging time, with a pump from Vikas Sharma (VS2-1).

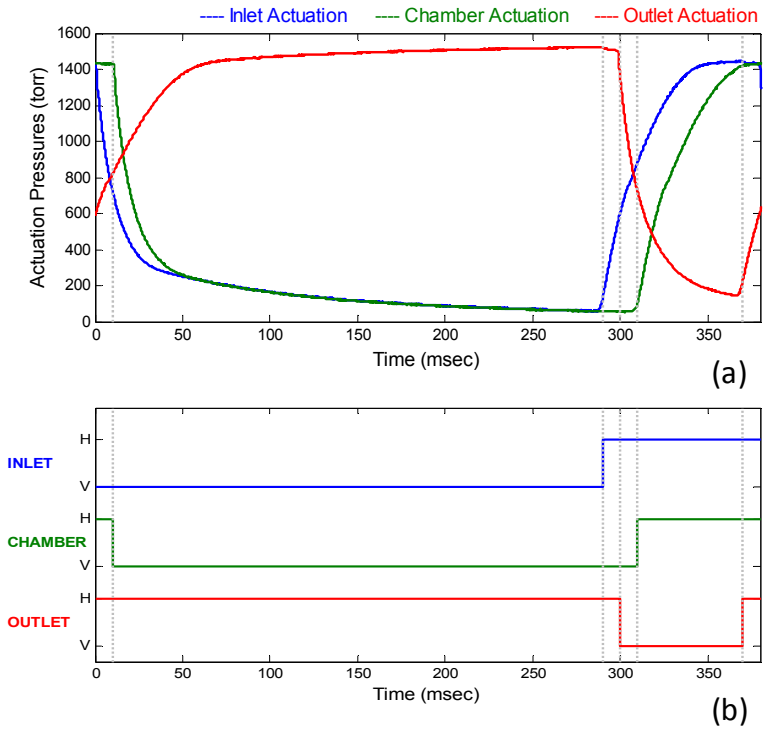

Figure 4-18: Actuation profile for one 6-step operation cycle.
(a) realtime actuation profile; (b) ideal actuation profile.

Table 4-3: The initial round vacuum generation results of the pump HZ2-B5.

T_{disc} \ T_c	20	30	40	50	60	80
30		446				
40	520	438	389	360	326	296
60		435				
80		434				

Notes:

T_c, T_{disc} – charging, discharging times (ms);
Middle cells – base pressures (torr).

The vacuum generation results are listed in Table 4-3. With gas discharging time of 40ms, the vacuum generation curves are shown in Figure 4-19. It takes around one hour to reach the base pressure. The lowest pressure with the initial round testing is 296 torr, which is 200 torr lower than the state-of-the-art micromachined displacement pumps reported in the world (refer to Chapter 1).

The initial round of testing points out that discharging time beyond 60ms does not help too much in improving the vacuum generation performance. Also the longer charging times definitely give lower base pressures. The second round testing further increases the charging time. The vacuum generation performance and pump speeds are studied in the next part.

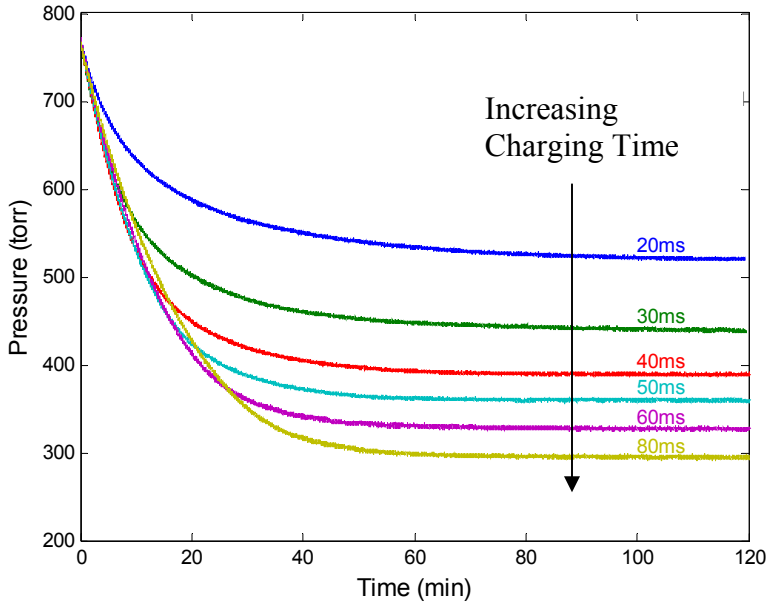

Figure 4-19: Vacuum generation curves of the initial round testing for the pump HZ2-B5.

3. The second round testing

The second round testing results are listed in Table 4-4. A base pressure of 206 torr has been achieved in 2.5 hours, as shown in Figure 4-20.

Table 4-4: The 2nd round vacuum generation results of the pump HZ2-B5.

T_{disc} \ T_c	20	30	40	50	60	80	120	160	200
40	520	438	389	360	326	296	246	215	206

Notes:

T_c, T_{disc} – charging, discharging times (ms);
Middle cells – base pressures (torr).

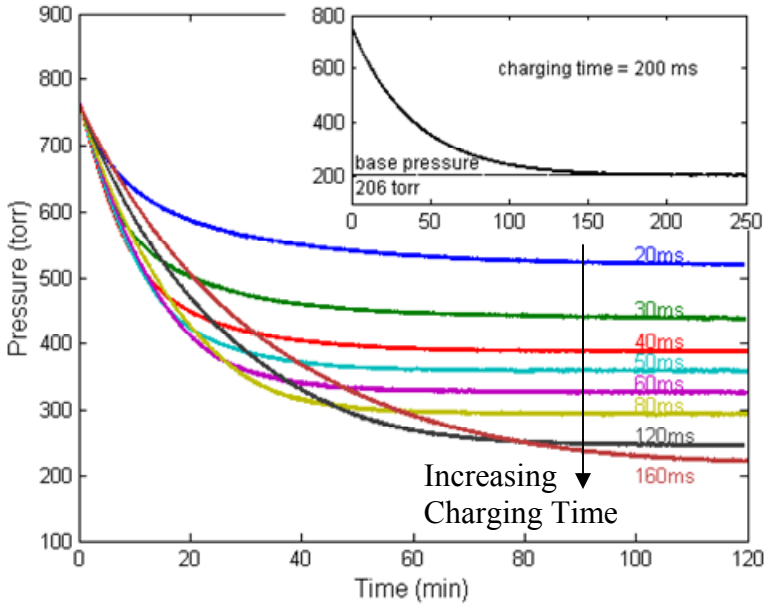

Figure 4-20: Vacuum generation curves of the first two rounds testing for the pump HZ2-B5.

The pressure derivative of the test volume can be converted to the pumping speed with Eq. 4-3 as below:

$$v_{pumping} = \frac{1}{P_t} \cdot \left(\frac{dP}{dt}\right)_{P_t} \cdot V_t \quad (Eq. 4-3)$$

where

$v_{pumping}$: pumping speed
P_t: test volume pressure
$(dP/dt)_{Pt}$: pressure derivative
V_t: test volume (~0.6 cm^3)

The pumping speed at four different pressure levels, 760 torr, 620 torr, 465 torr, and 310 torr, are drawn versus charging times in Figure 4-21. The peak pumping speeds occur at charging times of 30ms, 40ms, 60ms, and 120ms, respectively from 760 torr to 310 torr. The maximum pumping speed at atmospheric pressure is 0.027 sccm.

Another way to analyze the pumping speeds is to normalize the pumping speed to the cycle times. The pump speeds are then characterized as cm^3/cycle, which are drawn in

Figure 4-22. Normalized pumping speeds start to saturate at charging times of 45ms, 55ms, 70ms, and 110ms, for pressures of 760 torr, 620 torr, 465 torr, and 310 torr. The units are scc/cycle (standard cubic centimeter per cycle).

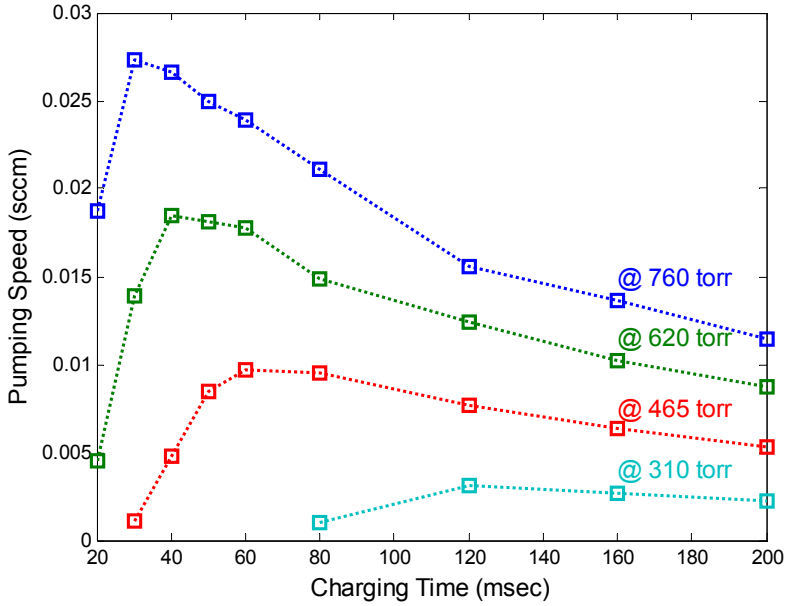

Figure 4-21: Pumping speeds at 760 torr, 620 torr, 465 torr, and 310 torr (HZ2-B5).

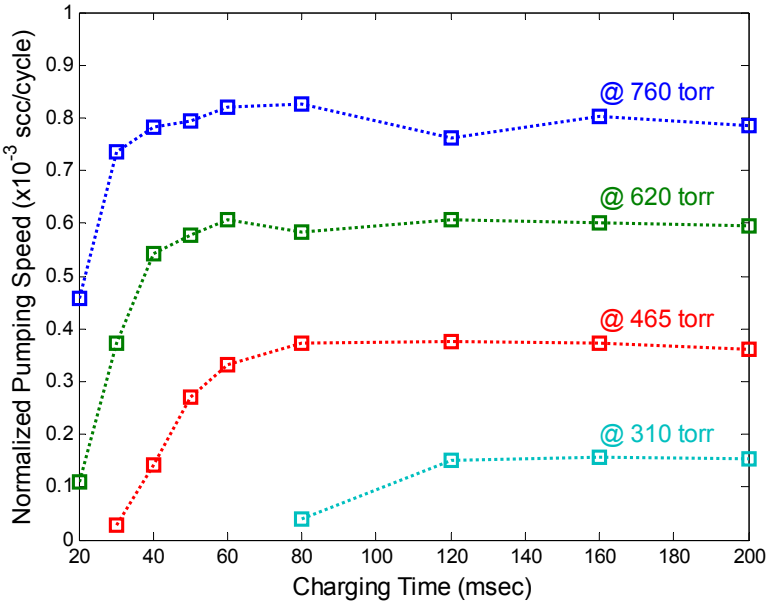

Figure 4-22: Pumping speeds at 760 torr, 620 torr, 465 torr, and 310 torr, normalized to cycle times (HZ2-B5).

The products of the pressures and the saturated charging times are 34.2, 34.1, 32.55, and 34.1 torr·sec for the pressures of 760, 620, 465, and 310 torr, respectively. The products equal to each other with a 5% tolerance. This finding validates our derivation of the gas time constant in Eqs. 2-1 ~ 2-7, which is the fundamental of our gas dynamic modeling.

4. The third round testing (Run 1)

From the first two rounds of testing results, we may find the optimal vacuum generation performance has not been reached and a longer charging time is required. On the other hand, longer operation time leads to more leak, which is discussed in great detail in Section 4.4. Pumping efficiency and system leak compete with each other, and a lowest base pressure is expected at a certain charging time. Another test chip (HZ2-A5) is chosen to study the competing phenomena and the charging time starts from 160ms, and increases incrementally to 640ms. The 3rd round testing results are included in Table 4-5, and the lowest base pressure of 164 torr is achieved.

Table 4-5: The 3rd round vacuum generation results for the pump HZ2-A5.

T_{disc} \ T_c	160	200	240	280	320	640
40	236	200				
60		186	173	**164**	165	207
80		188	173	168		

Notes:

T_c, T_{disc} – charging, discharging times (ms);
Middle cells – base pressures (torr).

The selected vacuum generation curves are shown in Figure 4-23. In about 2.5 hours, the pressure is reduced to below 200 torr. The pressure changes are also drawn versus operational cycles, as shown in Figure 4-24. Initial pressure derivatives are almost the same for the four curves, which agrees with the experimental results shown in Figure 4-22. Pumping speeds saturate when the gas charging time is above ~45ms. The effects of the charging time on vacuum generation performance are reflected when the pump is at the quasi-static states below 200 torr.

This round of testing is important to understand the vacuum generation performance of micromachined displacement pumps. The effects of insufficient gas charging time and

the pump leakage are studied based on this set of experimental results in Section 4.4. And to validate our understanding and hypothesis, parametric experiments are designed by varying the pump leakage and operation times.

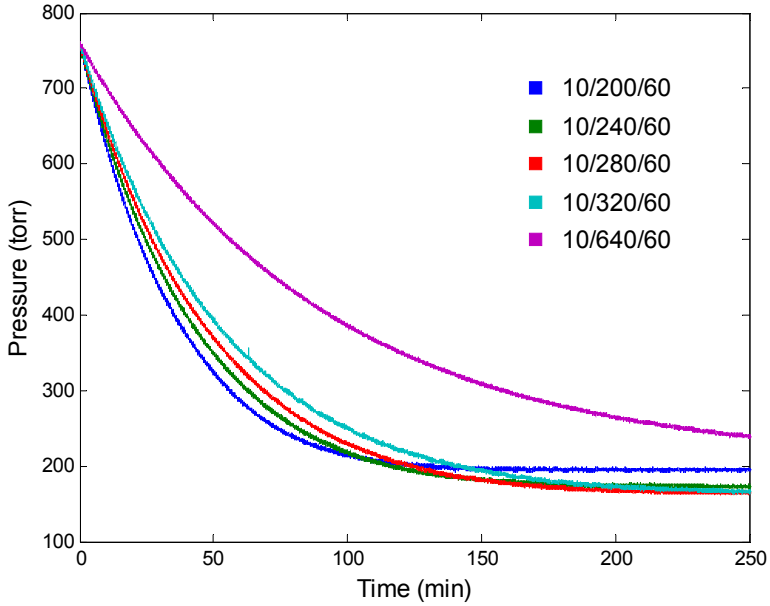

Figure 4-23: Vacuum generation curves for the pump HZ2-A5. Operation descriptions: e.g. 10/200/60 – valve operation times/charging time/discharging time.

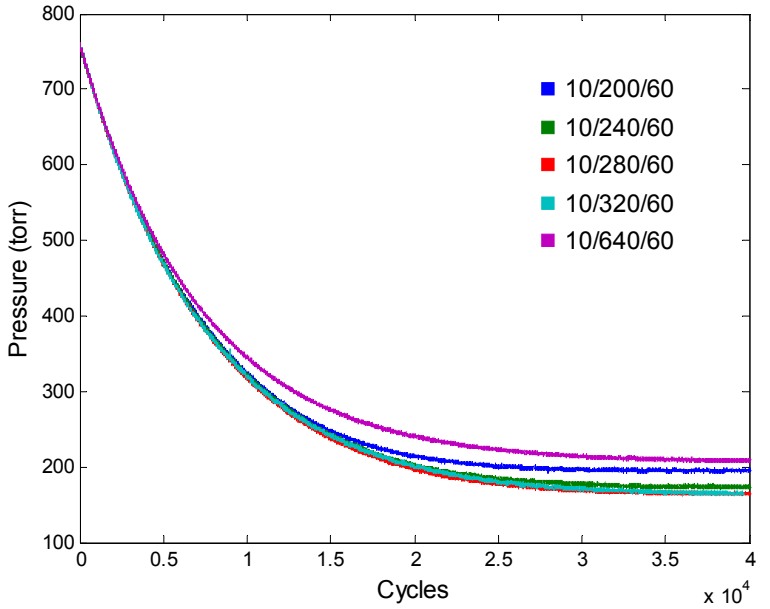

Figure 4-24: Vacuum generation curves for the pump HZ2-A5, normalized to cycle times.

5. Parametric testing (Run 2 &3)

The clamping of the test jig is tuned on purpose to vary the pump leak. The valve operation times are kept as 10ms, the gas discharging time is 60ms, and the charging times sweep from 120ms incrementally to 640ms. The experimental results of the ultimate base pressures are listed in Table 4-6 (Run 2). At the new leakage level, a valve operation time is increased by 100ms, and the new set of the vacuum generation results are listed in Table 4-7 (Run 3).

Table 4-6: Vacuum generation results – parametric testing (Run 2, more leakage, HZ2-A5).

T_{disc} \ T_c	120	160	200	240	280	320	360	400	480	640
60	262	230	211	202	208	207	224	236	260	295

Table 4-7: Vacuum generation results – parametric testing (Run 3, more leakage, 100ms longer valve operation time, HZ2-A5).

T_{disc} \ T_c	120	160	200	240	280	320	360	400	480	640
60	257	236	215	217	220	--	249	--	281	320

The three runs of vacuum generation results (Tables 4-5~7) are modeled with the lumped element modeling method. A concept of virtual dead volume is also developed to facilitate the analysis. The details are discussed in the following Section 4.4.

4.4 Experimental Results Modeling

The experimental results are modeled in this section and a full model of the micromachined displacement pumps for vacuum generation is developed thereafter.

4.4.1 Vacuum Generation: Run 1

By taking the virtual dead volume into consideration, the vacuum performance of displacement pumps is then a function of gas charging time:

$$P_v = \frac{P_0 \cdot V_d + P_0 \cdot Q_{leak} \cdot T}{V_d + V_p}$$
$$= \frac{P_0 \cdot [V_{d0} + Q_{leak} \cdot (T - T_c)]}{V_d + V_p} + \frac{P_0 \cdot V_p}{V_d + V_p} \cdot e^{-T_c/\tau} + \frac{P_0 \cdot Q_{leak}}{V_d + V_p} \cdot T_c \ (Eq. 4-4)$$

where

V_{d0}: the dead volume by design (total channel volume ~0.0043 mm^2)

If we assume the dead volume approximately constant at the pressure range, we may re-write the above equation as in Eq. 4-5a

$$P_v = K_1 + K_2 \cdot e^{-T_c/\tau} + K_3 \cdot T_c \ (Eq. 4-5a)$$

where the three constants K_1, K_2, and K_3 are

$$K_1 = \frac{P_0 \cdot [V_{d0} + Q_{leak} \cdot (T - T_c)]}{V_d + V_p} \ (Eq. 4-5b)$$
$$K_2 = \frac{P_0 \cdot V_p}{V_d + V_p} \ (Eq. 4-5c)$$
$$K_3 = \frac{P_0 \cdot Q_{leak}}{V_d + V_p} \ (Eq. 4-5d)$$

Eqs. 4-4 and 4-5a have three terms: 1) a constant term, which relates to leak rate and cycle time; 2) an exponential term, which shows the effect of the virtual dead volume as an exponential expression of the charging time; and 3) a linear term, which highlights the effect of the leakage during the charging step. And all the three terms are functions of the pumping volume and the dead volume as well. Eqs. 4-5b~d may be rearranged as below:

$$\begin{pmatrix} K_1 & K_1 & -P_0 \cdot (T - T_c) \\ K_2 & K_2 - P_0 & 0 \\ K_3 & K_3 & -P_0 \end{pmatrix} \begin{pmatrix} V_d \\ V_p \\ Q_{leak} \end{pmatrix} = \begin{pmatrix} P_0 \\ 0 \\ 0 \end{pmatrix} V_{d0} \ (Eq. 4-6)$$

The experimental results (Run1, as shown in Table 4-5) for the pump HZ2-A5 are fitted with the expression of Eq. 4-5a with the exponential term and linear term, as shown in Figure 4-25. The gas discharging time is 60ms, and the valve operation times are 10ms each. Exponential term and linear term are drawn separately as well with red dash lines.

The fitting parameters are:

$$\tau = 0.0855 \ sec$$

$$K_1 = 93.68\ torr$$
$$K_2 = 594.3\ torr$$
$$K_3 = 176.6\ torr/sec$$

A few discussions on these constants would improve our understanding of the pump performance and help to develop the comprehensive pump model.

(1) Time constant τ

Let us recall that the time constant calculated from FEA assisted lumped element modeling is 0.093 sec, which is only ~8% away from the time constant mathematical fit from experimental results.

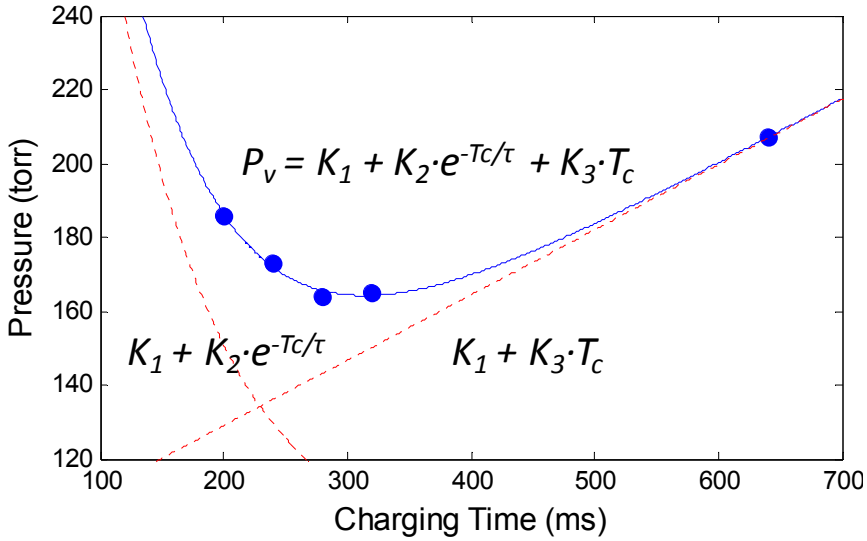

Figure 4-25: Vacuum generation performance versus charging time (HZ2-A5).

(2) Leak rate Q_{leak} *(Run 1)*

The leak rate calculated with Eq. 4-5 is *2.32/sec* × V_{d0} ≈ *0.01 mm*^{3}*/sec (standard)*. The leak rate can also be derived with Eq. 2-15b:

$$Q_{leak} = \frac{\Delta P}{R_{leak}} = \frac{\Delta P}{P_0} \cdot \frac{V_t}{\tau_{leak}} \quad (Eq. 4-7)$$

With the leak time constant of the chip A5, as shown in Figure 4-18, 5.96 × 10^4 seconds, the leak rate is calculated as

$$Q_{leak} = \frac{\Delta P}{P_0} \cdot \frac{V_t}{\tau_{leak}} \approx \frac{760 - 200}{760} \cdot \frac{0.6\ cm^3}{5.96 \times 10^4 s} = 0.0074\ mm^3/sec$$

The leakage rates calculated with two different approaches are close and the one from leak time constant is smaller by 26%. The latter one uses the approximate test volume pressure of 200 torr, which is higher than the exact value. Also the test volume is estimated with the geometry of the cavity, which might be underestimated due to the complexity of the sealed volume.

On the other hand, the accurate test volume might be derived from the leak rates. Use $Q_{leak} = 0.01\ mm^3/sec\ (standard)$, and $\Delta P = 560\sim600\ torr$, then

$$V_t = Q_{leak} \cdot \frac{P_0}{\Delta P} \cdot \tau_{leak} = 0.75\sim0.81\ cm^3$$

(3) Pumping volume V_p *(Run 1)*

The pumping volume is calculated from Eq. 4-6 with the values three constants K_1, K_2, and K_3 to be $7.82 \times V_{d0} \approx 0.0336\ mm^3$. If the pump chamber piston was actuated at the full stroke 10μm, the ideal chamber volume is calculated as a frustum of a cone

$$V_p\ (ideal) = \frac{1}{3}\pi h\left(r_{top}^2 + r_{bottom}^2 + r_{top} \cdot r_{bottom}\right) = 0.238 mm^3$$

where

r_{top}: chamber ceiling radius (3mm)
r_{bottom}: piston radius (2.5mm)

The experimental pumping volume is only 1/7X of the ideal value. The 1/7X difference can be explained by the combined contributions of the insufficient pneumatic actuation force and the fillet on the tether. From the FEA modeled curve in Figure 2-14, we can derive the chamber deflection at 100 torr pressure differential using interpolation

$$h_p(100\ torr) \approx 11.5 - 0.095 \times r\ \ (Eq. 4-8)$$

where

h_p: pumping deflection (in μm)
r: fillet radius (in μm)

If we further assume the linear response of the tether to the pneumatic actuation force, the pumping deflection then is

$$h_p \approx (11.5 - 0.095 \times r) \cdot \frac{P_a}{100} \quad (Eq. 4-9)$$

where

P_a: pneumatic actuation pressure differential (in torr)

If h_p is only 1/7 of the designed full stroke, i.e. 10μm/7 = 1.4μm, a set of actuation pressure and fillet radius is drawn in Figure 4-26.

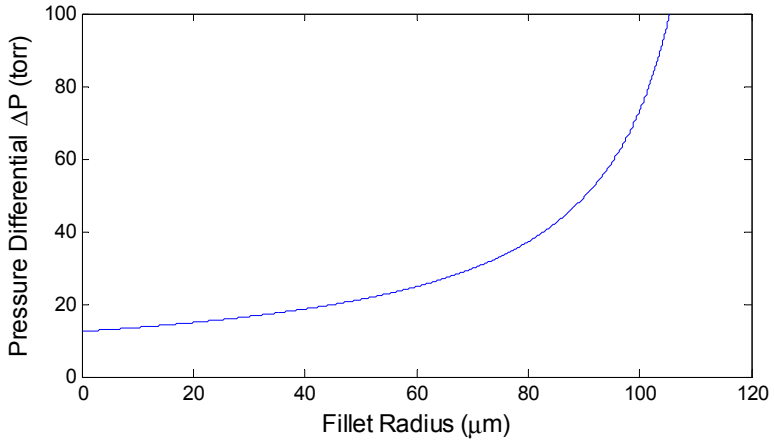

Figure 4-26: Combined effects of the fillet radius and actuation force for a 1/7X deflection (1.4 μm).

The typical fillets have radiuses of 40~80μm, and the corresponding actuation pressures ΔP are 20~40 torr. The limited actuation forces are also proved with actuation profile, as shown in Figure 4-11. Note that the location measuring the actuation pressures is not right at the chamber actuation cavity site but about 10cm away. The actuation on the pump chamber should have longer delay than the one indicated in Figure 4-11, and the actuation pressure differential will be smaller than ~100 torr. An in-situ pressure monitoring would help to obtain more accurate actuation pressures, however, the integration of a micro pressure sensor is beyond the scope of this thesis project.

4.4.2 Vacuum Generation: Parametric Testing

The most effective method to verify the modeling is using parametric testing. As discussed in the previous section, it is clear that constants τ and K_2 are relatively independent of testing runs. On the other hand, the leakage may differ if the assembly is changed in different runs. Parametric experiments are done with two additional runs:

Run 2: vary the test setup clamping from Run 1 on purpose, and the leakage changes.
Expectation: a larger leak rate should be derived than that in Run 1.
Run 3: use same assembly with Run 2, but change a valve operation time from 10ms to 110ms, which increases the time of $(T\text{-}T_c)$, i.e. changes the constant K_1 from Run 2.
Expectation: a larger K_1 should be obtained than that in Run 2.

The experimental results are listed in Table 4-6 for Run2 and 4-7 for Run 3. Using the same constants of τ and K_2 from Run 1, the Run 2 results are mathematically fitted:

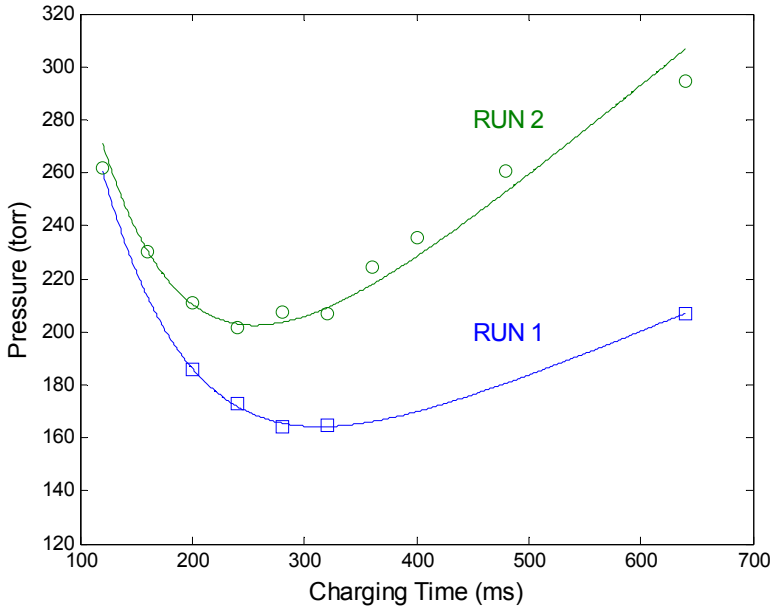

Figure 4-27: Vacuum generation performance for Run 1 & 2 (HZ2-A5).

Fitting parameters are

$$\tau(2) = \tau(1) = 0.0855\ sec$$
$$K_1(2) = 83.56\ torr$$
$$K_2(2) = K_2(1) = 594.3\ torr$$
$$K_3(2) = 348.2\ torr/sec$$

Discussion of the two constants K_1 and K_3 will give us more insight about the pump:

(1) Pumping volume V_p *(Run 2)*
For Run 2, the pumping volume is $12.2 \times V_{d0} \approx 0.0524\ mm^3$ which is 22% of the ideal value. If we assume the pumping volume is proportional to the piston deflection, the stroke is then 2.2μm. The chamber piston is actuated more efficiently than in Run 1 due to the higher pressure in the test volume. This is also an evidence of the pneumatic

actuation limit.

(2) Leak rate Q_{leak} *(Run 2)*
In Run 2, the leak rate is larger than that in Run 1 due to the loosened clamping, which becomes *7.1/sec* × $V_{d0} \approx 0.03\ mm^3/sec$ *(standard)*.

Furthermore, the Run 3 results are fitted as well, with constants τ, K_2, and K_3 from Run 2:

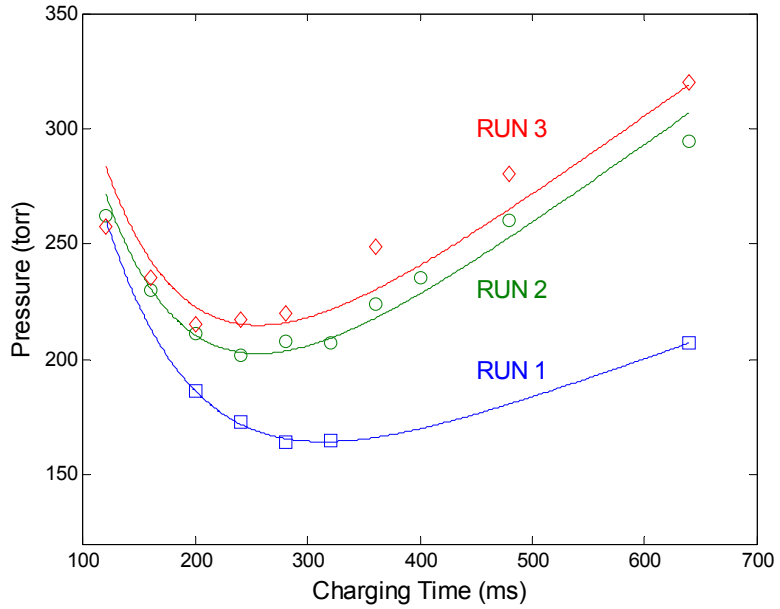

Figure 4-28: Vacuum generation performance for Run 1, 2, & 3 (HZ2-A5).

Fitting parameters are

$$\tau(3) = \tau(2) = \tau(1) = 0.0855\ sec$$
$$K_1(3) = 95.86\ torr$$
$$K_2(3) = K_2(2) = K_2(1) = 594.3\ torr$$
$$K_3(3) = K_3(2) = 348.2\ torr/sec$$

It is not surprised that $K_1(3) > K_1(2)$ since $(T - T_c)(3) > (T - T_c)(2)$, while other parameters remain the same.

The model developed in this section based on lumped element modeling for the vacuum generation of the displacement pumps is helpful in explaining the experimental results, but more importantly, it has also been demonstrated a very powerful tool to predict the pump behavior and provide a clear direction for future improvement.

4.5 Further Exploration

4.5.1 Current Challenges in Pump Characterization

From the measurement of the actuation profile and analysis of the experimental results, we have obtained various evidences of the pneumatic actuation limit. When the test volume pressure is low, e.g. 164 torr, the actuation force during gas charging step is insufficient, and the pump chamber does not deflect to its full stroke. The challenges in pump characterization are also shown in a three step experiment as shown in Figure 4-29.

The single-stage pump is operated at the optimal sequence: 10ms for all the valve operations, 280ms for gas charging and 60ms for gas discharging. The outlet pressure changes twice, from 760 torr to 300 torr, and then to 160 torr. However, the base pressure decreases from ~200 torr to 135 torr, and then to 133 torr. The flow is in continuous regime and the base pressure should be proportional to the ambient pressure if the pump chamber and valves are actuated at the same level, which is far from the experimental observations. The best explanation is the deflection decreases due to insufficient pneumatic vacuum actuation force. To study the ultimate capability of the micromachined displacement pump for vacuum generation, the vacuum actuation has to be replaced with another kind of the actuation.

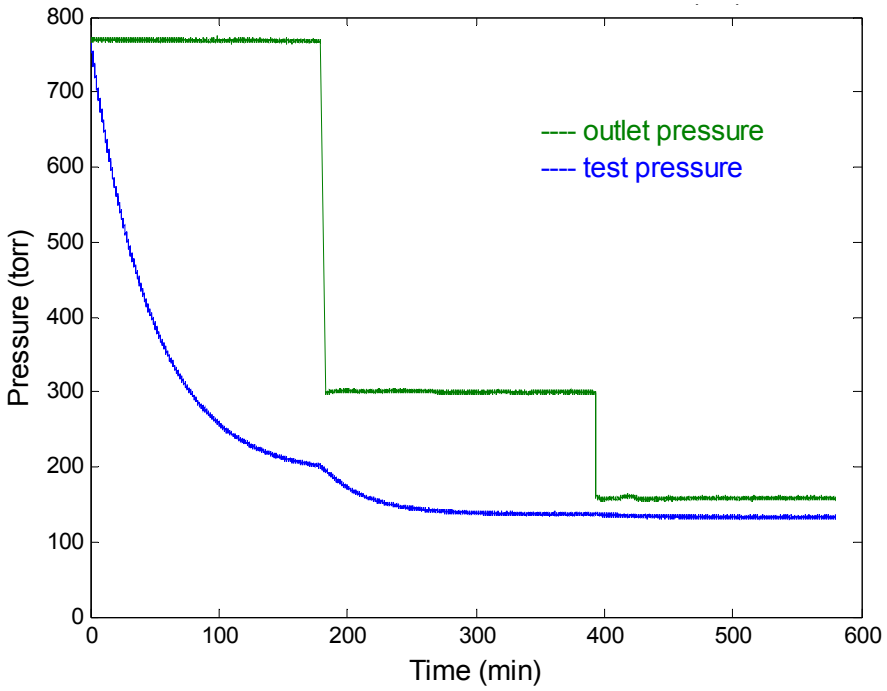

Figure 4-29: Three step vacuum generation experiments for the single-stage pump.

4.5.2 Hybrid Actuated Testing

For characterization purpose of the displacement pumps for vacuum generation, another actuation is proposed to study their ultimate vacuum capability and to demonstrate the second-stage pump. Electromagnetic solenoid is used for the first trial, e.g. Bicron SCO424N0600. For example, a hole is opened on a test die of a two-stage pump, as shown in Figure 4-30. The second stage pump chamber is actuated with the solenoid. The other chamber and the four valves continue to be actuated pneumatically.

A tube is glued to the second-stage chamber piston. The actuation force against the pressure differential should be larger than 1 Newton, and the adhesion strength should be sufficient. For that sake, the glue is tested first. A simple testing method is shown in Figure 4-31. The tube is glued to a silicon chip, and a weight is hanged on the silicon chip. Among a few instantly available glues, epoxy is the strongest as shown in Figure 4-31 with the weight of ~170g (1.66N) for static testing. Dynamic testing on epoxy has also been done, and the glue has been functional through tens of hours of operation.

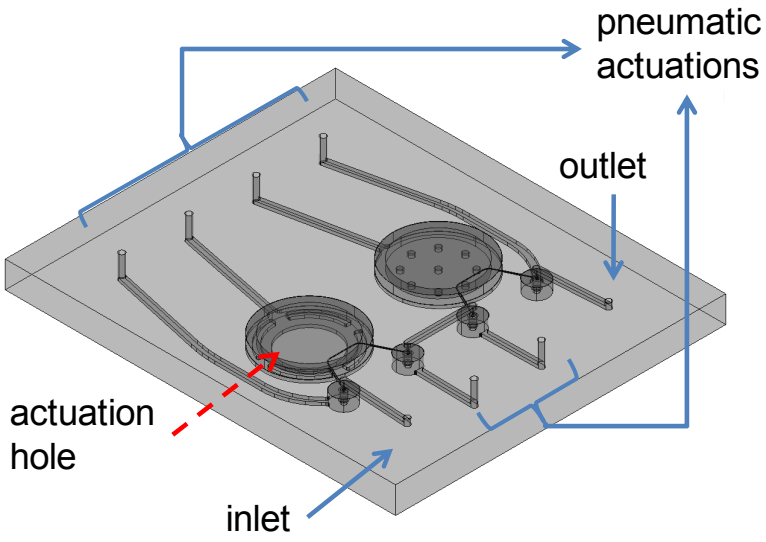

Figure 4-30: Schematic view of the hybrid actuated test die.

The solenoid is attached to the connecting tube to complete the test setup, as demonstrated in Figure 4-32. The actuation force of the electromagnetic actuator is independent of the test volume pressure, which was the case for pneumatic actuations. With the hybrid actuated testing, the single-stage pumps would be able to be studied further and the two-stage pumps could be demonstrated.

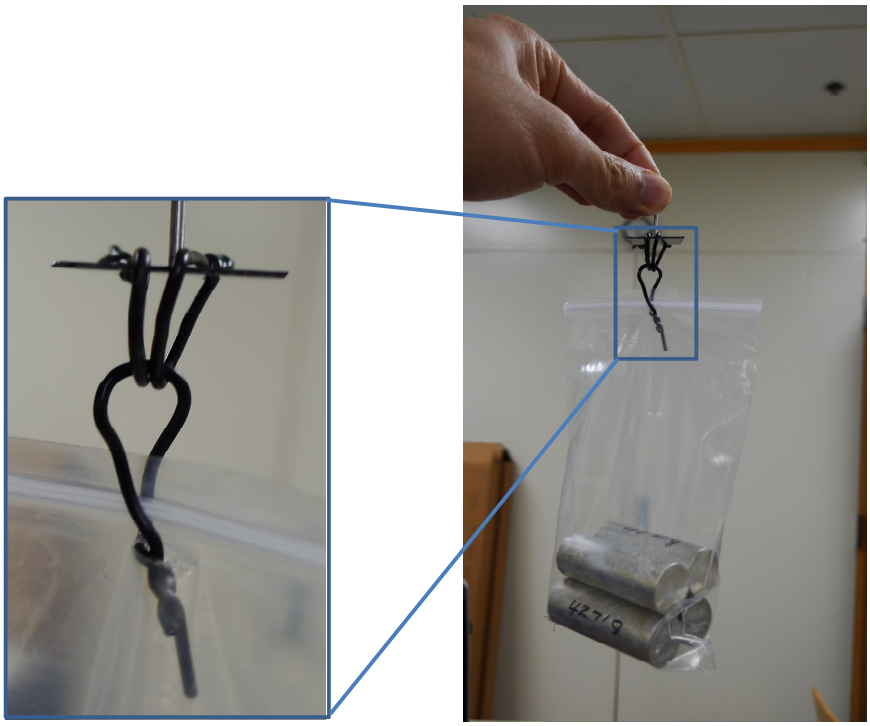

Figure 4-31: Epoxy strength testing with 170 gram weight.

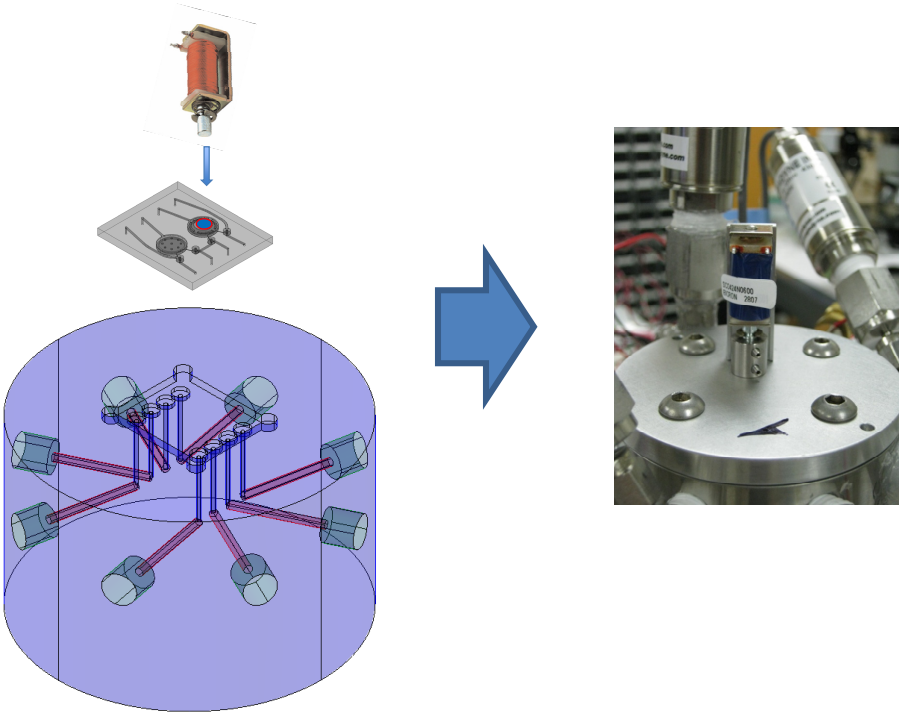

Figure 4-32: Hybrid testing setup.

4.6 Summary

In this chapter, the characterization of the micromachined displacement pumps is presented. The testing strategy is firstly discussed, and the testing setup is then built following the testing plan. The testing results of the prescreening flow measurements, the leakage testing, and the vacuum generation testing are presented.

Based on parameter sweeping testing and parametric testing results, a universal model on the vacuum generation performance of the micromachined displacement pumps is developed. The model is independent of actuation mechanism and can be used to understand any micro displacement vacuum pump, along with the mechanical modeling of the deflection for some specific actuations and the preliminary leakage characterizations.

Limits of the pneumatic actuation are also discussed. For better understanding of the displacement pumps for vacuum generation, a hybrid actuated testing is proposed to demonstrate the ultimate capability of our pumps. Further discussions are included in the following Chapter 5.

Chapter 5

Future Development

In this chapter, the contribution of this thesis is firstly summarized. Limit of the current design and characterization is discussed, and the integration of micro actuators for vacuum generation is introduced. Finally, future development plans are suggested.

5.1 Thesis Contribution

We have developed a micromachined displacement pump for vacuum generation. The contributions of this thesis include:

1. The pump has been carefully designed to minimize the dead volume and to improve valve sealing.
   a. Miniature device size. The diameter of the pump chamber is 6mm, and a single-stage pump is only 8mm wide, 10mm long, and 2mm thick by design.
   b. Planar connecting channels. There are no traditional vertical through wafer holes between the pump chamber and the valves, which reduces the dead volume.
   c. Normally-closed design. The chamber and the two valves are closed in idle state, to reduce dead volume between two actuation states.
   d. Better sealing. Valve seat surface roughness is minimized to improve the surface quality for better sealing.
   e. The fluid ports are moved to the side opposite the actuators to facilitate the integration of actuation in the future generations.

2. The pumps are fabricated in house with 10 photo masks.
   a. All silicon wafers for the four layers. All the four layers are RCA cleaned and bonded altogether simultaneously. Contamination is minimized during the pump assembly.
   b. Deep-reactive ion etching recipe is fine tuned to form the fillet and clean bottom profile, which improve the robustness of the pumps.
   c. Stress compensation. Thermal oxide is used to compensate the buried oxide stress.

3. The single-stage pump has been characterized in details.
   a. Systematic testing strategy has been designed. Pneumatic actuation is used for characterization purpose.
   b. The testing setup has been built to fulfill the testing plan.
   c. Pump leakage is characterized.
   d. The micro displacement pumps have been measured for vacuum generation. Parameter sweeping testing is done and parametric testing is used for a better understanding of the pump vacuum performance.
   e. Through optimization of design and operation, we can now report a pump that achieves 164 torr absolute pressure, which is to our knowledge the lowest measured pressure in a micromachined vacuum pump operated from atmospheric pressure.

4. The experimental results are analyzed and modeled.
   a. Mechanical behavior is analyzed for the pump chamber and the valve.
   b. Computer aided modeling is done to explain the leakage and vacuum generation results.
   c. A universal model is developed based on the mechanical analysis and gas dynamics modeling. Our understanding on the vacuum generation performance of the micro displacement vacuum pumps is further improved.

5.2 Integrated Actuations

The micromachined vacuum pumps will be ultimately integrated with micro actuators for portability purposes. The use of single crystal piezoelectric actuators has been demonstrated to be integrated with hydraulic pumps [11]. The piezoelectric actuators provide a very large actuation force, however, the piezoelectric actuators could be only integrated manually die by die. To improve the yield, the actuators might be better integrated at wafer level. As discussed in Section 1.4, the electrostatic zipper actuators are most promising to actuate the displacement pumps, which could also provide an adequate force.

A schematic of a single-stage micromachined displacement pump is shown in Figure 5-1, with three electrostatic zipper actuators integrated to actuate the two valves and one chamber. The actuator is different from most micro electrostatic zipper actuators reported in the way of actuation directions. The micromachined displacement pumps developed in this thesis work need to be actuated vertically, and the electrostatic zipper actuators would be designed accordingly.

The design of the vertical electrostatic zipper actuators includes a curved substrate and thin top electrodes, as highlighted in green and orange colors in Figure 5-1. The curved substrate might be fabricated with materials other than silicon, such as aluminum alloy or stainless steel by metal milling or conductive polymers by plastic molding. But silicon is still the first choice for its microfabrication compatibility. One way to form the curved silicon substrate is to use the plastic deformation mechanism of silicon at elevated temperature over 900^{o}C, as described in [44]. The top electrodes may be fabricated with the device layer of silicon-on-insulator (SOI) wafer or plain silicon wafers, with the aid of chemical-mechanical-polishing and other standard microfabrication techniques. And if the electrostatic zipper actuators are also developed with silicon wafers, the micromachined displacement pump could be integrated with the actuators with direct fusion bonding.

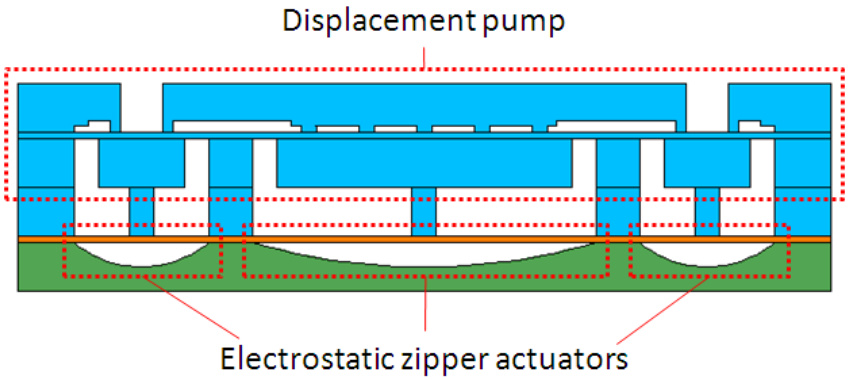

Figure 5-1: Schematic cross-section of a single-stage micromachined displacement pump with electrostatic zipper actuators integrated (courtesy of Hanqing Li).
Blue: the single-stage micromachined displacement pump.
Orange: the top electrodes of the electrostatic zipper actuators.
Green: the substrate of the electrostatic zipper actuators.

5.3 Suggestions for Future Development

A universal model on the vacuum generation performance of the micromachined displacement pumps has been developed in this thesis work. The model is independent of actuation mechanism and can be used to understand any micro displacement vacuum pump. The model is powerful in three ways: 1) explaining the experimental results; 2) predicting the pump vacuum generation performance; and most importantly, 3) revealing the specific properties of the pump or the testing setup. The first two parts have been

demonstrated in this thesis Chapter 4. The experimental results of Run 1 (Section 4.4) were modeled, and by intentionally increasing the system leakage, the corresponding constants (*K's* and τ) were predicted in Run 2 & 3. The hidden properties of the micromachined displacement pump have also been calculated, the time constant τ, the leakage Q_{leak}, and the pumping volume V_p. By comparing the calculated values and the designed values, the directions of future development could be decided. For example, to continue the research on the micromachined displacement pumps based on this thesis work, a few important modifications could be made:

1. Alternative actuation for characterization purposes. The pumping volume is far less than the designed value, which has suggested an insufficient pneumatic actuation force at the final vacuum level. To demonstrate the ultimate vacuum generation performance of the micromachined displacement pumps, the pump chambers should be actuated by other actuation mechanisms. Before the micro-actuators are fully developed and integrated into the pump, a hybrid actuation might be needed, such as the example in Section 4.5.2.

2. Integrated test volume. Currently the test volume is defined on the test jig, and the test volume is connected to the pump chip through channels and connectors on the jig. As illustrated earlier, the parasitic leak from the connections may contribute more than 50% of the total leakage. If there is no parasitic leak, the micro vacuum pump would further evacuate the test volume by another 39 torr to 125 torr. To better characterize the pump or to achieve a lower base pressure, the test volume should be fabricated on the silicon chip and there would be no connection leak between the test volume and the pumping components. For an integrated test volume, a micro pressure sensor should also be included inside the test volume, which may require additional processes.

3. Integrated actuators. To complete the micro rough pump, the actuators should be integrated. The development of an electrostatic zipper actuator will comprise of the fabrication of the substrate, the formation of the top electrodes, and finally the integration of the actuators into the pump.

4. Pump redesign. The pump structure may also be further optimized to achieve a lower base pressure. For example, the height of the channels connecting the valves to the chamber is 10μm for the pump presented in this thesis work, but the height can be even smaller to reduce the dead volume. The chamber diameter can also be tuned. A larger pump chamber would decrease the effect of dead volume, i.e. the ratio of the dead volume over the pumping volume would be smaller. However, the operational time constants for gas charging and discharging steps are subsequently larger, which might require larger charging or discharging times. A larger leakage then follows. The pump is

then able to be engineered for a lower base pressure, and a redesign of the pump is necessary.

5. Fundamental study of valve leakage. A thorough understanding of valve leakage is essential to improve the pump valve sealing and further lower base pressure. A systematic study on the silicon valve leakage is then needed. The parameters that influence the valve leakage, such as the surface roughness of the valve seat and valve boss, the valve seal ring width, and the sealing force, could be vary. The valve sealing performance could also be studied at various pressures. Besides, a coating of soft layers on the silicon valves might further improve the valve sealing and lead to a smaller base pressure.

Aside from the development of the next generation micromachined displacement pumps for vacuum generation, the integration of the rough pump with other pump components, such as the separation valve between the rough pump and the ion pumps, should also be taken care of.

5.4 Summary

In this chapter, the contribution of the thesis is first summarized. A micromachined displacement vacuum pump is designed, fabricated, and characterized. The pump has achieved 164 torr absolute pressure, which is to our knowledge the lowest measured pressure in a micromachined vacuum pump operated from atmospheric pressure. More importantly, a complete pump model is developed based on our systematic understanding of the micro displacement pumps for vacuum generation. Based on the powerful model, the micromachined displacement pumps can be further improved. A few suggestions for further development are finally proposed in this chapter.

Appendix

Appendix A Mechanical Analysis

A.1 Plate Formulas

The mechanical structure of the chamber or the valve is redrawn in Figure A-1, with the tether region and the piston in the center.

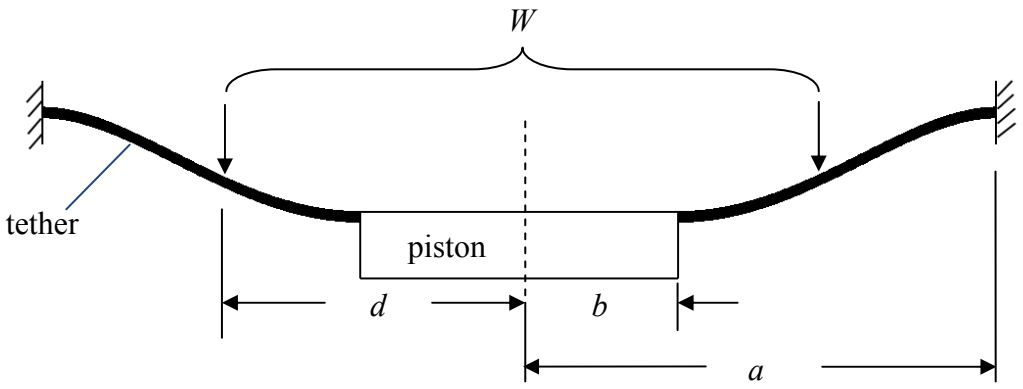

Figure A-1: Schematic drawing for plate deflection modeling.

The piston thickness (575μm) is much larger than the tether thickness (10μm), and we can then assume the piston is rigid compared to the tether part. The outer edge of the tether is fixed to the bulk silicon. The inner edge of the tether is also fixed to the rigid piston. The boundary conditions are then as below:

1. $w = 0$ when $r = a$
2. $dw/dr = 0$ when $r = a$
3. $dw/dr = 0$ when $r = b$

where

w: the deflection;
r: the position of the deflection;
a,b: outer and inner.

For pneumatic actuation, there is a pressure differential applied on the tether and the piston, as shown in Figure 2-10. The deflection of the piston is restricted by the deflection stops to be less than 10μm, which is much smaller than the diameters of the chamber and the valve, 6mm and 1.5mm respectively. So the load on the tether is

simplified to uniformly distributed load vertically applied, as shown in Figure 2-11. Besides, the load on the piston is also simplified to load applied on the concentric circle with the radius of *b*, as shown in Figure A-1.

For the case that there is a uniform load applied on a concentric circle of plate, as *W* in Figure A-1, the deflection for the inner portion of plate, $b \le r \le d$, is as shown in [35]:

$$w(W,r) = \frac{Wa^2}{8\pi D}\left(\frac{a^2}{a^2-b^2}\right)\left\{\left(1-\frac{d^2}{a^2}\right)\left[\left(1-\frac{b^2}{a^2}\right)-\frac{1}{2}\left(1-\frac{r^2}{a^2}\right)\right]+\frac{b^2}{a^2}\left(1-\frac{d^2}{a^2}\right)\ln\frac{d}{r} + \left(\frac{2b^2}{a^2}-\frac{d^2}{a^2}-\frac{r^2}{a^2}\right)\ln\frac{a}{d}-\frac{2b^2}{a^2}\left(\ln\frac{a}{d}\right)\ln\frac{a}{r}\right\} \quad (Eq.A-1)$$

And the maximum deflection is

$$w_{max}(W) = \frac{Wa^2}{8\pi D}\left[\frac{1}{2}\left(1-\frac{d^2}{a^2}\right)+\frac{b^2}{a^2-b^2}\ln\frac{a}{b}-\frac{d^2}{a^2-b^2}\left(\frac{b^2}{a^2}\ln\frac{d}{b}+\ln\frac{a}{d}\right) - \frac{2b^2}{a^2-b^2}\left(\ln\frac{a}{b}\right)\ln\frac{a}{d}\right] \quad (Eq.A-2)$$

The factor *D*, the flexural rigidity of the plate, is defined as

$$D = \frac{EI}{1-\nu^2} = \frac{Eh^3}{12(1-\nu^2)} \quad (Eq.A-3)$$

where

h: the thickness of the plate
v: Poisson's ratio

For the segment ring with the width *dr* where $b < r < a$, the load $W = P \cdot 2\pi r dr$, and Eq. A-2 is converted to

$$w_{max}(P,r) = \frac{P\cdot 2\pi r dr\cdot a^2}{8\pi D}\left[\frac{1}{2}\left(1-\frac{r^2}{a^2}\right)+\frac{b^2}{a^2-b^2}\ln\frac{a}{b}-\frac{r^2}{a^2-b^2}\left(\frac{b^2}{a^2}\ln\frac{r}{b}+\ln\frac{a}{r}\right) - \frac{2b^2}{a^2-b^2}\left(\ln\frac{a}{b}\right)\ln\frac{a}{r}\right] \quad (Eq.A-4)$$

So the deflection of the piston is the superposition of the displacements driven by all the segments of the actuation force:

$$w(piston) = \int_b^a w_{max}(P, r) + w_{max}(P \cdot \pi b^2, b)$$
$$= \int_b^a \frac{P \cdot 2\pi r \cdot a^2}{8\pi D}\left[\frac{1}{2}\left(1 - \frac{r^2}{a^2}\right) + \frac{b^2}{a^2 - b^2}\ln\frac{a}{b} - \frac{r^2}{a^2 - b^2}\left(\frac{b^2}{a^2}\ln\frac{r}{b} + \ln\frac{a}{r}\right)\right.$$
$$\left. - \frac{2b^2}{a^2 - b^2}\left(\ln\frac{a}{b}\right)\ln\frac{a}{r}\right] dr$$
$$+ \frac{P \cdot \pi b^2 \cdot a^2}{8\pi D}\left[\frac{1}{2}\left(1 - \frac{b^2}{a^2}\right) + \frac{b^2}{a^2 - b^2}\ln\frac{a}{b} - \frac{b^2}{a^2 - b^2}\left(0 + \ln\frac{a}{b}\right)\right.$$
$$\left. - \frac{2b^2}{a^2 - b^2}\left(\ln\frac{a}{b}\right)\ln\frac{a}{b}\right] \quad (Eq. A - 5)$$

Eq. A-5 is used to calculate the deflections of the valve and chamber pistons that are subject to pressure differential. Note that the unit

For an actuation pressure, *ΔP = 100 torr*, the deflections of the pistons are 12.4μm and 2.14μm for the chamber and the valve, respectively, with the material Young's modulus and the dimensions in Table A-1.

Table A-1: Piston deflections for chamber and valve pistons with *ΔP = 100 torr* actuation.

	Chamber	Valve
Young's Modulus, E	170 GPa	170 GPa
Diaphragm Thickness, h	10μm	10μm
Radius, a	3mm	0.75mm
Piston Radius, b	2.5mm	0.25mm
Piston Deflection	12.4μm	2.14μm

A.2 MATLAB Code for Mechanical Analysis

```
clear
clc

syms d;

% Dimensions for the chamber: a = 3mm, b = 2.5mm.
% Dimensions for the valve: a = 0.75mm, b = 0.25mm (not shown here).
a = 3e-3;
b = 2.5e-3;

% Poisson ratio of silicon: 0.28
pratio = 0.28;
% Young's modulus: 170GPa
E = 170e9;
% Diaphragm thickness: 10um
h = 10e-6;
I = h^3/12;
D = E*I/(1-pratio^2);
% pressure "p" = 100 torr
p = 100*133.3;

% Deflection caused by the load applied on the tether directly, "wr1".
r = b;
c1 = (1-d^2/a^2)*((1-b^2/a^2)-1/2*(1-r.^2/a^2));
c2 = b^2/a^2*(1-d^2/a^2)*log(d./r);
c3 = (2*b^2/a^2-d^2/a^2-r.^2/a^2)*log(a/d);
c4 = -2*b^2/a^2*log(a/d)*log(a./r);
w = (2*pi*d*p)*a^2/(8*pi*D)*(a^2/(a^2-b^2))*(c1+c2+c3+c4);
wr1 = double(int(w,b,a));

% Deflection caused by the load applied on the piston, "wr2".
d2 = b;
c12 = (1-d2^2/a^2)*((1-b^2/a^2)-1/2*(1-r.^2/a^2));
c22 = b^2/a^2*(1-d2^2/a^2)*log(d2./r);
c32 = (2*b^2/a^2-d2^2/a^2-r.^2/a^2)*log(a/d2);
c42 = -2*b^2/a^2*log(a/d2)*log(a./r);
wr2 = (pi*b^2*p)*a^2/(8*pi*D)*(a^2/(a^2-b^2))*(c12+c22+c32+c42);

% Total deflection, "wr".
wr = double(wr1+wr2)

% Results:
%     2.1413um for the valve; 12.402um for the chamber
%     for 100 torr pneumatic actuation
```

Appendix B Fluid Dynamics Analysis

B.1 Validation of FEA Method for Fluidic Resistance Calculation

The most asked question about numerical method is the validity or accuracy of the computer modeling results. To build the confidence in using computer-aided method for our study, I will validate the simulation results by comparing them to the analytical solutions. For incompressible Poiseuille flow between stationary parallel plates, the flow profile is parabolic and the lumped element model for a Poiseuille flow path is as shown in [37]:

$$R = \frac{12\eta L}{Wh^3} \ (Eq.B-1)$$

where

R: fluidic resistance
η: fluid viscosity
W, L, h: channel width, length, and height

The analytical solution requires the channel width and length are much larger than the height (W, L ≫ h). The height of our pump is ~10μm, and the validation will be conducted with channel heights of 8~12μm.

A FEA package COMSOL Multiphysics® is chosen for computer aided modeling in this thesis. Channels with the widths of 1mm, 2mm, and 3mm, the lengths of 1cm and 2cm are modeled. Flow rate is calculated by integrating the flow velocities on the inlet or outlet surfaces. The fluidic resistances are then calculated with Eq. B-1 and listed in Table B-1 (a) & (b). Flow viscosity and pressure differential are set to be 1×10^{-3} Pa·s and 10 torr, respectively, for characterization purpose.

Table B-1 (a): FEA modeled fluidic resistances for L = 1cm (unit: 10^{14} Pa·s·m^{-3})

W \ h	8μm	9μm	10μm	11μm	12μm
1mm	2.7980	1.9658	1.4333	1.0769	0.8295
2mm	1.3992	0.9827	0.7164	0.5383	0.4146
3mm	0.9327	0.6551	0.4776	0.3588	0.2764

Table B-2 (b): FEA modeled fluidic resistances for L = 2cm (unit: 10^{14} Pa·s·m^{-3})

W \ h	8μm	9μm	10μm	11μm	12μm
1mm	5.5977	3.9317	2.8664	2.1537	1.6591
2mm	2.7984	1.9654	1.4329	1.0765	0.8292
3mm	1.8655	1.3103	0.9552	0.7176	0.5528

(1) Fluidic resistance versus channel height

First, we draw the plot of the logarithm of fluidic resistances versus the logarithm of channel heights, as shown in Figure B-2. The slopes of log(R) vs. log(h) range from -2.9986 to -2.9999, which are rounded to -3, i.e.

$$R \propto h^{-3}$$

(2) Fluidic resistance versus channel width and height

From Table B-2 (a) & (b), it is clearly shown that $R \propto W^{-1}$, and $R \propto L$

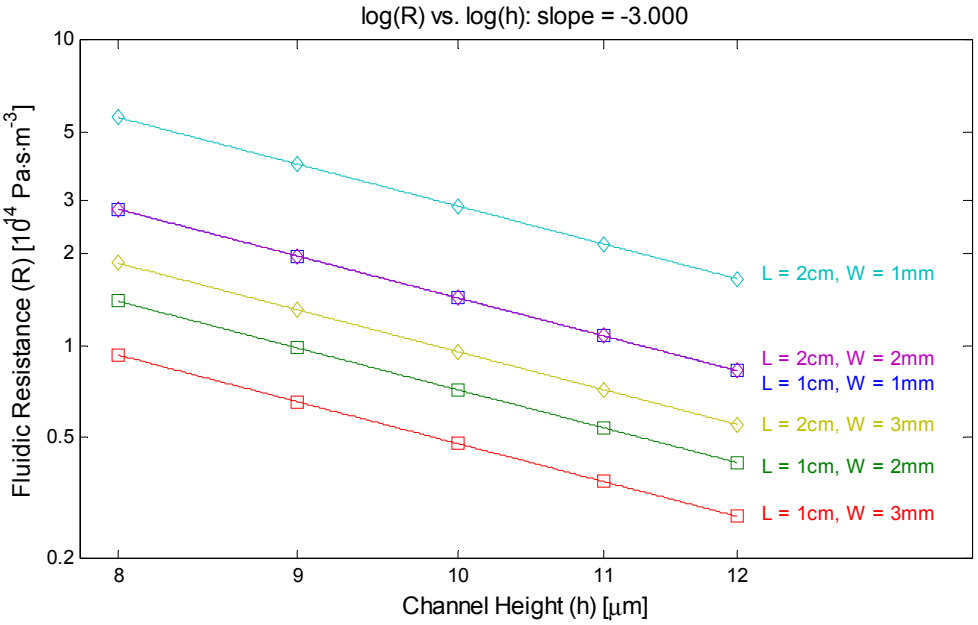

Figure B-2: Fluidic resistance versus channel height.

(3) The prefactor

From (1) & (2), we can see the FEA modeling also gives a relationship of the fluidic resistance with the dimensions as shown in Eq. B-2, the same with analytical solution:

$$R \propto \frac{L}{Wh^3} \ (Eq.B-2)$$

The last question is how close the prefactor derived from the FEA modeling results to 12 given in the analytical solution. Calculations with the results in Table B-2 (a) & (b) give the prefactor ranging from 14.3257~14.3343, with a mean value of 14.3293. The number is close to the theoretical value of 12 but 19.4% higher.

Coarse meshing is the reason why the prefactor is higher, which is also common with numerical analysis. In FEA modeling, the entire structure is meshed with finite segments, and the value inside each segment is derived using interpolation method. A finer meshing, 10 segments for the 10μm thickness, is shown in Figure B-3. With this meshing, a more accurate modeling result is obtained, as shown in Figure B-4. The prefactor calculated with the finer meshing is 12.868, which is only 7.2% off the theoretical value.

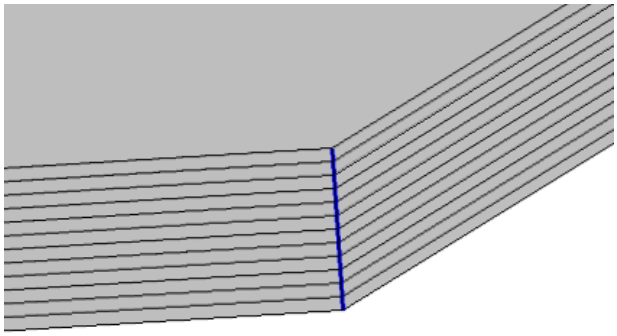

Figure B-3: Meshing in the FEA modeling.

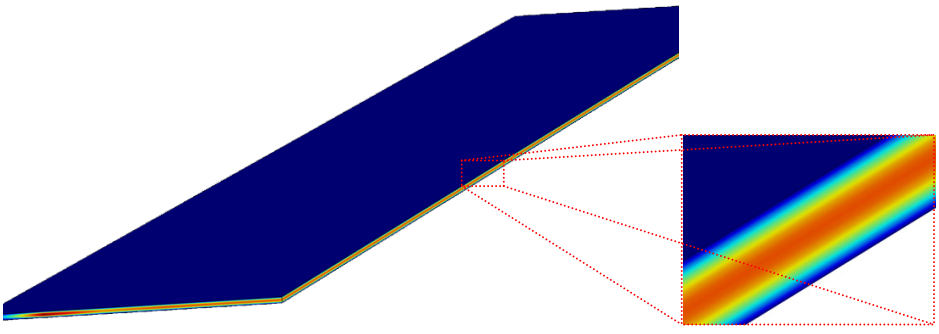

Figure B-4: FEA modeling results (velocity magnitude).

Aside from the resistance comparison, the flow velocities along the thickness also follow clearly the parabolic profile, as illustrated in Figure B-5. The parabolic profile is essential to derive the analytical solution of fluidic resistance for Poiseuille flow. As derived in [37], the velocity profile follows the expression in Eq. B-3:

$$u = \frac{1}{2\eta}[z(h-z)]\frac{\Delta P}{L} \quad (Eq.B-3)$$

The fitting curve uses the equation $u = c[z(h-z)]$, which perfectly matches the FEA modeling results with the constant $c = 0.5013$. As a reference, the prefactor used in the FEA modeling $\Delta P/2\eta L = 0.5$ with a 0.26% difference from modeling result.

With the comparison of fluidic resistance and flow profile between FEA modeling results and analytical solutions for parallel plates, we can then draw the conclusion that FEA tools, in particular COMSOL Multiphysics® used here, are adequate to model the fluidic resistance. Even with very coarse meshing, the modeling results is within 80% accuracy and finer meshing can improve the modeling to over 90% accuracy.

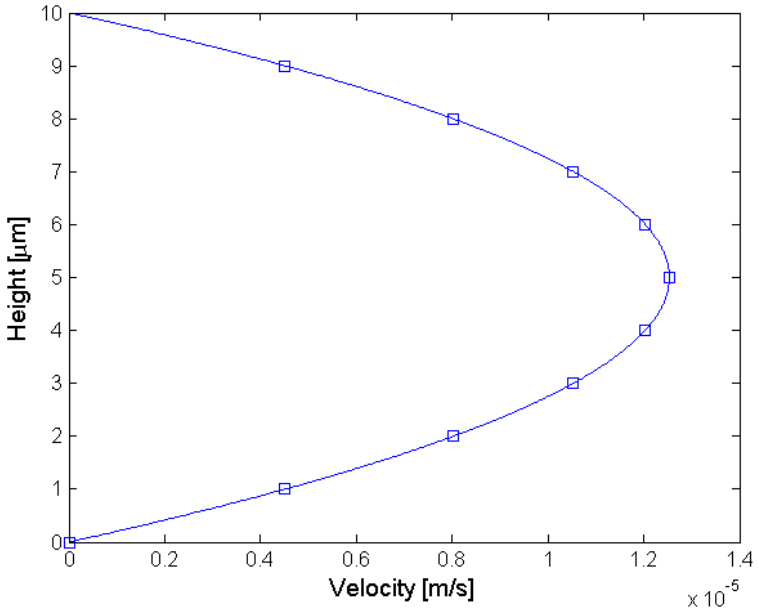

Figure B-5: Parabolic profile of the flow derived from FEA modeling. Squares: FEA modeling results; the line: mathematical fitting curve.

B.2 MATLAB Code for Fluidic Dynamics Analysis

1. Flow Rate

The fluidic dynamics is modeled with a FEA package COMSOL Multiphysics (simplified as "COMSOL" in the following context). The COMSOL model is saved as .m file, and the modeling results can be further analyzed with MATLAB. The code below is an example to extract the flow rate inside a rectangular channel.

File: `FlowRate.m`

```
% To extract the flow rate of a rectangular channel.
clear
clc

% Call the COMSOL model.
COMSOL_MATLAB_example;
model=ModelUtil.model('Model');

% Integral of velocity "v" within the channel volume.
val = mphint(model,'v');

% flowrate = val/length for a simple channel;
L = 1e-2;
flowrate = val/L;
```

File: `COMSOL_MATLAB_example.m (generated from COMSOL and called by flowrate.m)`

```
function out = model
%
% COMSOL_MATLAB_example.m
%

import com.comsol.model.*
import com.comsol.model.util.*

model = ModelUtil.create('Model');

model.modelPath('D:\Work');
model.modelNode.create('mod1');
model.geom.create('geom1', 3);
model.mesh.create('mesh1', 'geom1');
model.physics.create('spf', 'LaminarFlow', 'geom1');

model.study.create('std1');
model.study('std1').feature.create('stat', 'Stationary');
```

```
model.param.set('p_in', '10[Pa]');
model.param.set('p_out', '0[Pa]');
model.param.set('L', '2[cm]');
model.param.set('W', '3[mm]');
model.param.set('H', '8[um]');

model.geom('geom1').feature.create('blk1', 'Block');
model.geom('geom1').feature('blk1').setIndex('size', 'W/2', 0);
model.geom('geom1').feature('blk1').setIndex('size', 'L', 1);
model.geom('geom1').feature('blk1').setIndex('size', 'H', 2);
model.geom('geom1').feature('blk1').set('base', 'corner');
model.geom('geom1').run('blk1');
model.geom('geom1').run;

model.param.set('eta', '1e-3[Pa*s]');

model.physics('spf').feature.create('inl1', 'Inlet', 2);
model.physics('spf').feature.create('out1', 'Outlet', 2);
model.physics('spf').feature.create('sym1', 'SymmetryFluid', 2);
model.physics('spf').feature('sym1').selection.set([6]);
model.physics('spf').feature('inl1').selection.set([2]);
model.physics('spf').feature('out1').selection.set([5]);
model.physics('spf').feature('fp1').set('mu_mat', 1, 'userdef');
model.physics('spf').feature('fp1').set('mu', 1, 'eta');
model.physics('spf').feature('fp1').set('rho_mat', 1, 'userdef');
model.physics('spf').feature('fp1').set('rho', 1, '1e3');
model.physics('spf').prop('CompressibilityProperty').set('Compressibili
ty', 1, 'Incompressible');
model.physics('spf').prop('CompressibilityProperty').set('Compressibili
ty', 1, 'CompressibleMALT03');
model.physics('spf').prop('CompressibilityProperty').set('Compressibili
ty', 1, 'Incompressible');
model.physics('spf').feature('inl1').set('BoundaryCondition', 1,
'PressureNoViscousStress');
model.physics('spf').feature('inl1').set('p0', 1, 'p_in');
model.physics('spf').feature('out1').set('p0', 1, 'p_out');

model.mesh('mesh1').feature.create('ftet1', 'FreeTet');
model.mesh('mesh1').run('ftet1');
model.mesh('mesh1').feature('ftet1').set('zscale', '10');
model.mesh('mesh1').run('ftet1');
model.mesh('mesh1').feature('ftet1').set('zscale', '3');
model.mesh('mesh1').run('ftet1');
model.mesh('mesh1').feature('ftet1').set('zscale', '5');
model.mesh('mesh1').run('ftet1');
model.mesh('mesh1').feature('ftet1').set('zscale', '2');
model.mesh('mesh1').run('ftet1');

model.sol.create('sol1');
model.sol('sol1').feature.create('st1', 'StudyStep');
model.sol('sol1').feature('st1').set('study', 'std1');
model.sol('sol1').feature('st1').set('studystep', 'stat');
model.sol('sol1').feature.create('v1', 'Variables');
model.sol('sol1').feature.create('s1', 'Stationary');
model.sol('sol1').feature('s1').feature.create('fc1', 'FullyCoupled');
model.sol('sol1').feature('s1').feature('fc1').set('dtech', 'const');
```

```
model.sol('sol1').feature('s1').feature('fc1').set('damp', 0.9);
model.sol('sol1').feature('s1').feature('fc1').set('maxiter', 100);
model.sol('sol1').feature('s1').feature.create('i1', 'Iterative');
model.sol('sol1').feature('s1').feature('i1').set('linsolver',
'gmres');
model.sol('sol1').feature('s1').feature('i1').set('prefuntype',
'right');
model.sol('sol1').feature('s1').feature('i1').set('itrestart', 50);
model.sol('sol1').feature('s1').feature('i1').set('rhob', 100);
model.sol('sol1').feature('s1').feature('i1').set('maxlinit', 200);
model.sol('sol1').feature('s1').feature('i1').set('nlinnormuse', 'on');
model.sol('sol1').feature('s1').feature('fc1').set('linsolver', 'i1');
model.sol('sol1').feature('s1').feature('i1').feature.create('mg1',
'Multigrid');
model.sol('sol1').feature('s1').feature('i1').feature('mg1').set('prefu
n', 'gmg');
model.sol('sol1').feature('s1').feature('i1').feature('mg1').set('mcase
gen', 'any');
model.sol('sol1').feature('s1').feature('i1').feature('mg1').feature('p
r').feature.create('sl1', 'SORLine');
model.sol('sol1').feature('s1').feature('i1').feature('mg1').feature('p
r').feature('sl1').set('iter', 2);
model.sol('sol1').feature('s1').feature('i1').feature('mg1').feature('p
r').feature('sl1').set('linerelax', 0.3);
model.sol('sol1').feature('s1').feature('i1').feature('mg1').feature('p
r').feature('sl1').set('linealgorithm', 'matrix');
model.sol('sol1').feature('s1').feature('i1').feature('mg1').feature('p
r').feature('sl1').set('linemethodmatrix', 'coupled');
model.sol('sol1').feature('s1').feature('i1').feature('mg1').feature('p
r').feature('sl1').set('linevar', 'mod1_u');
model.sol('sol1').feature('s1').feature('i1').feature('mg1').feature('p
r').feature('sl1').set('seconditer', 2);
model.sol('sol1').feature('s1').feature('i1').feature('mg1').feature('p
r').feature('sl1').set('relax', 0.8);
model.sol('sol1').feature('s1').feature('i1').feature('mg1').feature('p
o').feature.create('sl1', 'SORLine');
model.sol('sol1').feature('s1').feature('i1').feature('mg1').feature('p
o').feature('sl1').set('iter', 2);
model.sol('sol1').feature('s1').feature('i1').feature('mg1').feature('p
o').feature('sl1').set('linerelax', 0.3);
model.sol('sol1').feature('s1').feature('i1').feature('mg1').feature('p
o').feature('sl1').set('linealgorithm', 'matrix');
model.sol('sol1').feature('s1').feature('i1').feature('mg1').feature('p
o').feature('sl1').set('linemethodmatrix', 'coupled');
model.sol('sol1').feature('s1').feature('i1').feature('mg1').feature('p
o').feature('sl1').set('linevar', 'mod1_u');
model.sol('sol1').feature('s1').feature('i1').feature('mg1').feature('p
o').feature('sl1').set('seconditer', 2);
model.sol('sol1').feature('s1').feature('i1').feature('mg1').feature('p
o').feature('sl1').set('relax', 0.8);
model.sol('sol1').feature('s1').feature('i1').feature('mg1').feature('c
s').feature.create('d1', 'Direct');
model.sol('sol1').feature('s1').feature('i1').feature('mg1').feature('c
s').feature('d1').set('linsolver', 'pardiso');
model.sol('sol1').feature('s1').feature('fc1').set('dtech', 'const');
model.sol('sol1').feature('s1').feature('fc1').set('damp', 0.9);
model.sol('sol1').feature('s1').feature('fc1').set('maxiter', 100);
```

```
model.sol('sol1').feature('s1').feature.remove('fcDef');
model.sol('sol1').attach('std1');

model.result.create('pg1', 3);
model.result('pg1').set('data', 'dset1');
model.result('pg1').feature.create('surf1', 'Surface');
model.result.create('pg2', 3);
model.result('pg2').set('data', 'dset1');
model.result('pg2').feature.create('slc1', 'Slice');

model.sol('sol1').runAll;

model.result('pg1').run;
model.result('pg1').feature('surf1').run;
model.result('pg1').set('renderdatacached', true);
model.result('pg2').feature('slc1').run;
model.result('pg2').feature('slc1').set('quickplane', 'zx');
model.result('pg2').feature('slc1').set('quickynumber', '1');
model.result('pg2').feature('slc1').run;

model.mesh('mesh1').feature.remove('ftet1');
model.mesh('mesh1').feature.create('dis1', 'Distribution');
model.mesh('mesh1').feature.create('map1', 'Map');
model.mesh('mesh1').feature.remove('dis1');
model.mesh('mesh1').feature('map1').selection.set([2]);
model.mesh('mesh1').feature('map1').feature.create('dis1',
'Distribution');
model.mesh('mesh1').feature('map1').feature.create('dis2',
'Distribution');
model.mesh('mesh1').feature('map1').feature('dis1').selection.set([5]);
model.mesh('mesh1').feature('map1').feature('dis2').selection.set([9]);
model.mesh('mesh1').feature('map1').feature('dis2').set('numelem',
'3');
model.mesh('mesh1').feature.create('swe1', 'Sweep');
model.mesh('mesh1').run;

model.sol('sol1').feature.remove('s1');
model.sol('sol1').feature.remove('v1');
model.sol('sol1').feature.remove('st1');
model.sol('sol1').feature.create('st1', 'StudyStep');
model.sol('sol1').feature('st1').set('study', 'std1');
model.sol('sol1').feature('st1').set('studystep', 'stat');
model.sol('sol1').feature.create('v1', 'Variables');
model.sol('sol1').feature.create('s1', 'Stationary');
model.sol('sol1').feature('s1').feature.create('fc1', 'FullyCoupled');
model.sol('sol1').feature('s1').feature('fc1').set('dtech', 'const');
model.sol('sol1').feature('s1').feature('fc1').set('damp', 0.9);
model.sol('sol1').feature('s1').feature('fc1').set('maxiter', 100);
model.sol('sol1').feature('s1').feature.create('i1', 'Iterative');
model.sol('sol1').feature('s1').feature('i1').set('linsolver',
'gmres');
model.sol('sol1').feature('s1').feature('i1').set('prefuntype',
'right');
model.sol('sol1').feature('s1').feature('i1').set('itrestart', 50);
model.sol('sol1').feature('s1').feature('i1').set('rhob', 100);
model.sol('sol1').feature('s1').feature('i1').set('maxlinit', 200);
```

```
model.sol('sol1').feature('s1').feature('i1').set('nlinnormuse', 'on');
model.sol('sol1').feature('s1').feature('fc1').set('linsolver', 'i1');
model.sol('sol1').feature('s1').feature('i1').feature.create('mg1',
'Multigrid');
model.sol('sol1').feature('s1').feature('i1').feature('mg1').set('prefu
n', 'gmg');
model.sol('sol1').feature('s1').feature('i1').feature('mg1').set('mcase
gen', 'any');
model.sol('sol1').feature('s1').feature('i1').feature('mg1').feature('p
r').feature.create('sl1', 'SORLine');
model.sol('sol1').feature('s1').feature('i1').feature('mg1').feature('p
r').feature('sl1').set('iter', 2);
model.sol('sol1').feature('s1').feature('i1').feature('mg1').feature('p
r').feature('sl1').set('linerelax', 0.3);
model.sol('sol1').feature('s1').feature('i1').feature('mg1').feature('p
r').feature('sl1').set('linealgorithm', 'matrix');
model.sol('sol1').feature('s1').feature('i1').feature('mg1').feature('p
r').feature('sl1').set('linemethodmatrix', 'coupled');
model.sol('sol1').feature('s1').feature('i1').feature('mg1').feature('p
r').feature('sl1').set('linevar', 'mod1_u');
model.sol('sol1').feature('s1').feature('i1').feature('mg1').feature('p
r').feature('sl1').set('seconditer', 2);
model.sol('sol1').feature('s1').feature('i1').feature('mg1').feature('p
r').feature('sl1').set('relax', 0.8);
model.sol('sol1').feature('s1').feature('i1').feature('mg1').feature('p
o').feature.create('sl1', 'SORLine');
model.sol('sol1').feature('s1').feature('i1').feature('mg1').feature('p
o').feature('sl1').set('iter', 2);
model.sol('sol1').feature('s1').feature('i1').feature('mg1').feature('p
o').feature('sl1').set('linerelax', 0.3);
model.sol('sol1').feature('s1').feature('i1').feature('mg1').feature('p
o').feature('sl1').set('linealgorithm', 'matrix');
model.sol('sol1').feature('s1').feature('i1').feature('mg1').feature('p
o').feature('sl1').set('linemethodmatrix', 'coupled');
model.sol('sol1').feature('s1').feature('i1').feature('mg1').feature('p
o').feature('sl1').set('linevar', 'mod1_u');
model.sol('sol1').feature('s1').feature('i1').feature('mg1').feature('p
o').feature('sl1').set('seconditer', 2);
model.sol('sol1').feature('s1').feature('i1').feature('mg1').feature('p
o').feature('sl1').set('relax', 0.8);
model.sol('sol1').feature('s1').feature('i1').feature('mg1').feature('c
s').feature.create('d1', 'Direct');
model.sol('sol1').feature('s1').feature('i1').feature('mg1').feature('c
s').feature('d1').set('linsolver', 'pardiso');
model.sol('sol1').feature('s1').feature('fc1').set('dtech', 'const');
model.sol('sol1').feature('s1').feature('fc1').set('damp', 0.9);
model.sol('sol1').feature('s1').feature('fc1').set('maxiter', 100);
model.sol('sol1').feature('s1').feature.remove('fcDef');
model.sol('sol1').attach('std1');
model.sol('sol1').runAll;

model.result('pg1').run;
model.result('pg2').feature('slc1').run;
model.result('pg1').feature('surf1').run;

out = model;
```

2. Velocity Profile

MATLAB is also used for a velocity profile as shown in Figure B-5. The fluidic inside a rectangular channel is modeled in COMSOL and a series of velocities along the thickness direction are extracted and mathematically fitted.

File: `VelocityProfile.m`

```
% To study the velocity profile along the thickness direction.
clear
clc

% Call the COMSOL model.
COMSOL_MATLAB_example;
model=ModelUtil.model('Model');


W = 1e-3;
L = 1e-2;
H = 10e-6;


n = 11;

% Assign the coordinates for the (n = 11) locations.
co = zeros(3,11);
co(1,1:11) = W/2;
co(2,1:11) = L/2;

for i = 1:n
    co(3,i) = (i-1)*H/(n-1);
end

% Extract the velocities on (n = 11) locations.
vel = mphinterp(model,'v','coord',co(:,1:11));

% H = 10um; units: length - um, velocity - um/s.
s = fitoptions('Method','NonlinearLeastSquare');
f = fittype('a1*x*(10-x)','options',s);

% Fit the velocities with parabolic equation defined in "f".
c = fit(z'*1e6,vel'*1e6,f)


figure(1)
hold on
plot(vel,z,'s')
plot(vel_fit,z2*1e-6,'Linewidth',1)
hold off
xlim([0 14e-6])
ylim([0 10e-6])
set(gca,'ytick',0:1e-6:10e-6)
set(gca,'yticklabel',{'0','1','2','3','4','5','6','7','8','9','10'})
xlabel('Velocity [m/s]','Fontsize',12);
ylabel('Height [\mum]','Fontsize',12);
```

Appendix C Fabrication

C.1 Fabrication Process Flow

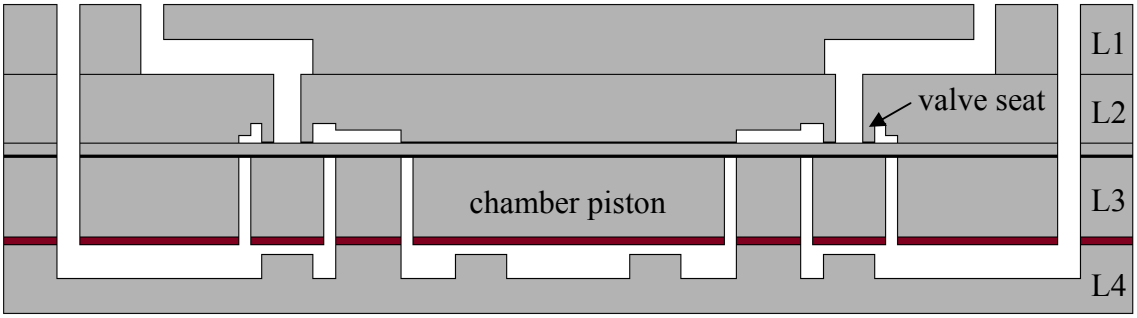

Figure C-1: Cross-section of the micromachined displacement pump (same with Figure 3-1). Gray: silicon; black: buried oxide layer; dark red: thermal oxide.

The details of the fabrication processes of the four layers and the assembly are illustrated in this section. The major steps have been shown in Chapter 3 with schematic drawings of the cross-sections.

Layer 1

Step	Description
Starting Materials	Double side polished (DSP) silicon wafer
1. Clean	RCA clean
2. Oxidation	Wet oxidation at 1000^{o}C for 90 minutes (~0.5μm thick)
3. Lithography	Spin cast thin resist* on both surfaces. Pattern with Mask AM (alignment marks) on the top side, and then pattern with Mask AM on the bottom side, by aligning to the top side marks.
4. BOE	Etch exposed oxide around the alignment marks to silicon.
5. RIE	RIE on both sides by 0.5~1μm for the alignment marks.
6. Strip resist	Wet cleaning**.

Step	Description
7. Lithography	Spin cast thick resist on both surfaces. Pattern with Mask 1-1 on top surface, with Mask 1-2 on bottom surface.
8. BOE	Etch exposed oxide for the through holes and trenches.
9. Etch through holes	DRIE on the top surface half way through the wafer.
10. Etch trenches	Mount the top side to a quartz wafer. DRIE on the bottom surface half way through the wafer. The holes should be through.
11. Strip resist	Remove polymer coating from DRIE process with oxygen plasma*** for >30 minutes, followed by wet cleaning.

* "Thin resist" used in the fabrication refers to the resist OCG825, which is about 1μm thick. "Thick resist" shown later refers to the resist AZ4620, which is about 8~10μm thick.

** We use piranha clean. Piranha solution is a mixture of sulfuric acid (H_2SO_4) and hydrogen peroxide (H_2O_2). The mixture we use is 3:1 concentrated sulfuric acid to 30% hydrogen peroxide solution.

*** The tool is also known as "asher".

Layer 2

Step	Description
Starting Materials	Double side polished (DSP) silicon wafer
1. Clean	RCA clean
2. Oxidation	Wet oxidation at 1000^{o}C for 90 minutes (~0.5μm thick)
3. Lithography	Spin cast thin resist on both side surfaces. Pattern with Mask AM on the top side, and then pattern with Mask AM on the bottom side, by aligning to the top side marks.
4. BOE	Etch exposed oxide around the alignment marks to silicon.
5. RIE	RIE on both sides by 0.5~1μm for the alignment marks.

Step	Description
6. Strip resist	Wet cleaning.
7. Lithography	Spin cast thin resist on both surfaces. Pattern with Mask 2-1 on bottom to expose the area of the chambers, valves, channels between chambers and valves, and through holes.
8. BOE	Etch exposed oxide to silicon.
9. Roughening	Shallow etch with SF6 plasma for 3 seconds. The shallow etch step is used to roughen the exposed surface area to prevent accidental bonding.
10. Strip and clean	Wet cleaning.
11. Lithography	Spin cast thin resist on bottom surface. Pattern with Mask 2-2 to expose the surroundings of the valve seats.
12. Etch	Etch with SF6 plasma for 8 seconds (~0.5μm) to offset the valve seats from the rest area of the valves.
13. Strip and clean	Wet cleaning.
14. Oxide deposition	Deposit ~0.5μm thick oxide on the bottom surface (PECVD).
15. Lithography	Spin cast thick resist on the bottom surface. Pattern with Mask 2-3 to expose the channel area. The oxide will be used as the etch mask in Step 17.
16. BOE	Etch the exposed oxide to silicon.
17. Strip and clean	Wet cleaning.
18. Lithography	Spin cast thick resist on the bottom surface. Pattern with Mask 2-4 to expose the through holes.
19. DRIE	DRIE the through holes. The through holes include the holes connecting the pumps to outside and the holes for pneumatic actuations.
20. Strip and clean	Remove polymer coating from DRIE process with oxygen plasma for >30 minutes, followed by wet cleaning.

Step	Description
21. Etch channels	Mount the top side to a quartz wafer. DRIE using the oxide mask formed during Steps 14~17. The channel depth is ~10μm.
22. Strip and clean	Remove polymer coating from DRIE process with oxygen plasma for >30 minutes, followed by wet cleaning.

Layer 3

Step	Description
Starting Materials	Silicon-on-insulator wafer, with a 10 μm thick device layer.
1. Clean	RCA clean
2. Oxidation	Wet oxidation at 1000^{o}C for 90 minutes (~0.5μm thick)
3. Nitride deposition	LPCVD ~0.1μm nitride.
4. Lithography	Spin cast thin resist on both side surfaces. Pattern with Mask AM on the top side, and then pattern with Mask AM on the bottom side, by aligning to the top side marks.
5. Nitride removal	RIE etch to completely remove exposed nitride with SF6+C4F8 plasma on both sides.
6. BOE	Etch exposed oxide around the alignment marks to silicon.
7. RIE	RIE on both sides by 0.5~1μm for the alignment marks.
8. Strip resist	Wet cleaning.
9. Nitride removal	RIE etch to completely remove the top side nitride with SF6+C4F8 plasma.
10. Lithography	Spin cast thick resist on top and bottom surfaces. Pattern with Mask 3-1 to expose the through holes. Pattern with Mask 3-2 to expose tether regions and through holes.

Step	Description
11. Nitride removal	RIE etch to completely remove the bottom nitride with SF6+C4F8 plasma.
12. BOE	Etch exposed oxide, on top and bottom surfaces.
13. DRIE	Etch device layer from the top for ~5 minutes to the buried oxide (BOX) layer.
14. BOE	Etch exposed oxide on BOX layer.
15. DRIE	Etch the through holes half way through the wafer from the top.
16. DRIE	Etch the tether regions and the through holes. Careful operation is needed to form the tether fillets. The through holes should be through the wafer.
17. Strip and clean	Remove polymer coating from DRIE process with oxygen plasma for >30 minutes, followed by wet cleaning.

Layer 4

Step	Description
Starting Materials	Double side polished (DSP) silicon wafer
1. Clean	RCA clean
2. Oxidation	Wet oxidation at 1000^{o}C for 90 minutes (~0.5μm thick)
3. Lithography	Spin cast thin resist on both side surfaces. Pattern with Mask AM on the top side, and then pattern with Mask AM on the bottom side, by aligning to the top side marks.
4. BOE	Etch exposed oxide around the alignment marks to silicon.
5. RIE	RIE on both sides by 0.5~1μm for the alignment marks.
6. Strip resist	Wet cleaning.
7. Lithography	Spin cast thin resist on top surface. Pattern with Mask 4-1 to expose the chambers, valves, and channels.

Step	Description
8. BOE	Etch exposed oxide to silicon.
9. Strip and clean	Wet cleaning.
10. Lithography	Spin cast thick resist on top surface. Pattern with Mask 4-2 to expose the actuation cavities.
11. DRIE	Etch >150μm down from the top for the actuation cavities.
12. Strip and clean	Remove polymer coating from DRIE process with oxygen plasma for >30 minutes, followed by wet cleaning.
13. DRIE	Etch the deflection stops with the oxide mask left after Steps 7~9.
14. Strip and clean	Remove polymer coating from DRIE process with oxygen plasma for >30 minutes, followed by wet cleaning.

Assembly

Step	Description
Start	Four individual wafers fabricated.
1. Clean	Wet cleaning (piranha clean).
2. Oxide removal	Strip oxide on all the exposed surfaces with diluted hydrofluoric acid.
3. Nitride removal	Strip the nitride on Layer 3 with hot phosphoric acid.
4. Bonding	Fusion bonding with all four layers. Anneal the wafer stack at 1000^{o}C for 1 hour.
5. Dicing	Dice the 6" bonded wafer into test chips by using multi-cut mode due to the thickness of the wafer stack.

C.2 Photolithography Masks

There are 10 photolithography masks used in total during the fabrication. The mask drawings for the test chip with a single-stage pump and a single valve are shown in Figure C-2 to Figure C-5.

Layer 1 (2 masks)

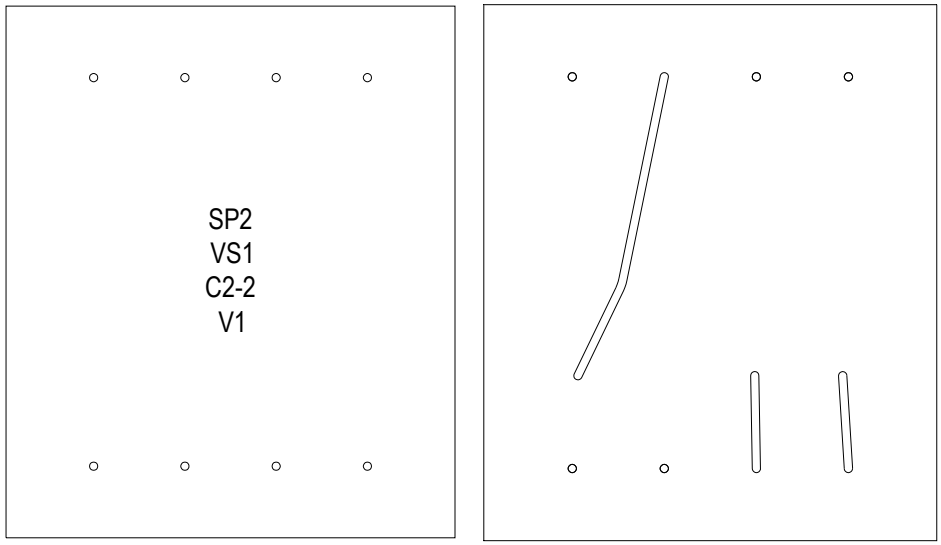

(a) (b)

Figure C-2: Masks for the Layer 1 fabrication. (a) Mask 1-1; (b) Mask 1-2.

Layer 2 (4 masks)

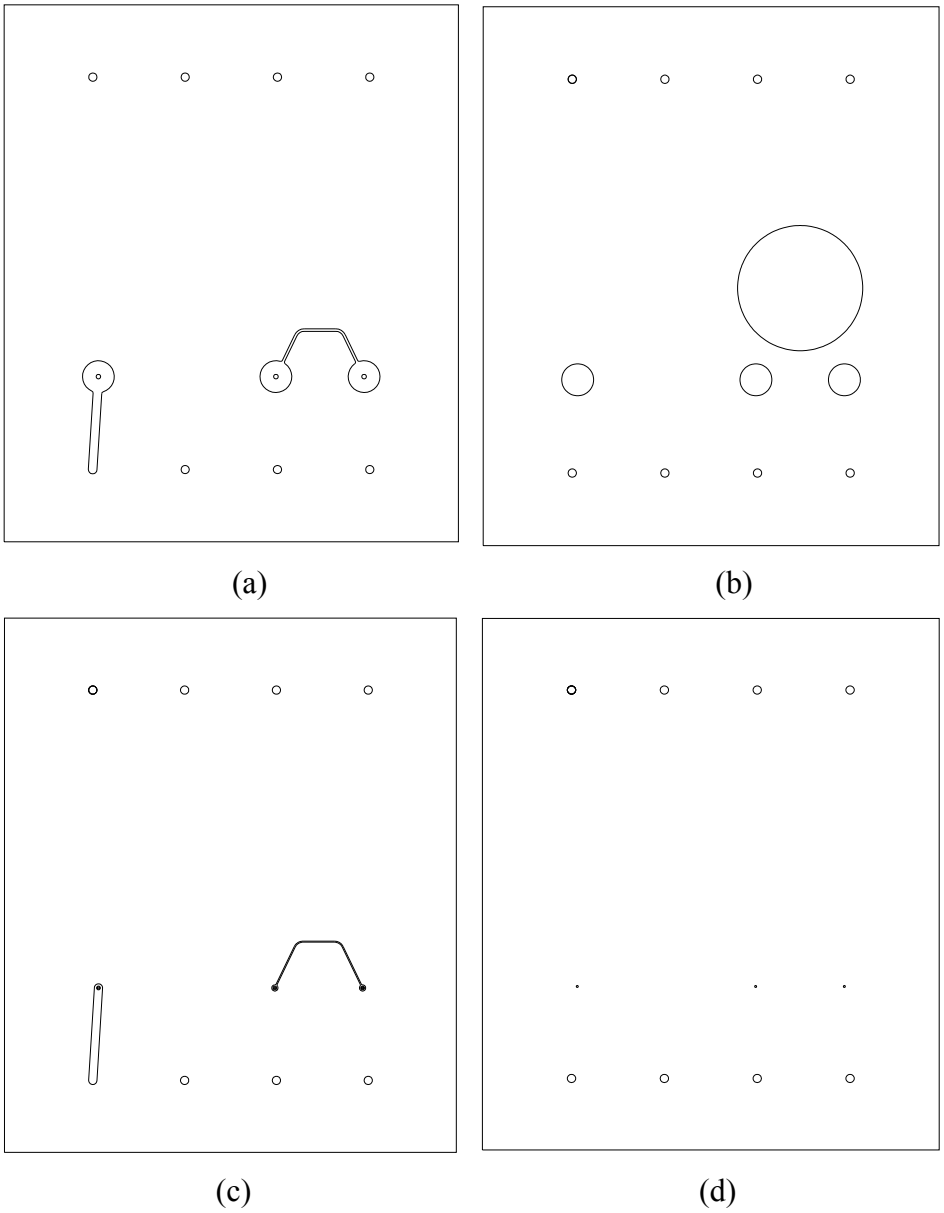

Figure C-3: Masks for the Layer 2 fabrication. (a) Mask 2-1; (b) Mask 2-2; (c) Mask 2-3; (d) Mask 2-4.

Layer 3 (2 masks)

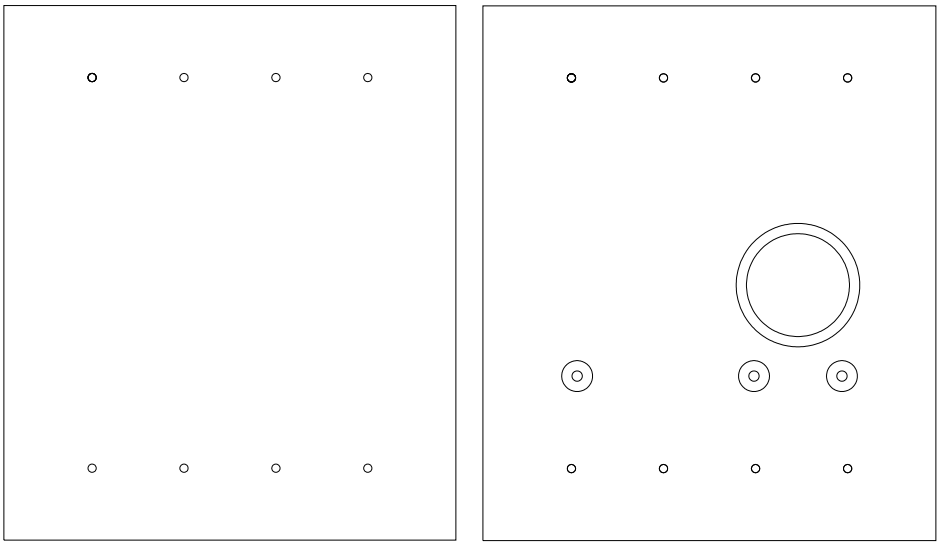

(a) (b)

Figure C-4: Masks for the Layer 3 fabrication. (a) Mask 3-1; (b) Mask 3-2.

Layer 4 (2 masks)

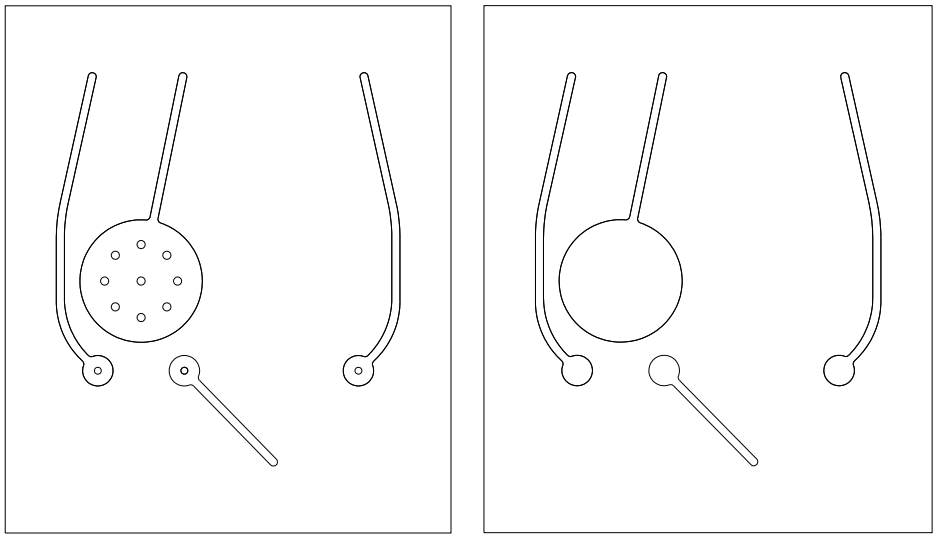

(a) (b)

Figure C-5: Masks for the Layer 4 fabrication. (a) Mask 4-1; (b) Mask 4-2.

The drawings of the masks for the 6" wafer are shown in the following 11 figures.

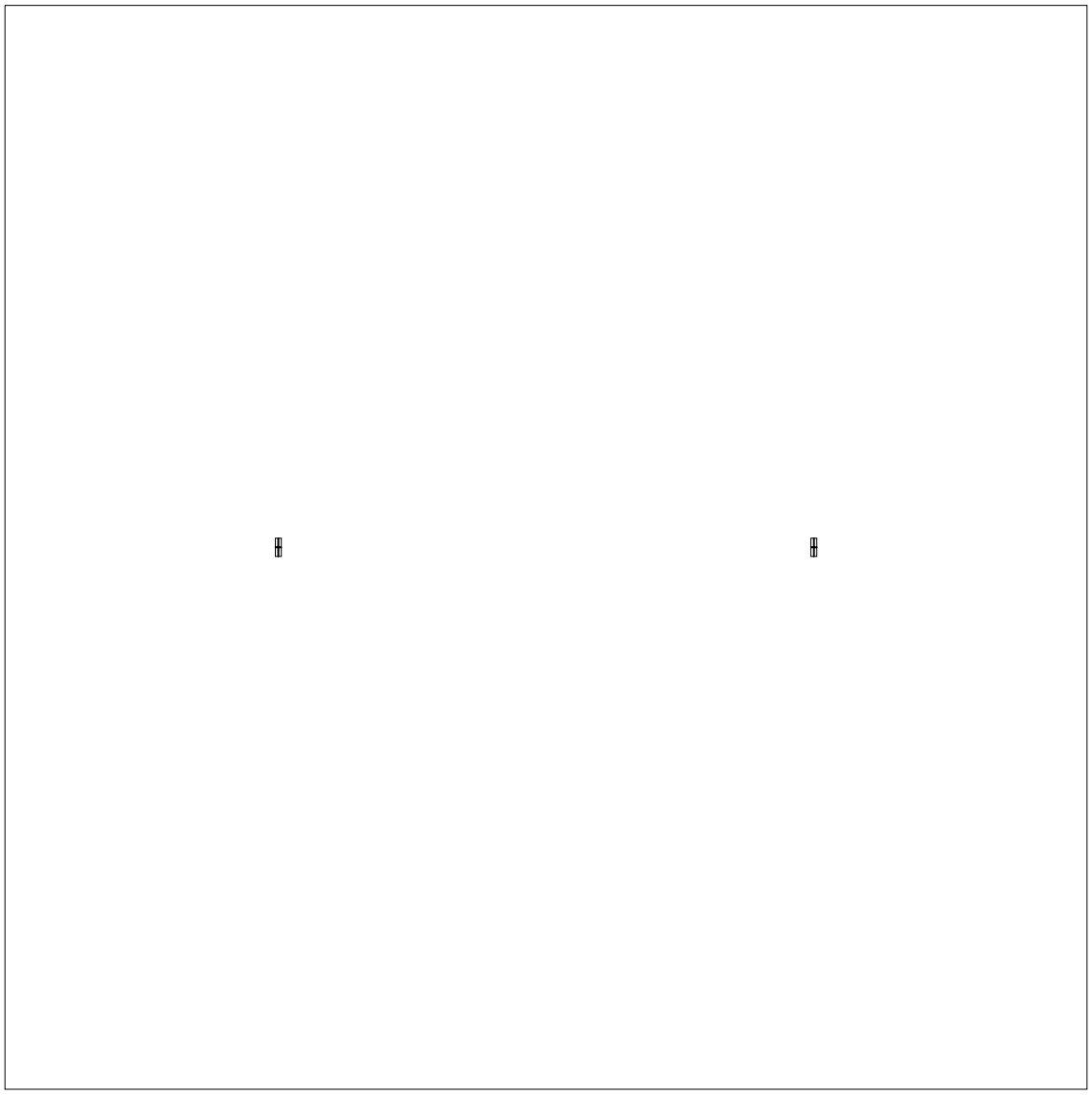

Figure C-6: Mask AM (alignment marks).

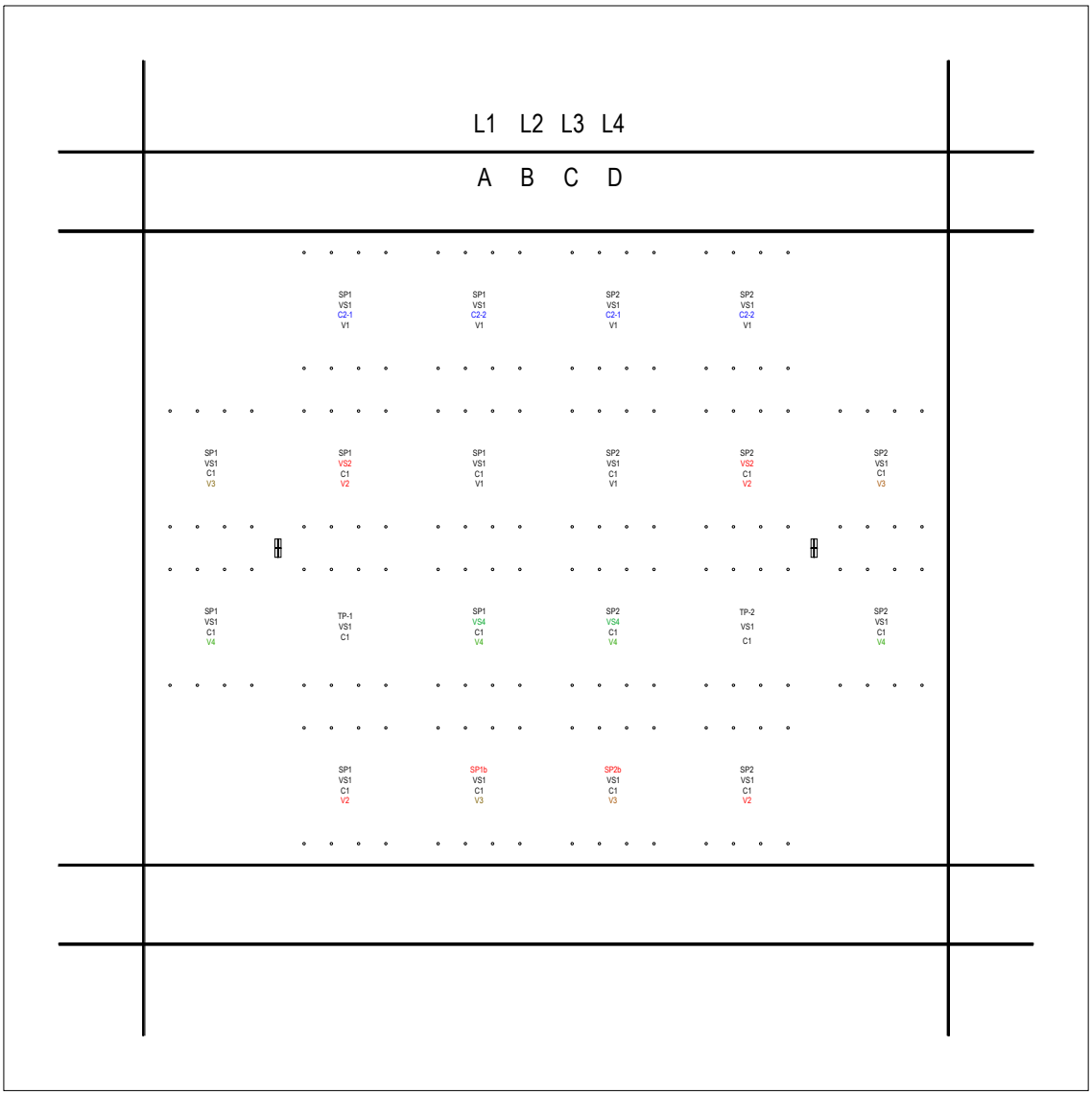

Figure C-7: Mask 1-1.

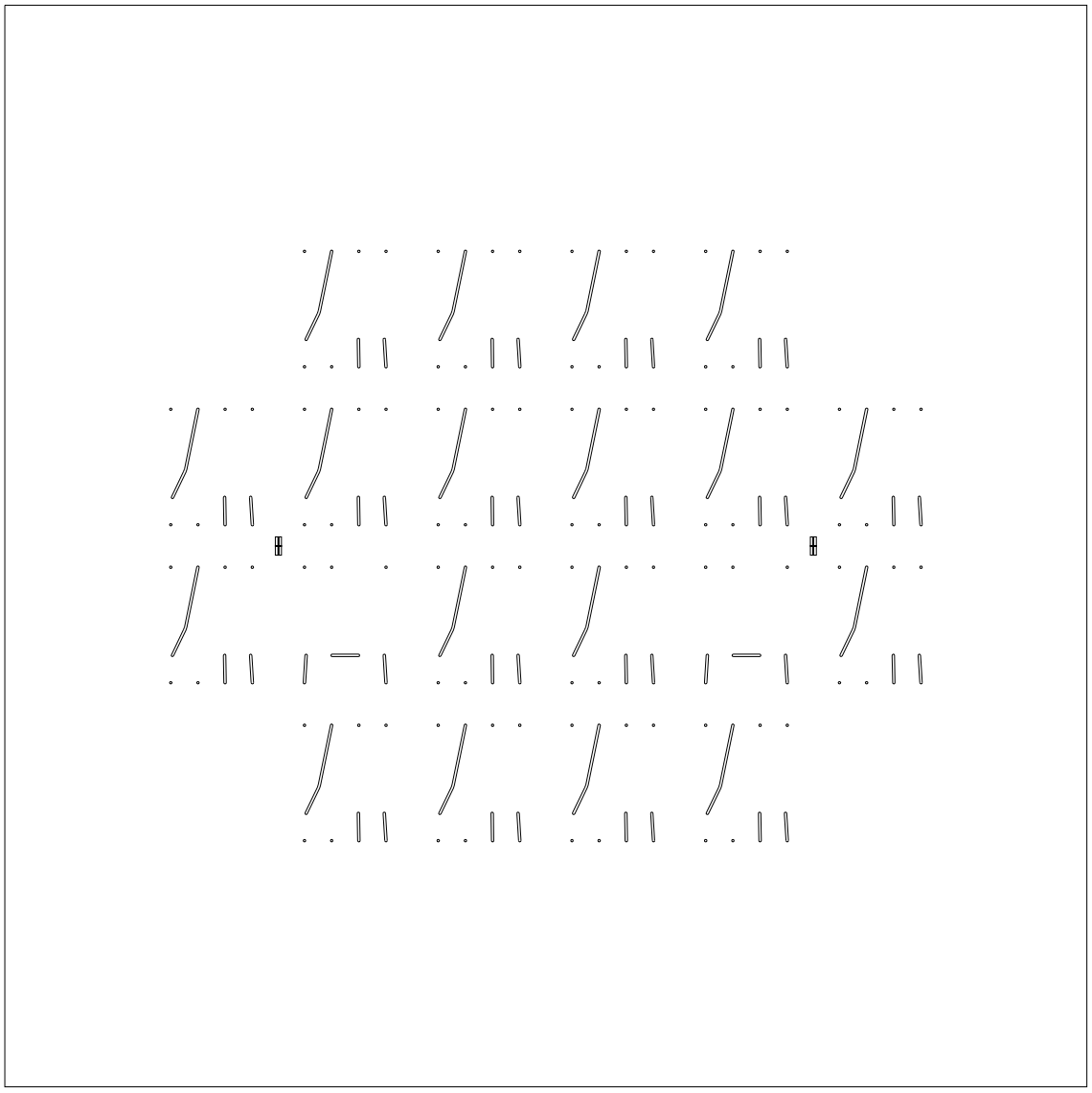

Figure C-8: Mask 1-2.

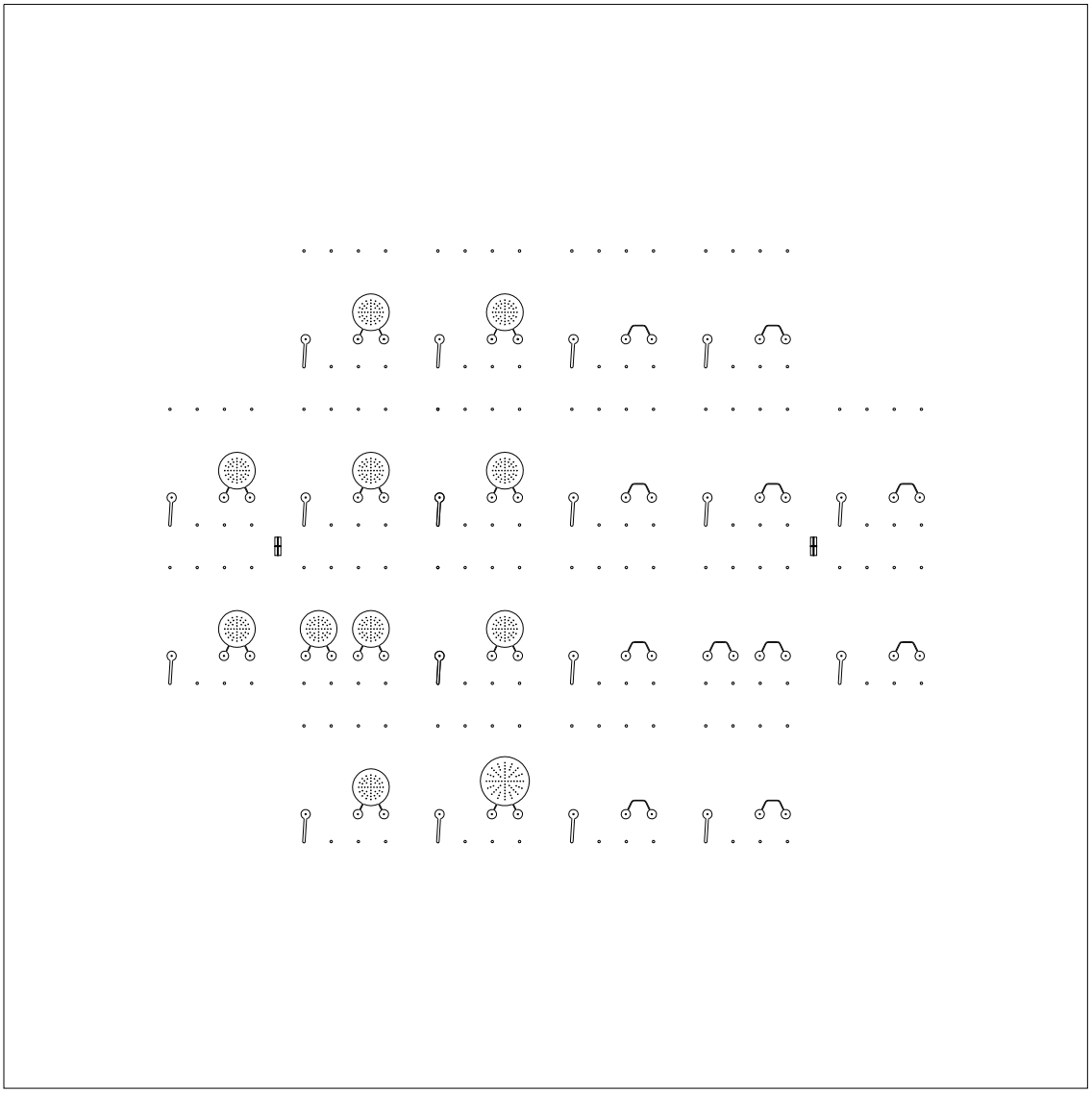

Figure C-9: Mask 2-1.

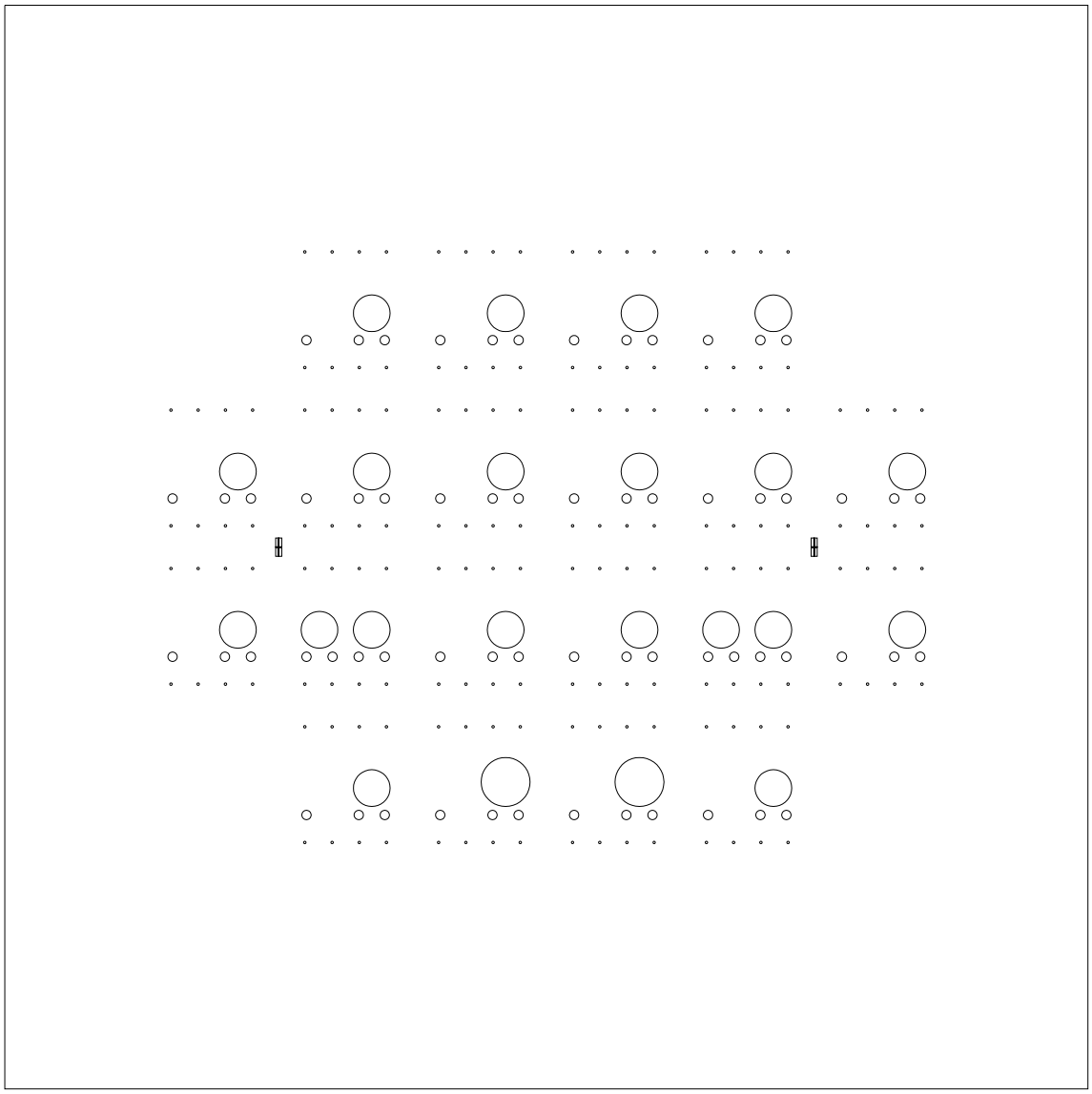

Figure C-10: Mask 2-2.

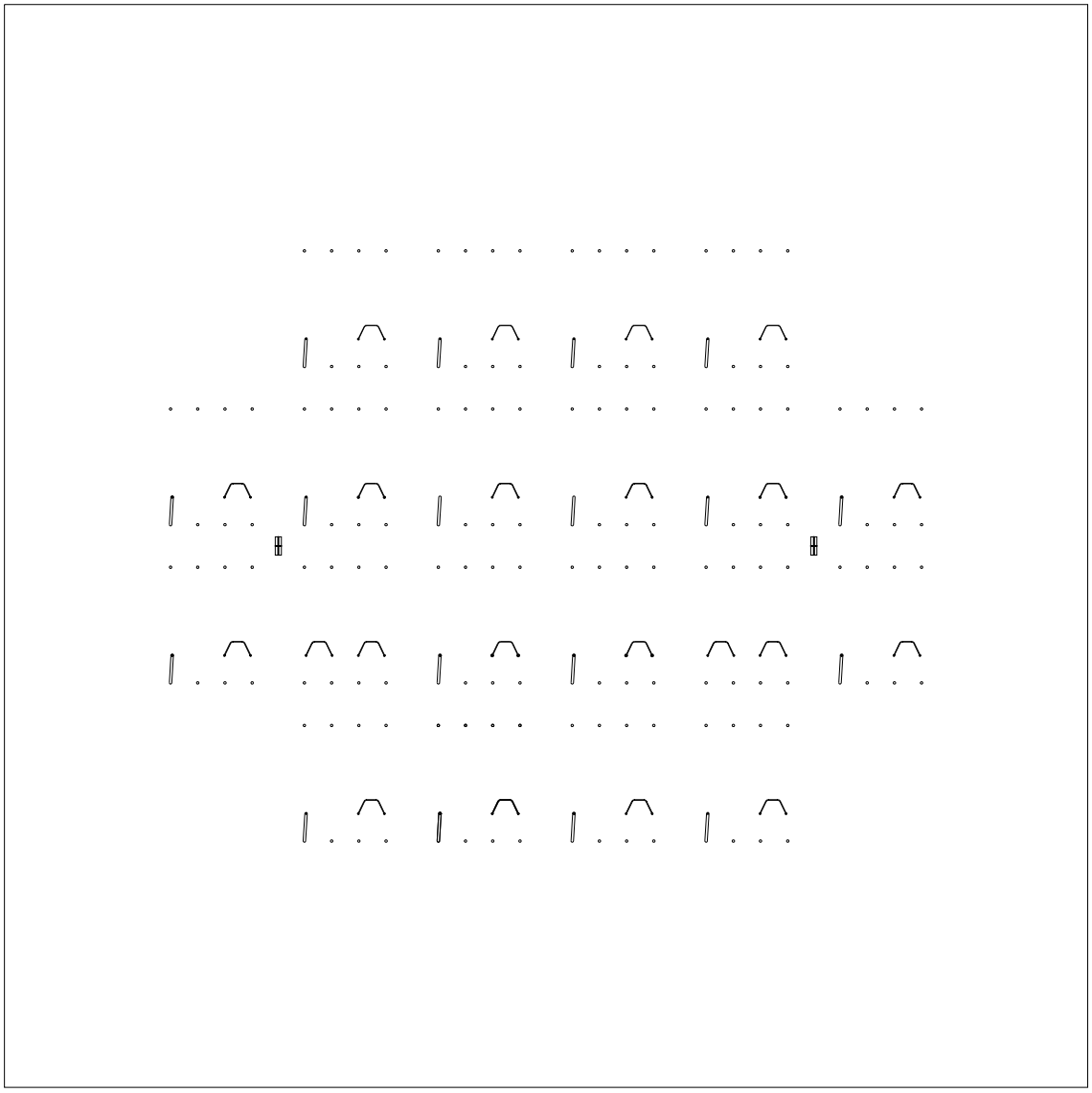

Figure C-11: Mask 2-3.

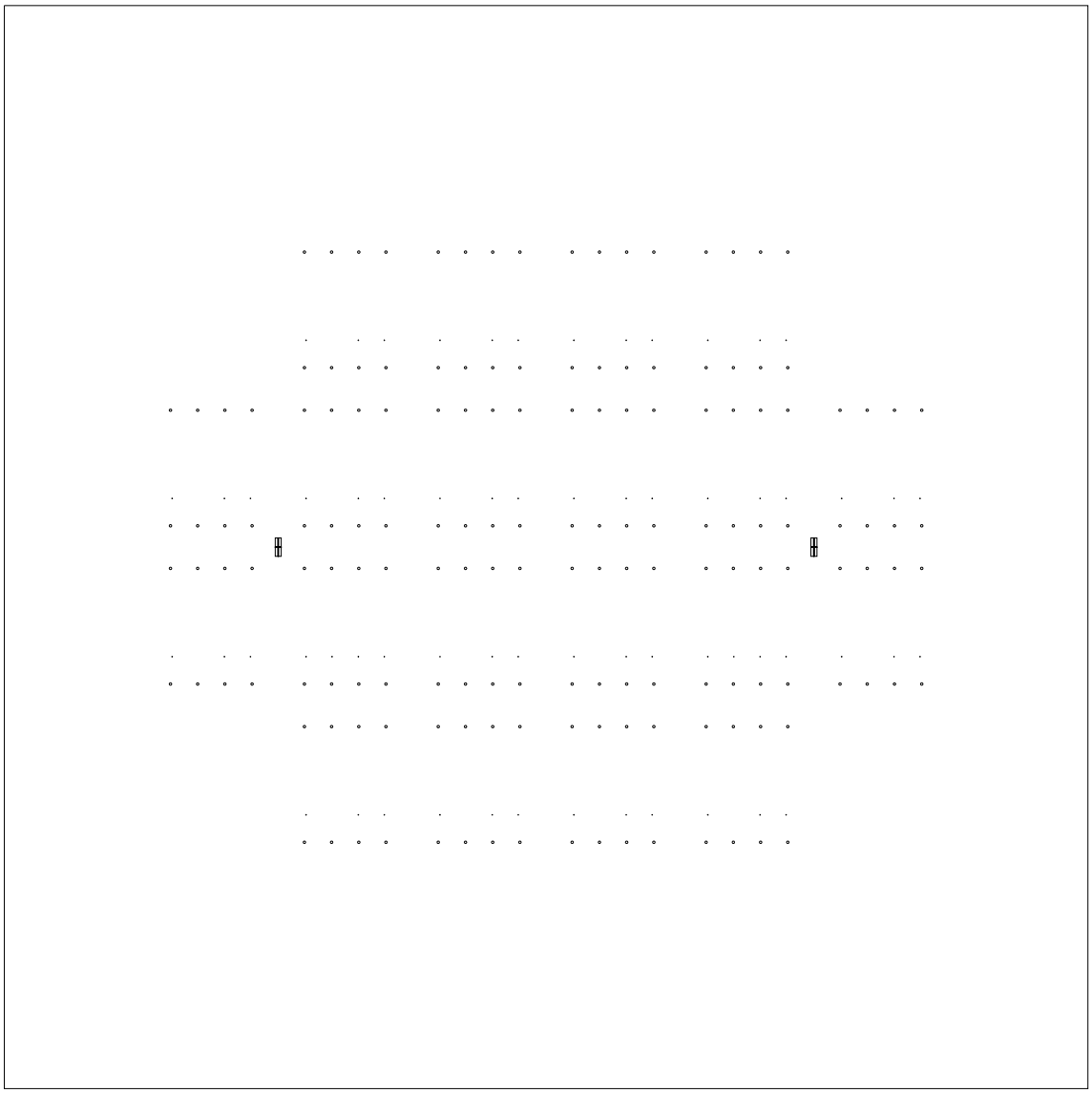

Figure C-12: Mask 2-4.

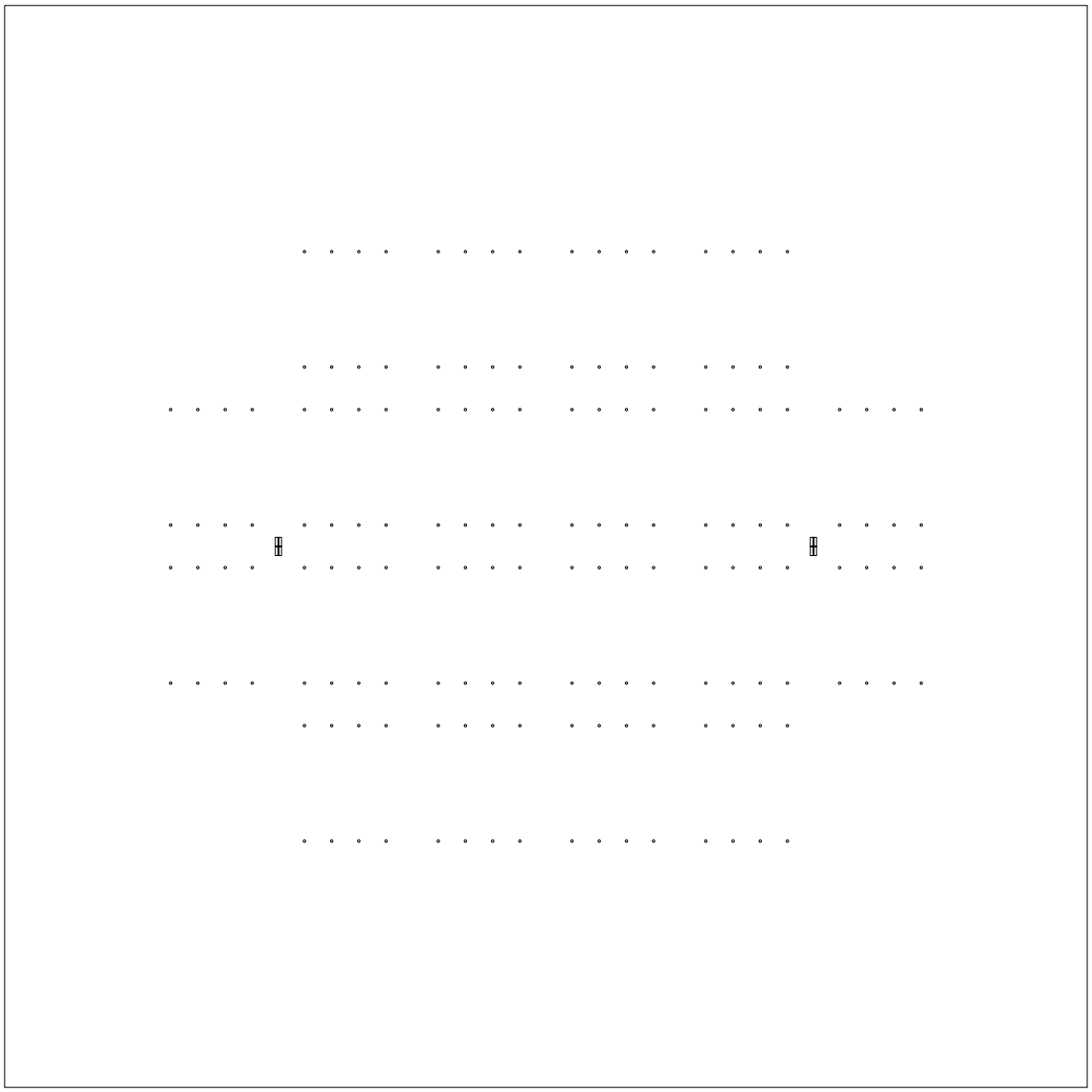

Figure C-13: Mask 3-1.

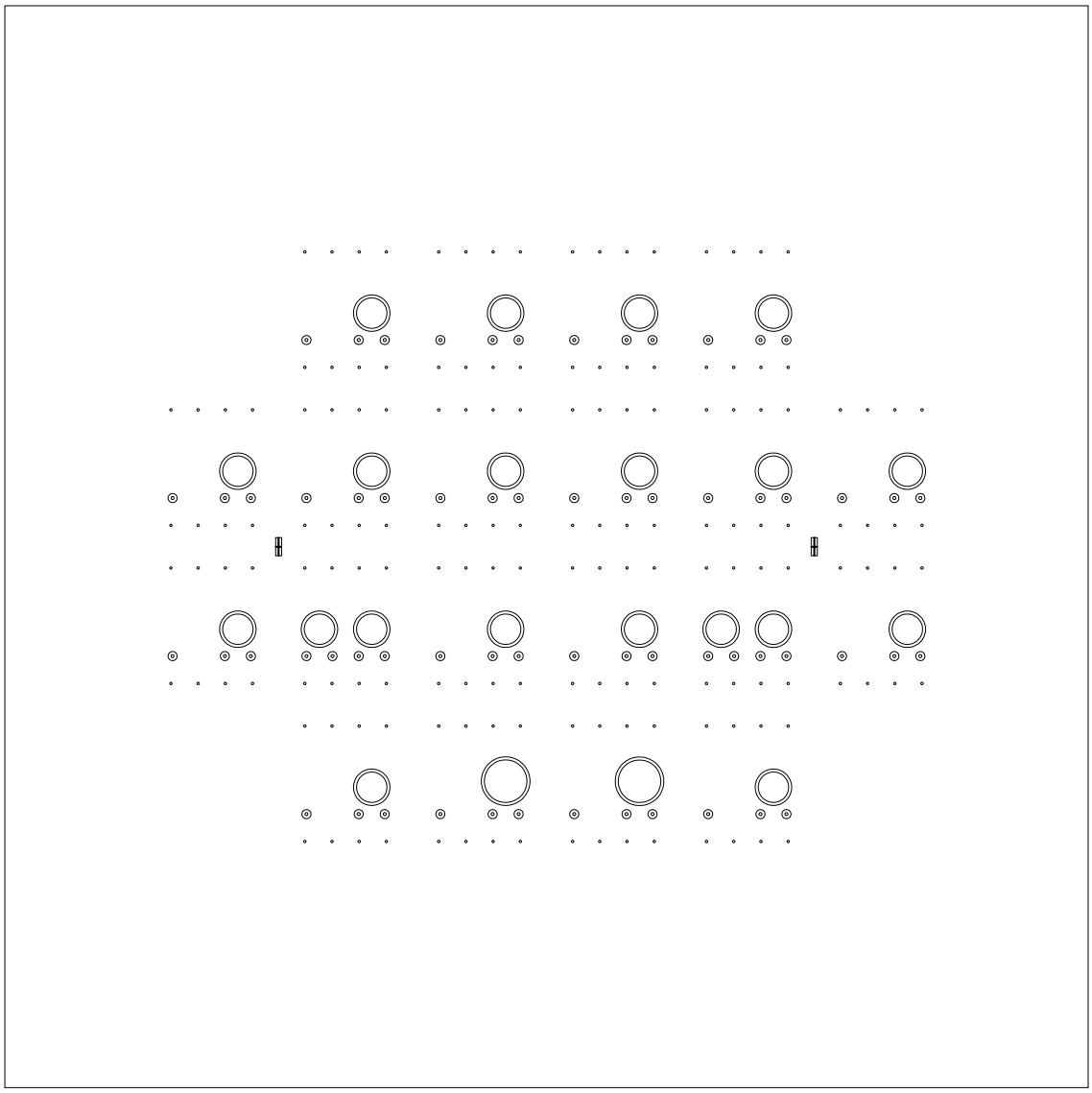

Figure C-14: Mask 3-2.

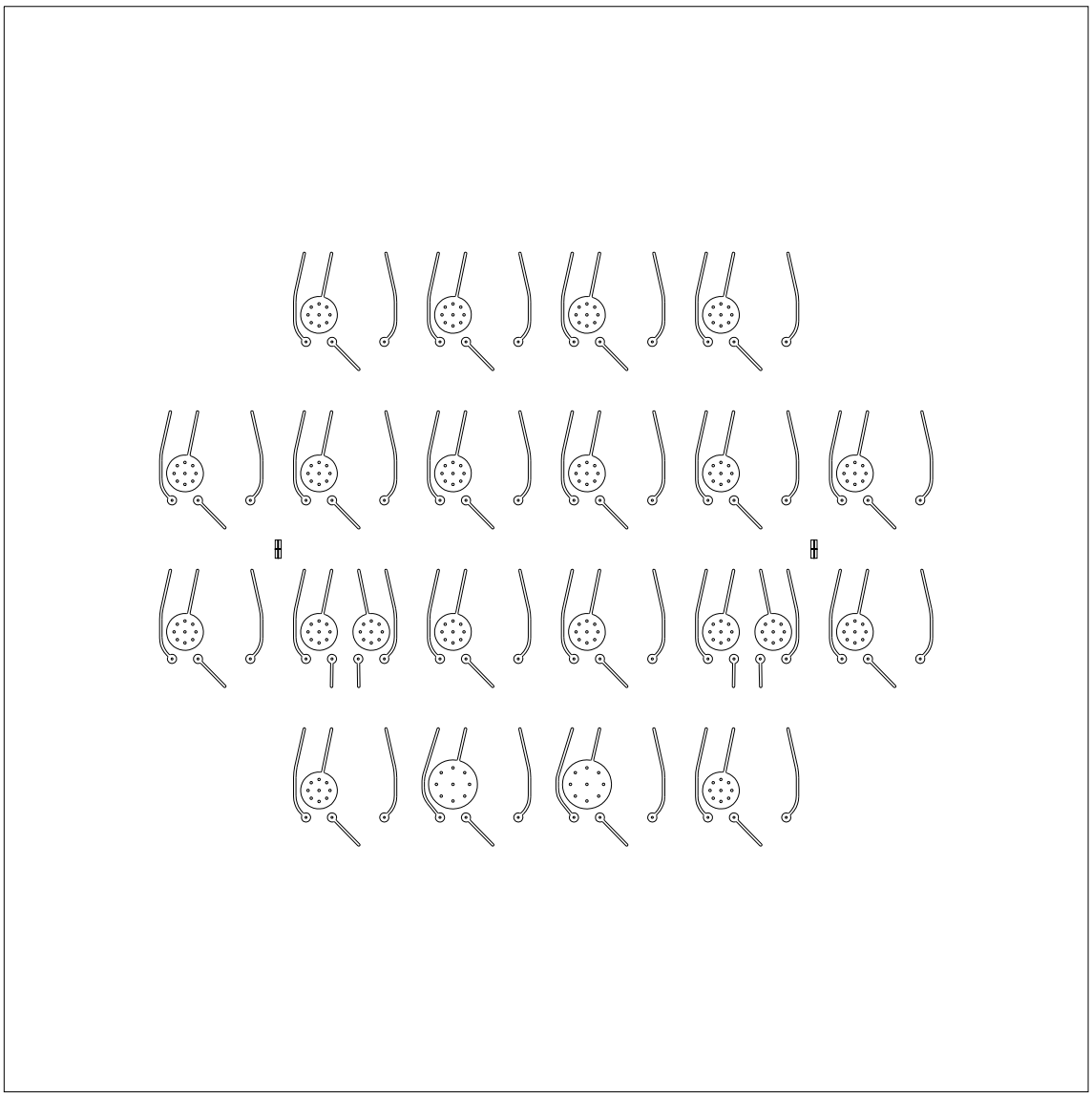

Figure C-15: Mask 4-1.

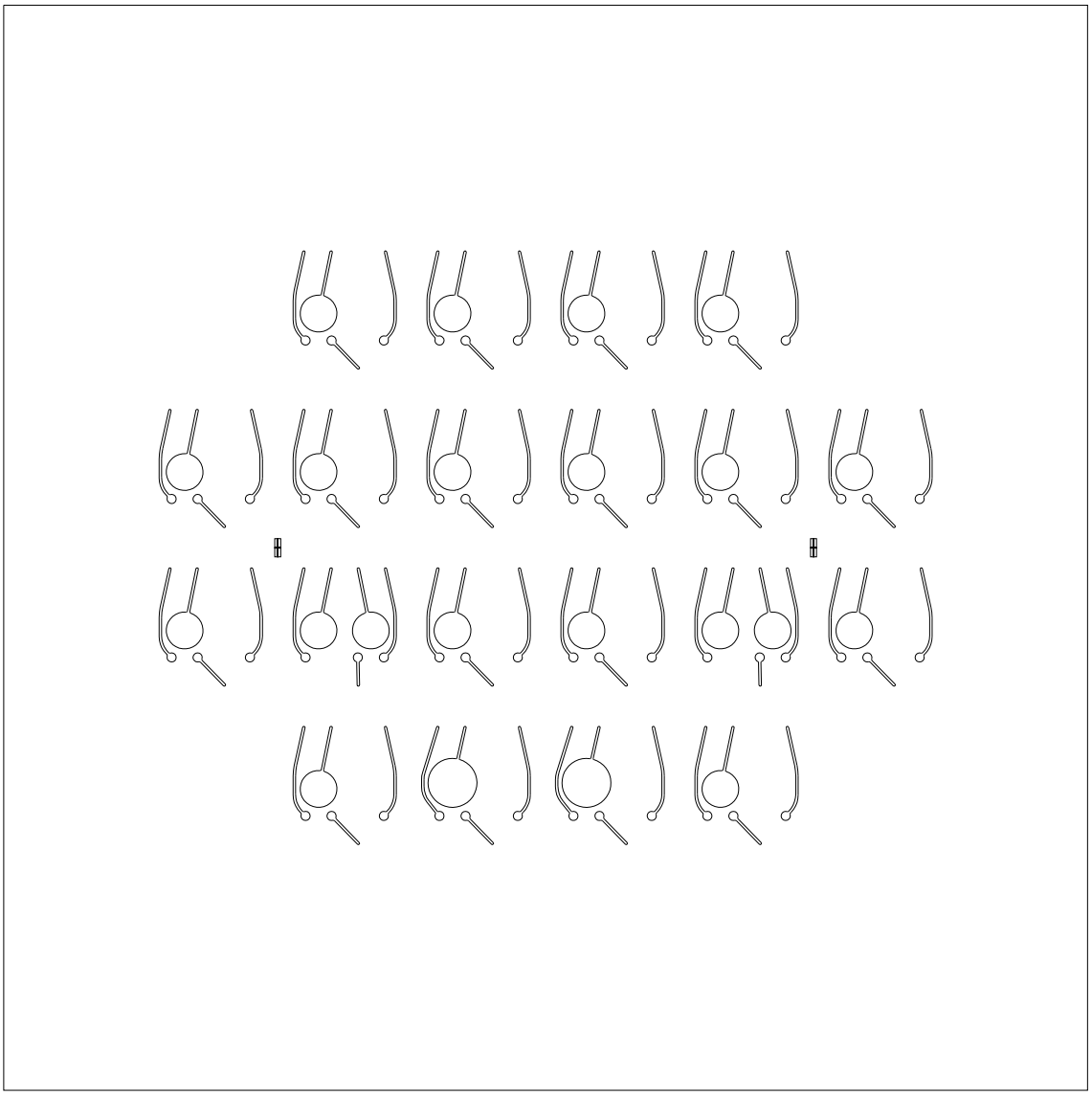

Figure C-16: Mask 4-2.

C.3 DRIE Recipes

The recipes are particular for the Surface Technology System DRIE tool, with the machine name "STS3", in Microsystems Technology Laboratories at MIT. There are four recipes used for the fabrication of the micromachined displacement pumps, with the recipe names on STS3 listed as well. The corresponding steps in Section C.1 related to each recipe are also stated.

Recipe 1 (shallow etch)

Name:

ALMARK

Application:

Layer 1 – Step 5;
Layer 2 – Steps 5, 9, and 12;
Layer 3 – Step 7;
Layer 4 – Step 5.

Gas (single):

SF6, 150 sccm

R.F.:

13.56MHz Generator Connected to Coil: 675W
Platen Generator Connected to 13.56MHz: 29W

Recipe 2 (nitride etch)

Name:

NITRIDE

Application:

Layer 3 – Steps 5, 9, and 11.

Gas (mixture):

SF6, 130 sccm and C4F8, 120 sccm

R.F.:

13.56MHz Generator Connected to Coil: 800W
Platen Generator Connected to 13.56MHz: 14W

Recipe 3 (deep etch)

Name:

JBETCH

Application:

Layer 1 – Steps 9 and 10;
Layer 2 – Steps 19 and 21;
Layer 3 – Steps 13 and 15;
Layer 4 – Steps 11 and 13.

Gas (switching alternatively):

SF6, 105 sccm, for 15 seconds (etch step)
C4F8, 50 sccm, for 11 seconds (passivation step)

R.F.:

13.56MHz Generator Connected to Coil:
Etch: 800W; Passivate: 600W
Platen Generator Connected to 13.56MHz:
Etch: 15W; Passivate: 6W

Recipe 4 (tether etch)

Name:

HQLIU500

Application:

Layer 3 – Step 16.

Gas (switching alternatively):

SF6, 100 sccm, for 14.5 seconds (etch step)
C4F8, 90 sccm, for 11 seconds (passivation step)

R.F.:

13.56MHz Generator Connected to Coil:
Etch: 700W; Passivate: 600W
Platen Generator Connected to 13.56MHz:
Etch: 19W; Passivate: 0W

Appendix D Testing Setup

D.1 Testing Jig for Pneumatic Actuation

The testing jig for the pneumatic actuation testing includes three parts: 1) testing jig lid; 2) testing jig base; and 3) testing jig support. An image of the testing jig base and the support is shown in Figure 4-8. A pump test chip is placed in the middle slot in the testing jig base, and then the testing jig lid is clamped onto the base with four screws. O-rings are used in between the test chip and the metal testing jig, and the eight o-ring slots are machined on the jig and the base. CAD drawings of the testing jig lid and base are shown in Figure D-1 & D-2.

(1) Testing Jig Lid

The CAD drawing of the testing jig lid is shown in Figure D-1 (unit: inch). The lid is made of stainless steel at MIT Machine Shop, as well as the testing jig base and support. Four Φ0.265" holes distributed around the lid center are cut through the lid for the four 1/4-20 clamping screws. Two Φ0.126" holes are also cut through the lid for the fitting pillars on the base. Eight Φ0.145" shallow slots are cut to hold the o-rings.

(2) Testing Jig Base

The CAD drawing of the testing jig base is shown in Figure D-2 (unit: inch). Four 1/4-20 screw holds are cut through the base, corresponding to the four Φ0.265" holes on the lid. Two pillars are added pointing out corresponding to the pillar holes in the lid. A central square chip slot is cut, and eight o-ring holding slots are made on the bottom of the chip slot, which have the same size and dimension as in the testing jig lid. Eight 1/8" NPT screw holes are cut evenly around the perimeter, with Φ0.12" channels connecting to the central chip slot.

(3) Testing Jig Support

The base is mounted to the support with two 1/4-20 screws, sharing two of the screw holes on the base with the four clamping screws. The height of the testing jig support is adjusted to fit the gas switches, pressure sensors, and the connectors requires, as shown in Figure 4-8.

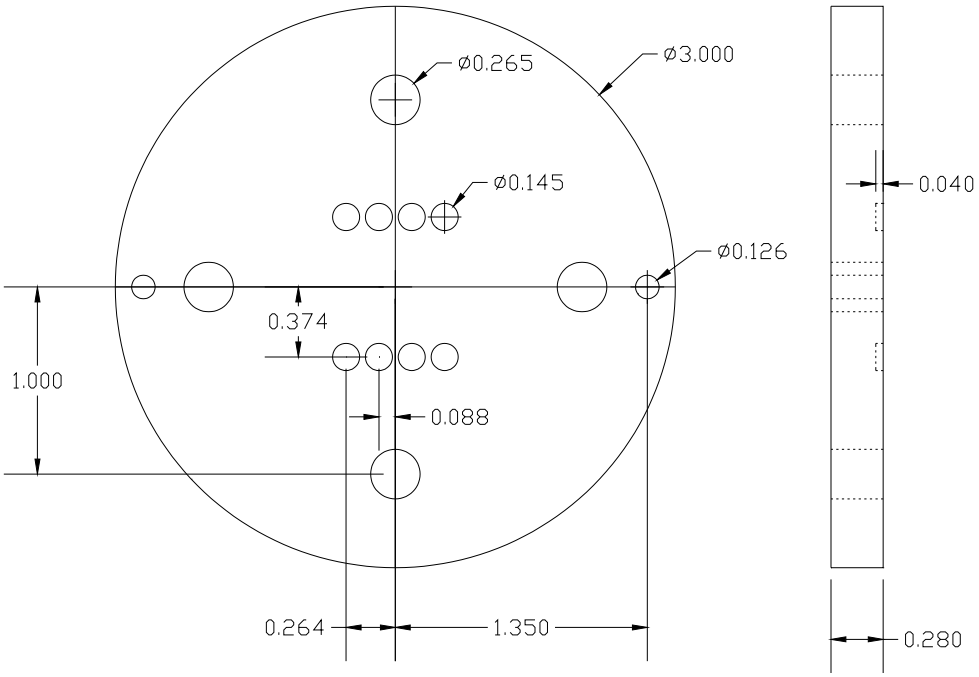

Figure D-1: CAD drawing of the testing jig lid.

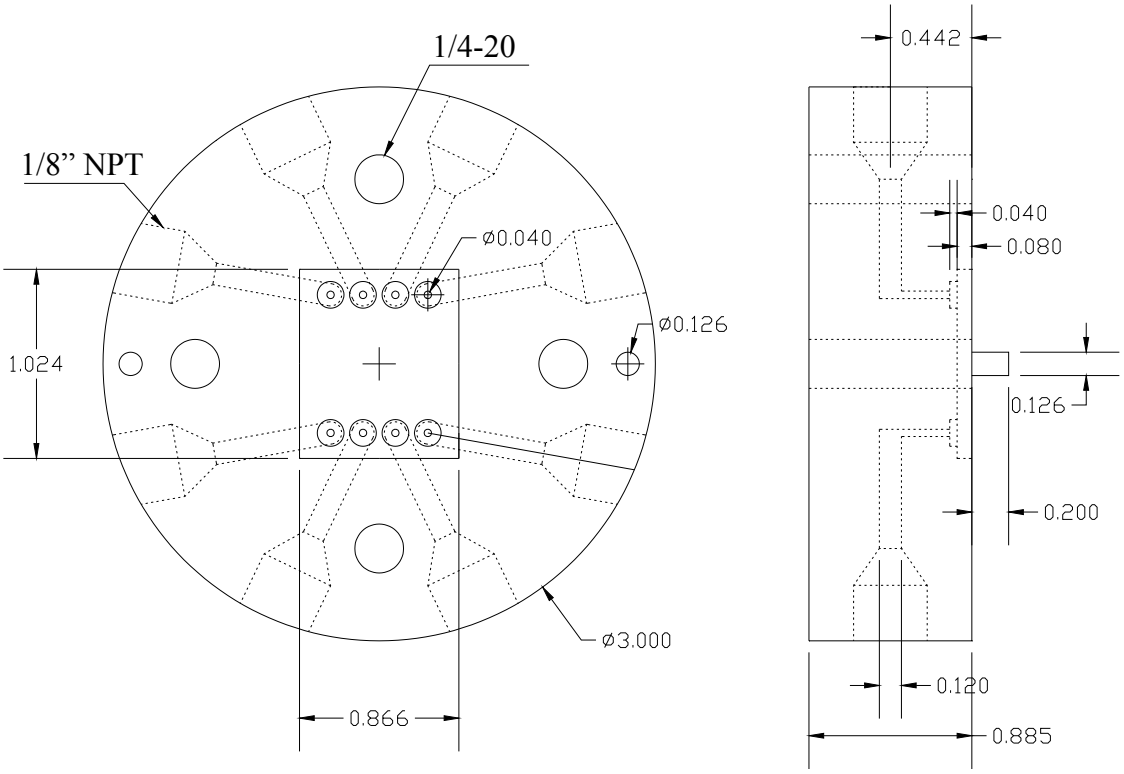

Figure D-2: CAD drawing of the testing jig base.

D.2 Testing Jig for Hybrid Actuation

An electromagnetic actuator could be used for hybrid actuation testing, and special testing jig lid has been designed. The CAD drawing of the modified lid is shown in Figure D-3.

The CAD drawing of the fixture holding the electromagnetic solenoid actuator is shown in Figure D-4.

A Φ1/8" stainless steel tube is glued to the silicon test chip with epoxy. The drawing of the connector, which connects the solenoid plunger and the Φ1/8" tube, is shown in Figure D-5.

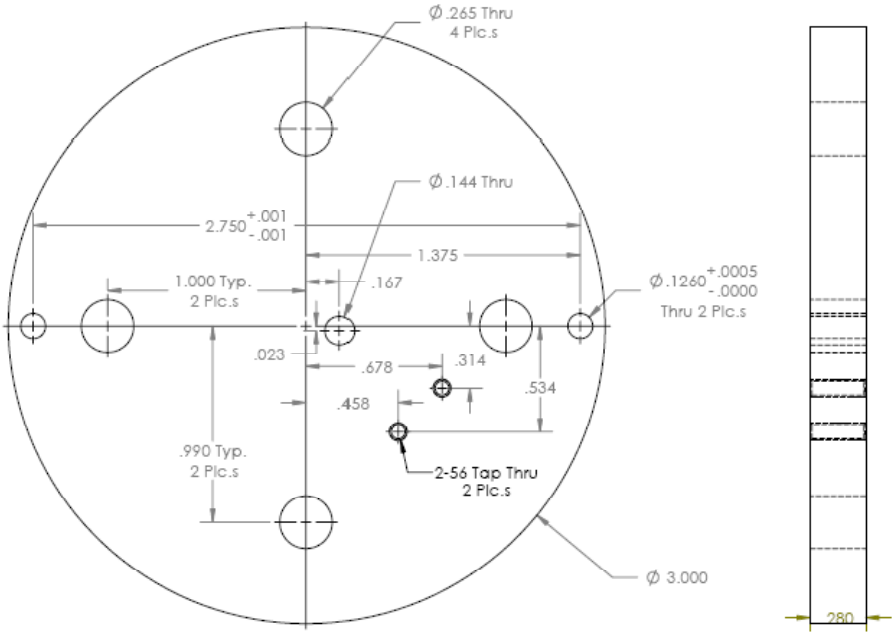

Figure D-3: CAD drawing of the testing jig lid for hybrid actuation testing.

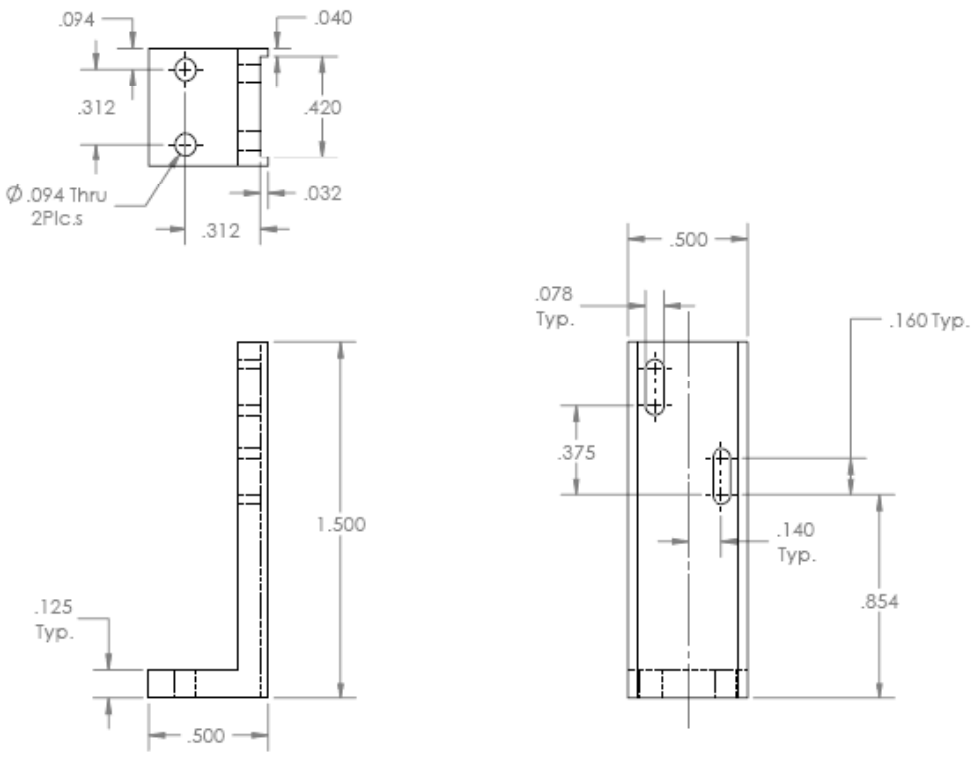

Figure D-4: CAD drawing of the fixture holding the solenoid actuator.

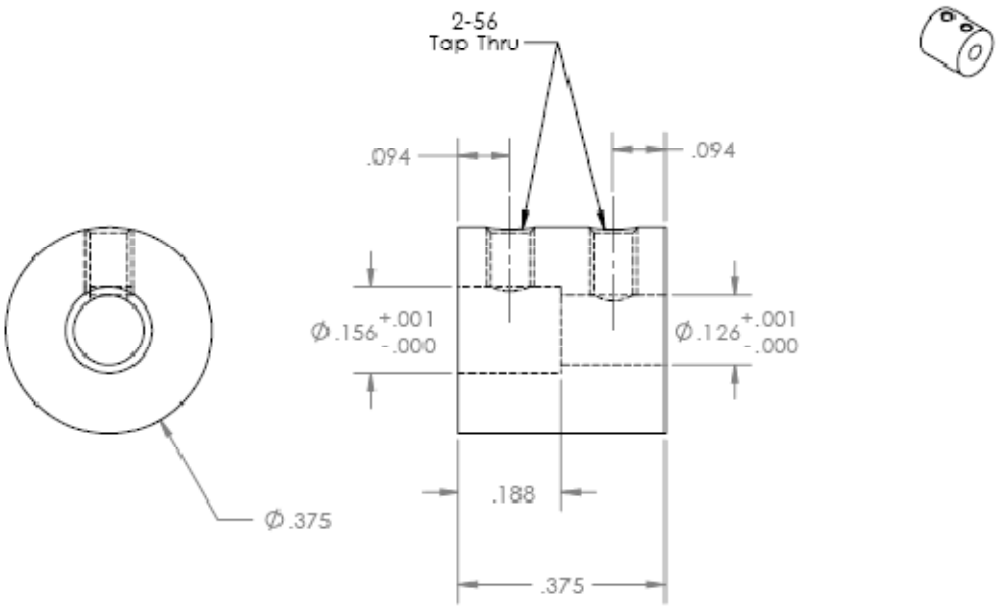

Figure D-5: CAD drawing of the fixture connector between the solenoid plunger and the connecting tube or pillar.

D.3 Other Testing Hardware

Other testing hardware components for the testing in this thesis work are listed as below.

Gas flow sensor:

Honeywell (0719-AWM3150V),

Pressure sensor:

Omega PX209-030A5V

Parker Convum MPS-L3N-PGA

Actuation gas flow switch:

Parker Kuroda VA01PEP34-1U

High pressure source:

House compressed nitrogen

Low pressure source:

External pump ULVAC GLD-040

Microcontroller:

Parallax BASIC Stamp 2

Electrical switch:

OMRON G6H-2

References

[1] D.J. Laser and J.G. Santiago, "A Review of Micropumps", Journal of Micromechanics and Microengineering, 14, pp. R35-R64, 2004.

[2] S. McNamara and Y. B. Gianchandani, "On-Chip Vacuum Generated by a Micromachined Knudsen Pump", Journal of Microelectromechanical Systems, 14, pp. 741-746, 2005.

[3] M. Doms and J. Muller, "A Micromachined Vapor-Jet Vacuum Pump", Technical Digest of Transducers & Eurosensors '07, Lyon, France, June 10-14, 2007, pp. 2425-2428.

[4] M. Doms and J. Muller, "A Micromachined Vapor Jet Pump", Sensors and Actuators A, 119, pp. 462-467, 2005.

[5] S.A. Wright and Y.B. Gianchandani, "Controlling Pressure in Microsystem Packages by On-Chip Microdischarges between Thin-Film Titanium Electrodes", Journal of Vacuum Science and Technology B, 25, pp. 1711-1720, 2007.

[6] K.P. Kamper, J. Dopper, W. Ehrfeld, and S. Oberbeck, "A Self-Filling Low-Cost Membrane Micropump", The Eleventh Annual International Workshop on Micro Electro Mechanical Systems, Heidelberg, Germany, January 25-29, 1998, pp. 432-437.

[7] H. Kim, A.A. Astle, K. Najafi, L.P. Bernal, and P.D. Washabaugh, "A Fully Integrated High-Efficiency Peristaltic 18-Stage Gas Micropump with Active Microvalves", Kobe, Japan, January 21-25, 2007, pp. 131-134.

[8] E.R. Badman, and R.G. Cooks, "Miniature Mass Analyzers", Journal of Mass Spectrometry, 35, pp. 659-671, 2000.

[9] Piezo Nano Positioning, Inspiration 2009 Catalog, PI (Physik Instrumente).

[10] S. Bohm, W. Olthuis, and P. Bergveld, "A Plastic Micropump Constructed with Conventional Techniques and Materials", Sensors and Acutators, 77, pp. 223-228, 1999.

[11] D.C. Roberts, H. Li, J.L. Steyn, O. Yaglioglu, S.M. Spearing, M.A. Schmidt, and N.W. Hagood, "A Piezoelectric Microvavles for Compact High-frequency, High Differential Pressure Hydraulic Micropumping Systems", Journal of Microelectromechanical Systems, 12, pp. 81-92, 2003.

[12] I. Chakraborty, W.C. Tang, D.P. Bame, and T.K. Tang, "MEMS Micro-Valve for Space Applications", Sensors and Actuators A, 83, pp. 188-193, 2000.

[13] S. Santra, P. Holloway, and C.D. Batich, "Fabrication and Testing of a Magnetically Actuated Micropump", Sensors and Actuators B, 87, pp. 358-364, 2002.

[14] O.C. Jeong and S.S. Yang, "Fabrication and Test of a Thermopneumatic Micropump with a Corrugated p+ Diaphragm", Sensors and Actuators A, pp. 249-255, 2000.

[15] P.W. Barth, "Silicon Microvalves for Gas Flow Control", Technical Digest of Transducers '95, Stockholm, Sweden, June 25-29, 1995, pp. 276-279.

[16] A.S. Dewa, K. Deng, D.C. Ritter, C. Bonham, H. Guckel, and S. Massood-Ansari, "Development of LIGA-Fabricated, Self-Priming, In-Line Gear Pumps", Technical Digest of Transducers '97, Chicago, June 16-19, 1997, pp. 757-760.
[17] J. Dopper, M. Clemens, W. Ehrfeld, S. June, K.-P. Kamper, and H. Lehr, "Micro Gear Pumps for Dosing of Viscous Fluids", Journal of Micromechanics and Microengineering, 7, pp. 230-232, 1997.
[18] M.A. Unger, H.P. Chou, T. Thorsen, A. Scherer, and S.R. Quake, "Monolithic Microfabricated Valves and Pumps by Multilayer Soft Lithography", Science, 288, pp. 113-116, 2000.
[19] J. Lee and C.-J. Kim, "Surface-Tension-Driven Microactuation Based on Continuous Electrowetting", Journal of Microelectromechanical Systems, 9, pp. 171-180, 2000.
[20] Y.J. Song and T.S. Zhao, "Modeling and Test of a Thermally-Driven Phase-Change Nonmechanical Micropump", Journal of Micromechanics and Microengineering, 11, pp. 713-719, 2000.
[21] B.K. Paul and T. Terhaar, "Comparison of Two Passive Microvalve Designs for Microlamination Architectures", Journal of Micromechanics and Microengineering, 10, pp. 15-20, 2000.
[22] M.C. Carrozza, N. Croce, B. Magnani, and P. Dario, "A Piezoelectric-Driven Stereolithography-Fabricated Micropump", Journal of Micromechanics and Microengineering, 5, pp. 177-179, 1995.
[23] H. Andersson, W. van der Wijngaat, P. Nilsson, P. Enoksson, and G. Stemme, "A Valve-Less Diffuser Micropump for Microfluidic Analytical Systems", Sensors and Actuators B, 72, pp. 259-265, 2001.
[24] P. Galambos, J.W. Lantz, C.D. James, J.L. McClain, M. Baker, R. Anderson, and R.J. Simonson, "Low Leak Rate MEMS Valves for Micro-Gas-Analyzer Flow Control", Technical Digest of Transducers 2009, Denver, June 21-25, 2009, pp. 1658-1661.
[25] R. Rapp, W.K. Schomburg, D. Maas, J. Schulz, and W. Stark, "LIGA Micropump for Gases and Liquids", Sensors and Actuators A, 40, pp. 57-61, 1994.
[26] V. Sharma, "MEMS Micropump for a Micro Gas Analyzer", Ph.D. Thesis, Massachusetts Institute of Technology, 2009.
[27] M. Tabib-Azar, Microactuators – Electrical, Magnetic, Thermal, Optical, Mechanical, Chemical & Smart Structures, Kluwer Academic Publishers, Boston, 1998.
[28] S. Shoji, and M. Esashi, "Microflow Devices and Systems", Journal of Micromechanics and Microengineering, 4, pp. 157-171, 1994.
[29] H. Zhou, "Micromechanical Actuators for Insect Flight Mechanics", S.M Thesis, Massachusetts Institute of Technology, 2008.
[30] W.C. Tang, T.H. Nguyen, and R.T. Howe, "Laterally Driven Polysilicon Resonant Microstructures", Sensors and Actuators, 20, pp. 25-32, 1989.

[31] W.C. Tang, T.H. Nguyen, M.W. Judy, and R.T. Howe, "Electrostatic-Comb Drive of Lateral Polysilicon Resonators", Sensor and Actuators, A21-A23, pp. 328-331, 1990.
[32] S. Egawa and T. Higuchi, "Multi-Layered Electrostatic Film Actuator", IEEE Proceedings on Micro Electro Mechanical Systems, Napa Valley, United States, February 11-14, 1990, pp. 166-171.
[33] R. Legtenberg, A.W. Groeneveld, and M. Elwenspoek, "Comb-Drive Actuators for Large Displacements", Journal of Micromechanics and Microengineering, 6, pp. 320-329, 1996.
[34] H.Q. Li, D.C. Roberts, J.L. Steyn, K.T. Turner, J. A. Carretero, O. Yaglioglu, Y.-H. Su, L. Saggere, N.W. Hagood, S.M. Spearing, M.A. Schmidt, R. Micak, and K.S. Breuer, “A High Frequency High Flow Rate Piezoelectrically Driven MEMS Micropump”, Technical Digest of the 2000 IEEE Solid State Sensor and Actuator Workshop, Hilton Head Island, SC, June 4-8, 2000, pp. 69-72.
[35] W. Griffel, Plate Formulas, Frederick Ungar Publishing Co., New York, 1968.
[36] H. Zhou, V. Sharma, H.Q. Li, and M.A. Schmidt, "A Study of Micromachined Displacement Pumps for Vacuum Generation", Technical Digest of the 2010 IEEE Solid State Sensor and Actuator Workshop, Hilton Head Island, SC, June 6-10, 2010, pp. 392-395.
[37] S.D. Senturia, Microsystem Design, Kluwer Academic Publishers, Boston, 2000.
[38] M. Hudspeth, "A Not-So-Booming Future", Desktop Engineering, 11, pp.46-48, 2010.
[39] H.A.C. Tilmans, "Equivalent Circuit Representation of Electromechanical Transducers: I. Lumped-Parameter Systems", Journal of Micromechanics and Microengineering, 6, pp. 157-176, 1996.
[40] T. Bourouina and J.P. Grandchamp, "Modeling Micropumps with Electrical Equivalent Networks", Journal of Micromechanics and Microengineering, 6, pp. 398-404, 1996.
[41] Y.C. Hsu and N.B. Le, "Equivalent Electrical Network for Performance Characterization of Piezoelectric Peristaltic Micropump", Microfluid Nanofluid, 7, pp. 237-248, 2009.
[42] P. Galambos, C.D. James, J. Lantz, R.C. Givler, J. J. McClain, and R.J. Simonson, "Passive MEMS Valves with Preset Operating Pressures for Microgas Analyzer", Journal of Microelectromechanical Systems, 18, pp. 14-27, 2009.
[43] R. Legtenberg, J. Gilbert, and S.D. Senturia, "Electrostatic Curved Electrode Actuators", Journal of Microelectromechanical Systems, 6, pp.257-265, 1997.
[44] M.A. Huff, A.D. Nikolich, and M.A. Schmidt, "Design of Sealed Cavity Microstructures Formed by Silicon Wafer Bonding", Journal of Microelectromechanical Systems, 2, pp. 74-81, 1993.
[45] V. Babu, Fundamentals of Gas Dynamics, CRC Taylor & Francis Ane Books, India, 2008.

[46] W.S. Griffin, H.H. Richardson, and S. Yamanami, “A Study of Fluid Squeeze-Film Damping”, Journal of Basic Engineer, pp. 451-456, 1966.
[47] K.S. Chen, A. Ayon, and S.M. Spearing, "Controlling and Testing the Fracture Strength of Silicon on the Mesoscale", Journal of American Ceramic Society, 83, pp. 1476-1484, 2000.